# Computation of the Load Flow at the Transformer in Distribution Grids with a Significant Number of Photovoltaic Systems using Satellite-derived Solar Irradiance Data

**Holger Ingmar Ruf**

# Computation of the Load Flow at the Transformer in Distribution Grids with a Significant Number of Photovoltaic Systems using Satellite-derived Solar Irradiance Data

Doctoral Dissertation for the Degree *Philosophiae Doctor (PhD)* at the Faculty of Engineering and Science, Specialisation in Renewable Energy

University of Agder
Faculty of Engineering and Science
2016

Doctoral Dissertation by the University of Agder 134
ISBN: 978-82-7117-827-7
ISSN: 1504-9272



Printed in the Printing Office, University of Agder
Kristiansand

# Preface

This dissertation contains the essential results from my work at the Institute of Energy and Drive Technologies, Ulm University of Applied Science, Germany. The research resulting in this dissertation was done during several publicly funded projects: ENDORSE (EU-FP7-SPACE, Grant Agreement No. 262892), SYSPV-NS (BMU, funding code 0325385), OrPHEuS (EU-FP7-ICT, Grant Agreement No. 608930) and NATHAN-PV (BMBF, funding code 03FH030I3).

Firstly, I would like to thank my supervisors Professor Hans Georg Beyer at the University of Agder, Norway, and Professor Gerd Heilscher at the Ulm University of Applied Science, Germany, for all their support and fruitful discussions. At many stages in this project I benefited from their advice, particularly so when exploring new ideas.

Further, I would particularly like to thank Marion Schroedter-Homscheidt at the German Aerospace Center (DLR) for explaining the meteorological background for this work, the endless patience in answering my questions and offering advice on data sources. I would also like to thank Florian Meier at Stadtwerke Ulm/Neu-Ulm Netze GmbH for the productive discussions about the interests and needs of the distribution system operators as well as the unlimited support in gathering and providing data and opportunities for measurements. This thesis would not have been possible without their help.

During my work I got the chance to spend some time as visiting scientist at the German Weather Service (DWD) in Offenbach, Germany. Thanks to Carmen Köhler and all the others from the EWeLiNE and ORKA research projects for hosting me. It was truly a memorable experience.

Furthermore, I would like to thank my colleagues at the Institute of Energy and Drive Technologies at Ulm University of Applied Science for their support and advice during the different research projects.

There are many more people both inside and outside the research projects who helped me with discussions, suggestions, ideas, comments, critiques, reviews and data. Thank you so much.

Last but not least, special thanks go to my family and friends for their support during the last years.

Holger Ingmar Ruf
Ulm, Germany
March 2016

# Summary

This thesis investigates the applicability of irradiance data provided by a weather satellite for the simulation of the high-resolution electric power load flow time series at a distribution grid transformer in an area with a significant number of residential PV systems. Up to the present, the feed-in tariff for renewable generators in Germany has encouraged the installation of a significant number of photovoltaic systems especially at the low voltage level. Current studies assume a further increase in the number of systems worldwide. The responsibility for the electric grid at this voltage level rests on the distribution system operators. However, the photovoltaic systems affect the characteristics of the electric grid and the distribution system operator needs more information than the current annual energy measurements can provide. One option that may contribute to the closing of information gap is the use of irradiance data derived from remote sensing technologies.

The load flow of the distribution grid transformer at a specific test site in Ulm, Germany, is calculated as a time series of 15-minute average values for a year. The feed-in power of each photovoltaic system connected to the grid is calculated using satellite-derived irradiance data and empirical non-linear photovoltaic models. The irradiance data are provided by different sources to investigate the influence of the irradiance source. The feed-in power is calculated with an average bias of 0.04 kW/kWp independent of the rated power of the photovoltaic system and varies with both the calculation algorithms and photovoltaic system orientation data used. The consumption time series is modelled with three different load profile types and scaled to the annual energy consumption provided by the distribution system operator. The different results of the variations are compared based on statistical measures and threshold detections are expressed as scores.

The bias of the satellite derived irradiance of around 5 % affects the simulation of the feed-in power. Experiment show that feed-in energy is overestimated by 22 % when using satellite irradiance while the use of locally ground-measured irradiance only results in an overestimation of 3 %. However, the statistical description of the consumption time series based on annual values leads to an additional bias of at least 33 % for the energy at the transformer level. These overestimations are also visible in the scores of threshold detection at both photovoltaic system and transformer levels. The accuracy of detecting feed-in power above 70 % of the photovoltaic system rating depends on the irradiance data and the modelling of the systems. The average false alarm rate is above 52 % for the investigated test site. The detection of reversal load flows at the low voltage transformer is overestimated leading to a false alarm rate of at least 12 % of all 15 minutes averages when the sun is higher than 15°.

This work makes clear that the detection accuracy strongly depends on the accuracy of the input data. The validation of the simulation up-scaled to the medium voltage level shows the weakness of absolute-value only measurements at the substation. The simulations also shows reversal load flows at this level. However, these results cannot be validated due to the limitation of the measurements to absolute values.

To conclude, the simulation of the feed-in power as well as the load flow at the transformer is overestimated at a local level such as a residential area. The main errors are caused by the load profile used followed by the satellite-derived irradiance. An accurate detection of events exceeding a threshold requires accurate input and model data. Overall the method is able to simulate the load flow at low voltage and medium voltage levels.

The effects of a significant number of PV systems on the electric grid and load flows have to be considered in grid planning and grid operations. Satellite-based irradiance data provides an opportunity to achieve independence from ground-based measurements limited to one location. If available, the orientation angles should be taken into account for analysis and calculations at the low voltage level.

# Contents

# List of Figures

# List of Tables

# Abbreviations

| | |
|---|---|
| AC | Alternating Current |
| AFGL | Air Force Geophysics Laboratory |
| *AM* | Air Mass |
| APOLLO | AVHRR Processing scheme Over cLouds, Land and Ocean |
| AVHRR | Advanced Very High Resolution Radiometer |
| BDEW | German Association of Energy and Water Industries |
| | (German: Bundesverband der Energie- und Wasserwirtschaft e. V.) |
| *BHI* | Beam Horizontal Irradiance |
| $BHI_{cs}$ | Beam Horizontal Irradiance, under clear-sky conditions |
| *BHR* | Bihemispherical Reflectance |
| *BNI* | Beam Normal Irradiance |
| $BNI_{cs}$ | Beam Normal Irradiance, under clear-sky conditions |
| $BNI_{ext}$ | Beam Normal Irradiance, at the top of the atmosphere |
| *BRDF* | Bidirectional Reflectance Distribution Function |
| *BTI* | Beam Irradiance, on a tilted plane |
| CAMS | Copernicus Atmosphere Monitoring Service |
| *CC* | Correlation Coefficient |
| *CTB* | Contingency Table Bias |
| DC | Direct Current |
| *DHI* | Diffuse Horizontal Irradiance |
| $DHI_{cs}$ | Diffuse Horizontal Irradiance, under clear-sky conditions |
| *DHR* | Directional Hemispherical Reflectance |
| DLR | German Aerospace Center |
| | (German: Deutsches Zentrum für Luft- und Raumfahrt) |
| *DNI* | Diffuse Normal Irradiance |
| $DNI_{cs}$ | Diffuse Normal Irradiance, under clear-sky conditions |
| DSO | Distribution System Operator |
| *DTI* | Diffuse Irradiance, on a tilted plane |
| $DTI_{ground}$ | Diffuse Irradiance, part on a tilted plane reflected by the ground |

| | |
|---|---|
| $DTI_{sky}$ | Diffuse Irradiance, part on a tilted plane from the sky dome |
| DWD | German Weather Service (German: Deutscher Wetterdienst) |
| ECMWF | European Centre for Medium-Range Weather Forecasts |
| ESRA | European Solar Radiation Atlas |
| ENDORSE | ENergy DOwnstReam SErvices |
| $FAR$ | False Alarm Rate |
| $G_{ext}$ | Global Irradiance, at the top of atmosphere |
| $GHI$ | Global Horizontal Irradiance |
| $GHI_{cs}$ | Global Horizontal Irradiance, under clear-sky conditions |
| $GTI$ | Global Irradiance, on a tilted plane |
| HC3v4 | HelioClim-3 version 4 |
| $I$ | Current |
| $I_{SC}$ | Short Circuit Current |
| IEA | International Energy Agency |
| $kC$ | Clear-sky index, cloud modification factor |
| $kCb$ | Clear-sky index related to beam irradiance |
| $kT$ | Clearness index |
| $kTb$ | Clearness index related to beam irradiance |
| LiDAR | Light Detection And Ranging |
| LUT | Look-Up Table |
| MACC | Monitoring Atmospheric Composition and Climate |
| $ME$ | Mean Error |
| MPP | Maximum Power Point |
| MPPT | Maximum Power Point Tracker |
| MODIS | Moderate-Resolution Imaging Spectroradiometer |
| MSG | Meteosat Second Generation |
| $n$ | Cloud index |
| $NPR$ | Nominal Power Ratio |
| NOAA | National Oceanic and Atmospheric Administration |
| NREL | National Renewable Energy Laboratory |
| OPAC | Optical Properties of Aerosols and Clouds |
| $PC$ | Proportion Correct |
| $p_{cloud}$ | Cloud parameter set for Heliosat-4, under cloudy conditions |
| $p_{cs}$ | Atmosphere parameter set for Heliosat-4, under clear-sky conditions |
| $p_{cs0}$ | $p_{cs}$, under clear-sky and typical atmospheric conditions |
| $P_{MPP}$ | Power at the MPP |
| $POD$ | Probability Of Detection |

| | |
|---|---|
| $POFD$ | Probability Of False Detection |
| $P_{STC}$ | Nominal PV Power, at STC |
| PV | Photovoltaic |
| PVPMC | PV Performance Modelling Collaborative |
| $rEM$ | Relative Error of Measurement |
| $rME$ | Relative Mean Error |
| $rRMSE$ | Relative Root Mean Squared Error |
| $RMSE$ | Root Mean Squared Error |
| RLP | Reference Load Profile |
| SAPM | Sandia Array Performance Model |
| SGPI | Sandia Performance Model for Grid-Connected Photovoltaic Inverters |
| SHC | Solar Heating and Cooling Programme |
| SOLEMI | Solar Energy Mining |
| SEVIRI | Spinning Enhanced Visible Infra-Red Imager |
| SLP | Standard Load Profile |
| STC | Standard Test Conditions |
| $STD$ | Standard Deviation |
| SWU | Stadtwerke Ulm/Neu-Ulm Netze GmbH |
| $T$ | Temperature |
| $THS$ | Threat Score |
| $TL$ | Linke Turbidity factor |
| TMY | Typical Meteorological Year |
| $U$ | Voltage |
| VDI | Association of German Engineers (German: Verein Deutscher Ingenieure) |
| $V_{OC}$ | Open Clamp Voltage |
| WMO | World Meteorological Organisation |
| $WS$ | Wind Speed |
| $\alpha_P$ | Temperature coefficient of PV power |
| $\gamma_s$ | Sun elevation angle |
| $\eta$ | Efficiency |
| $\Theta_z$ | Solar zenith angle, 90° at sunrise and sunset |
| $\lambda$ | Wavelength |
| $\rho$ | Albedo |
| $\rho_{cloud}$ | Cloud albedo |
| $\rho_{ground}$ | Ground albedo |
| $\rho_{sphere}$ | Atmospheric spherical albedo |
| $\rho_{sphere,cloud}$ | Spherical albedo of the cloudy atmosphere |

| | |
|---|---|
| $\tau_c$ | Cloud optical depth |

# Chapter 1

# Introduction

## 1.1 Background

The successful integration of a feed-in tariff in the markets of Germany and many other countries has led to a growing number of small photovoltaic (PV) systems with less than 30 kWp. The decreasing costs lead to a worldwide installed capacity of more than 180 GWp at the end of 2014 (IRENA, 2015). It is expected that PV increases further in the global energy mix and become a important part in the reduction of CO2 emission, e.g the International Energy Agency expect a installed PV capacity of 837 GWp by 2030 (IEA, 2015). Recently in Germany more than 1.5 million PV systems are connected to the grid and over 96 % of them are installed at the low voltage level (DGS, 2015).

The German distribution grid is be built-up of 507,000 km of medium voltage lines and 1.16 million km of low voltage lines in combination with approximately 560,000 transformers between both medium and low voltage level (BDEW, 2014).

The responsibility for grid stability and power quality at medium and low voltage level rests on the distribution system operators (DSO) according to several laws and regulations in Germany (EnWG, 2013). The objective of this law is the safe, well-priced, customer-friendly, efficient and environmentally compatible supply of the community with electricity and gas. They have to plan, operate and maintain the grid in an economic way which ensures no voltage band violations or overloading of grid elements do occur (EnWG, 2013; ARegV, 2007).

### 1.1.1 PV feed-in power affecting the electric distribution grid

In the last decades, the DSOs mainly considered the demand of their customers while planning their distribution grids. The installation of residential PV systems

in low-voltage grids changes the operation characteristics from demand-only to volatile demand and supply characteristic. The feed-in power of a PV system reduces the load-driven voltage drop and lead to higher voltage values within the grid. Depending of the amount of feed-in power these voltage values can be too high and violate the valid voltage thresholds (DIN EN 50160, 2011; VDE-AR-N 4105, 2011).

Furthermore, analysis show that an installed generation capacity of around 30 % of the annual consumption cause so-called reversal load flows during day-time and an increase of the voltage in the distribution grid (Mohrmann *et al.*, 2012; Ruf *et al.*, 2012b). Reversal load flows occur if the PV feed-in power exceed the current power consumption and the grid area fed the electric power to the upstream electric grid. This increase the voltage in the higher voltage level and can effect the effectiveness of the protection equipment.

The irradiance and therefore the PV feed-in power is highly volatile due to passing clouds. This applies to the single PV systems as well as for a PV fleet. The variability depends on the cloud conditions and wind speed as well as the spatial distribution and orientation of the PV systems (Hoff and Perez, 2010, 2012). Lave *et al.* (2015) analysed the influence of different solar irradiance variabilities on a distribution grid in the US and the number of tap changing operations. A high penetration of grids with PV can lead to high power ramp rates if the irradiance is change due to clouds. However, in low-voltage distribution grids high power ramp rates also occur due to the variability of the load. Schäfer *et al.* (2013) analyse secondly resolved power measurements over several month at different feeder lines in a low-voltage grid. They found no significant differences in the number of power ramp rates neither at feeders with PV systems nor at feeders without PV systems.

### 1.1.2 Changes in grid planning approaches

The grid planning reflects the requirement of a safe and efficient power supply provided by a public grid infrastructure. The main limits are the compliance with the voltage levels and the utilisation of the assets. Typical grid planning issues are the new grids in development areas or grid optimisations and reinforcements by changes in the demand or because of the utilisation.

The European standard for voltage characteristics of electric distribution networks (DIN EN 50160, 2011) defines a voltage band as $\pm$ 10 % of the nominal voltage and is strongly dependent on the load flow within the grid due to the line resistance. Calculation of the load flow allows the estimation of voltage values and distinguishes between PV-driven increase, load-driven decrease and the overlay ef-

fects by the medium voltage (Ruf *et al.*, 2013). Furthermore, normally the allowed voltage band of $\pm$ 10 % of the nominal voltage has to be split into parts for the low voltage and the medium voltage level because the last voltage regulating element is the transformer with on-load tap changers from the high voltage to the medium voltage. Therefore, the DSO is not able to control the voltage level at the lower level or in a certain area without additional assets. This makes the voltage band a limited resource in grid planning and operation.

Nowadays, the DSOs are reconsidering the traditional approach for dividing the voltage band into parts for the different voltage levels due to the consumption. Designated parts of the voltage band for the local generation are required and have to be defined. The new approaches for grid planning need more information about the influence of the volatile decentralized renewable energy on the voltage in the grids. Traditional grid reinforcement to increase the PV hosting capacity leads to high costs due to the costs for the installation of the lines (Schwarz and Kollmann, 2014). The efficiency of new established technologies such as voltage regulated distribution transformers, reactive feed-in power by inverters and the related control strategies require more time-dependent information about the behaviour in low voltage grids with a high amount of PV feed-in power.

### 1.1.3 Data availability in the low-voltage distribution grid

The interconnections between the high and medium voltage grid are monitored widely in real time. Also, remote controllable devices exist to actuate the grid. On the other hand, at the interconnections between the medium and the low voltage grid only current meters with slave pointers are used. These only show the real-time readings but do not store or transmit the data for further analysis. Additionally, they allow monitoring the maximum apparent power at a transformer station which occurred since the last readout. This does not solve the need for monitoring the grid state because an annual energy feed-in or demand value is not sufficient for planning and operating low voltage grids with volatile feed-in power (Bucher *et al.*, 2013a; Cohen and Callaway, 2016). Depending on the number of the installed PV systems, the PV feed-in power can exceed the maximum power consumption several times (IEA, 2014; Eilenberger and Braun, 2012).

A possible solution for collecting the necessary data can be the roll-out of smart meters but there are still discussions in refinancing the roll-out and the following annual communication costs as well as gaps in the regulatory framework (Buechner *et al.*, 2014). Another option is the installation of real-time monitoring devices into the secondary substations of the German distribution grid. However the installation

and operation of real-time monitoring for such a number of systems is a ambitious undertaking and will lead to uneconomic high costs.

Another option that may contribute to the closing of low voltage grid information gap was proposed during the ENDORSE[1] project (ENergy DOwnstReam SErvices): the use of irradiance data derived from remote sensing technologies. Methods for the surface irradiance estimation using satellite images are available since several decades and the time and spatial resolution increases with each satellite generation. Assuming a uniform distribution of all PV systems and medium-to-low voltage transformers over the area of Germany, each MSG pixel contains approximately 23 transformers and 60 PV systems. If only the settlement and traffic area of Germany is considered as distribution base each MSG pixel contains approximately 173 transformers and 433 PV systems. The proposed modular scheme is illustrated in Figure 1.1.

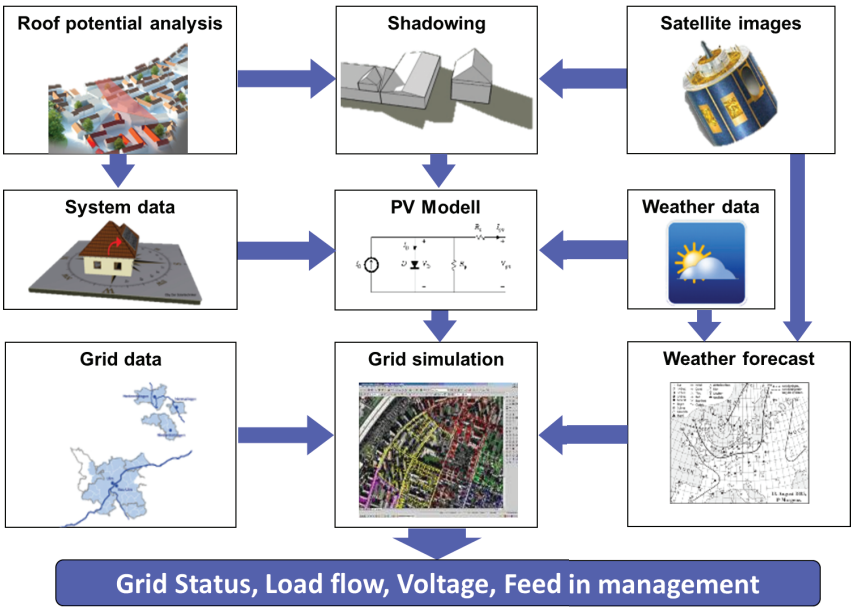


Figure 1.1: Modular scheme to computate the low voltage grid status based on satellite and roof-potential data (Ruf, 2012).

The roof potential analysis (top left) is an input data source based on an accurate 3D model of the whole city and provides both the inclination and azimuth angle for each roof and installed PV system as well as the nearby structures and buildings causing shadows on roofs and PV systems. The roof potential analysis completes the system data (middle left) of the installed PV systems containing location and nominal power with the orientation values. Furthermore, the data are necessary in-

[1] www.endorse-fp7.eu

put for the computation of shadowing effects (top middle) reducing the PV feed-in power. Data from the Meteosat-Second-Generation (MSG) meteorological satellite (top right) are available every 15 minutes and computed into surface irradiance data with the Heliosat method (Cano *et al.*, 1986; Schmetz *et al.*, 2002). This 15-minute time resolution is sufficient for electric grid simulations however the highest loss of information takes place between 1-minute and 5-minute time resolutions (Bucher *et al.*, 2013a; Cohen and Callaway, 2016) The power generation by PV (middle) can be computed when the irradiance and the temperature as well as the orientation and the inclination of the single PV systems, the module types and local shading effects are known. The temperature values are provided by ground-based measurements of weather data (middle right), e.g. a meteorological station. The combination of satellite-derived irradiance and PV feed-in power models including orientation angles cover the feed-in side of the grid state. However, the demand is not accessible by remote sensing but can be described by statistical approaches like typical load profiles. These consumption data are part of the grid data (bottom left) including number and type of consumers, annual energy consumption, voltage level and connection points. The grid simulation (bottom middle) requires both the PV feed-in power and the power consumption and offers support for the near real-time calculation of the state of a low voltage grid. The modular scheme is extendable with meteorological forecast (bottom right) techniques (Ruf, 2012).

### 1.1.4 Solar roof potential analysis data provision

The orientation values and the local shading can be derived from a solar roof potential analysis. The combination of using both digital elevation models based on airborne laserscan (LiDAR) data and solar irradiance data is state-of-the-art for the calculation of the received annual solar energy on tilted planes. The calculation approaches consider the diurnal and annual cycles of the solar irradiance as well as the local circumstances causing shadows on the tilted planes.

Several studies describe and analyse various approaches and techniques. Fath *et al.* (2015) use a 3D model of a part of the city of Karlsruhe, Germany, to calculate the solar potential on roofs and facades based on an hourly irradiance time series. This time series considers the local reflections and shadows as determined by a backwards ray-tracing algorithm for the irradiance estimation from the Radiance lighting simulation software (Larson and Shakespeare, 2003). The irradiance data are taken from the Meteonorm database (Meteotest, 2015). Jakubiec and Reinhart (2013) calculate the irradiance on tilted planes considering the local shadows and using the Radiance software also. The input data for the software is based on

ground measured irradiance data from a meteorological station nearby. The measurements from two PV systems at the campus of the Massachusetts Institute of Technology validate the calculated data. The focus of Verso *et al.* (2015) is also the annual global hourly irradiation on roofs for a small area in Spain. However, the irradiance data herein is taken from the Meteosat satellite with a 30-minute time resolution (Rigollier *et al.*, 2004; Zarzalejo *et al.*, 2009). The local shadow effects on the roofs are calculated with the *Hillshade* function of the ArcGIS software (Esri, 2015). Borfecchia *et al.* (2014) also uses satellite data for the calculation of the monthly solar irradiation potential in an urban area in Italy. In this study, the local monthly ground albedo is estimated with multi-spectral Landsat satellite images and the monthly average atmospheric turbidity from the MODIS (Moderate Resolution Image Spectrometer) satellites *Terra* and *Aqua*. The shadows on the roofs are also calculated with the laser-scan based urban 3D model.

In this thesis, the orientation angles of the single PV systems are based on recent LiDAR data from the test site. However, the implementation of the shadow calculation on PV systems is beyond the scope of this work.

### 1.1.5 Satellite-derived irradiance data for PV systems

The usage of satellite-derived irradiance data has a long history and is applied in a broad field of disciplines, e.g. climate or solar energy and electricity production (Lefevre *et al.*, 2014).

For the management of large scale transmission systems with a significant amount of PV penetration in Europe (Kühnert *et al.*, 2014) and the U.S. (Renné, 2014), the use of satellite derived irradiation information is state-of-the-art. The information gap concerning the lack of monitoring individual PV systems with their orientation and system data, is virtually closed by using a lumped PV model, representing the average response of the PV fleet (Beyer *et al.*, 2004). This requires that the number of PV systems covered is sufficiently large in order to average out the specific peculiarities of individual systems. Within this type of studies, details of planning and operation at the low voltage level are not handled. Several studies have been carried out to investigate the influence of PV systems on distribution grids considering meteorological parameters. Ground measurements of irradiance provide high accuracy and are often used in PV feed-in power studies (e.g. Ueda *et al.*, 2009; Lave *et al.*, 2015). Nevertheless, such ground measurements are only point measurements and do not fully represent the natural spatial and temporal variability of a distributed PV fleet in an area as, e.g. a regional utility grid.

In contrast, satellite-based irradiances provide a spatial information, but with

restrictions in the available spatial and temporal resolution according to their km sized pixels and their 15 minute temporally resolved observation scheme. The influence of distributed PV systems on the load flow in the distribution grid on both low and medium voltage levels has been described e.g. in Pardatscher *et al.* (2011). They derived the load flow for a total of 910 PV systems in a 12 km x 12 km area in southern Germany. However, the study was only for an assumed clear-sky day and another single day with large fluctuations as extreme cases. The day-to-day behaviour remains an open question. Grossi *et al.* (2014) simulate a PV fleet distributed over an area of 11 km x 15 km using irradiance data derived from satellite and assuming a singular orientation for all PV systems. The influence of PV feed-in power on the voltage level in an island grid also using satellite irradiance data is analysed in Rikos *et al.* (2008). Bucher *et al.* (2012) also use satellite irradiance data to derive statistic values for a given location to generate synthetic high resolution PV feed-in power by Monte-Carlo simulations. These synthetic feed-in profiles are used for the calculation of the hosting capacity for distributed PV in model grids, taking into account various load profiles.

## 1.2 Thesis objectives

The studies mentioned focus on larger areas than a single low voltage grid and higher voltage levels. A larger area benefits from a sufficient number of both PV systems and consumers that allows the usage of statistical approaches and lumped PV models, representing the average response of the PV-fleet.

This work continues the application of satellite data in distribution grids as mentioned above and scales the area of interest to the low voltage grid. The objective is the usage of irradiance data derived from satellite images as input for the simulation model of the load flow at a low voltage grid transformer.

The development and validation is performed for a single transformer in a suburban test site in Ulm, Germany. However, it will be shown, that this procedure is also applicable on larger scale. This is performed for several transformers connected to a medium-voltage feeder and validated against substation measurements.

The ground irradiance data are provided from external sources based on the Heliosat-2 and Heliosat-4 algorithms using satellite images from the MSG (Rigollier *et al.*, 2004; Oumbe *et al.*, 2014). The PV feed-in power is computed with a non-linear PV model based on empirical coefficients taking into account the orientation of each single PV system in the test site (King *et al.*, 2004, 2007). Usually, the DSO only knows the location and the nominal power of the PV system. The tilt and

azimuth angles were extracted by laser-scan data provided from an roof potential analysis for electric grid planning based on Ruf *et al.* (2015). As mentioned before, local shadowing effects are not considered. The load is assumed with different load profiles scaled to the annual household consumption.

The work will answer the following research questions:

- How accurate is the computation of the PV feed-in power of residential PV systems in a small area related to the spatial resolution of a satellite pixel?
- Is a simple model able to determine the load flow at the transformer level and what is its accuracy?
- How sensitive is the described approach to variations of models and input data, e.g. irradiance or load profile?

The answers are given by the validation of the main impact factors (irradiance, PV model, load profile) against measured data and an analysis due to variation of used data sources and models. The measured data are taken from PV feed-in smart meters and active power data-logger at the transformer level. Furthermore, the approach is scaled to a several stations connected to a medium voltage feeder and also validated with measured data from the substation provided by the DSO.

## 1.3 Thesis outline

This thesis is organized as follows:

In *Chapter 2*, a basic introduction to the surface irradiance calculation is given. A focus is set on the Heliosat approach and the herein used methods Heliosat-2 and Heliosat-4. Furthermore, the function and components of PV systems and the estimation of load profiles are briefly described.

*Chapter 3* describes the different data sources used for modelling and validation and gives an overview on their availability as well as gaps in the data.

The PV feed-in power model and transformer load flow model are explained in *Chapter 4*. Furthermore, the methods to analyse and compare the results of the different data and model variations are described.

*Chapter 5* combines the models with the data sources in the test site in the city of Ulm, Germany. The calculated values of the PV feed-in power as well as the load flow at low voltage and medium voltage level are validated with accurate measurements.

The results are discussed in *Chapter 6*. Furthermore, a comparison with results in literature is done.

*Chapter 7* draws overall conclusions from the present work and gives recommendations for application.

In *Chapter 8* an outlook for improvements in modelling as well as extensions with other research topics are given.

# Chapter 2

# Fundamentals

This chapter gives an introduction to required fundamentals of the irradiance on Earths surface and its calculation from satellite data. Furthermore, a brief introduction of the techniques behind the energy transformation from solar irradiance into electric power is given. The last section describes the assumed consumption time-series by the distribution system operators (DSOs) and the research community.

## 2.1 Irradiance at surface

### 2.1.1 Irradiance at the top of the atmosphere

The irradiance derived from the Sun received at the Earth is not constant. It varies by the Earths ecliptic orbit around the sun as well as by the 11-year-cycle of the Suns intensity. However, the monthly average influence of the Suns 11-year-cycle is approximately $1.6\,\mathrm{W/m^2}$ and therefore negligible. The long-term mean of irradiance received at the top of the atmosphere is denoted as solar constant $G_{ext} = 1360.8 \pm 0.5\,\mathrm{W/m^2}$ (Kopp and Lean, 2011). The influence of the ecliptic orbit can be calculated by

$$G_{ext}(J) = G_{ext}\left(1 + 0.0334\cos\left(0.0172^\circ J - 0.04747^\circ\right)\right), \tag{2.1}$$

where $J$ is the number of the day of the year.

### 2.1.2 Influence of the atmosphere

The irradiance spectrum changes due to the transfer through the atmosphere. This is caused by different absorption and scattering effects of the atmosphere particles.

The magnitude depends on the length of the path through the atmosphere and particle characteristics. The length can be denoted as air mass ($AM$) which is dependent on the sun elevation angle $\gamma_s$ or the sun zenith angle $\Theta_z$ by

$$AM = \frac{1}{\sin(\gamma_s)} = \frac{1}{\cos(\Theta_z)}. \tag{2.2}$$

Figure 2.1 shows the irradiance spectrum of $G_{ext}$ labelled as $AM0$ and the global irradiance reaching a tilted plane on the Earths surface labelled $AM1.5$ depending on the wavelength $\lambda$. According to ASTM (2012), the tilted plane is defined as an inclined plane at 37° tilt toward the equator, facing the Sun. The $AM1.5$ spectrum is lower in the peak compared to the $AM0$ spectrum and shows several sags. These sags are the result of the scattering and absorption by different chemical elements in the atmosphere e.g. oxygen, water vapour or ozone. The power of the spectrum is reduced from 1360.8 W/m$^2$ for $AM0$ to 1002.9 W/m$^2$ for $AM1.5$ (ASTM, 2012). Therefore, scattering and absorption effects of the atmosphere have to be taken into account in the irradiance calculation.

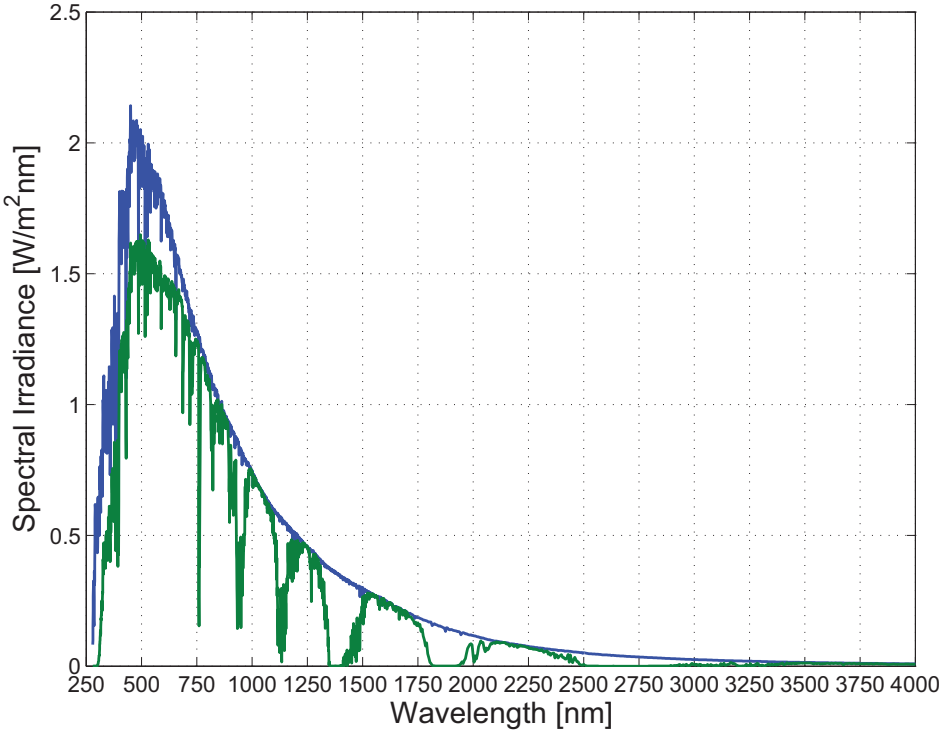


Figure 2.1: Solar irradiance spectrum at the top of the atmosphere ($AM0$, blue) and with $AM1.5$ (green) according to ASTM (2012).

The global irradiance on a horizontal surface is defined as $GHI$. $GHI$ is related to $G_{ext}$ but reduced by the atmosphere. During its travel through the atmosphere

*GHI* is divided into two parts. The first part, the beam component, is the part of $G_{ext}$ which reaches the surface directly. The second part is the result of irradiance absorption, scattering and reflection and is denoted as the diffuse part. The relation between those components is

$$GHI = BHI + DHI, \tag{2.3}$$

where *BHI* is the beam irradiance and *DHI* the diffuse irradiance, both also on the horizontal plane. The beam component received by a perpendicular plane facing the sun and following its path across the sky is called beam normal irradiance (*BNI*). The relation between *BHI* and *BNI* is given by

$$BHI = BNI \cdot \cos(\Theta_z). \tag{2.4}$$

The atmospheric influence can be expressed by transmission coefficients related to the effects by

$$GHI = G_{ext}\tau_{absorption}\tau_{Rayleigh}\tau_{Mie}\tau_{clouds}. \tag{2.5}$$

$\tau_{absorption}$ is the transmission coefficient describing the irradiance reduction effects due to absorption on atmospheric molecules and particles. Rayleigh scattering occurs if particles clearly smaller than the irradiance wavelength are present and its influence is expressed by $\tau_{Rayleigh}$. The Mie scattering occurs if particles in the range or larger than the irradiance wavelength are present and its effect is expressed in $\tau_{Mie}$. Clouds have the largest impact on the irradiance and can also be expressed by a transmission coefficient, $\tau_{clouds}$.

The single atmospheric components influence the solar irradiance in scattering and absorption. Hence, the transmission coefficients can also be related to the atmospheric components. The absence of clouds is defined as clear-sky and the irradiances are only dependent on the atmospheric parameters. Clear-sky conditions are denoted with the indices *cs* at the irradiance description e.g. $GHI_{cs}$ is the *GHI* under clear-sky conditions. The influence is enhanced for *BNI* and, following the modified Bird clear-sky model according to Iqbal (1983), for $BNI_{cs}$ it could be expressed by

$$BNI_{cs} = G_{ext}\tau_{Rayleigh}\tau_{gas}\tau_{ozone}\tau_{WV}\tau_{Ae}, \tag{2.6}$$

where $\tau_{gas}$ is the attenuation by permanent atmospheric gases (mainly CO2 and O2), $\tau_{ozone}$ is the attenuation by atmospheric ozone, $\tau_{WV}$ is the attenuation by water vapour and $\tau_{Ae}$ is the attenuation by aerosols (Schillings *et al.*, 2004).

The atmospheric parameters are dependent on presence and rate of various par-

ticles e.g. aerosols, water vapour or ozone. According to Espinar *et al.* (2014) aerosols have the strongest influence on clear-sky irradiance through absorption and scattering processes but it is hard to distinguish between both. The scattering follow the Mie scattering theory because the particle size is much larger than the solar irradiance wavelength. The optical thickness as function of the wavelength $\lambda$ can be approximated by Ångströms empirical equation by

$$k\lambda = \beta \cdot \lambda^{-\alpha}, \tag{2.7}$$

where $\beta$ is denoted as Ångström turbidity coefficient indicating the aerosol content integrated in a vertical column of the atmosphere. Usually, values for $\beta$ ranges from 0.0 to 0.5. The exponent $\alpha$ expresses the size distribution of the aerosol particles and is usually in a range of 0.25 to 2.5. The average is 1.3 and extreme values in a range of -0.5 to 3.0 are possible. The interaction of aerosols with the atmosphere and clouds is a complex issue. The aerosol sources are variable in time and space, and the aerosol life time is approximately one week (Espinar *et al.*, 2014). Modelling aerosols is a difficult task in atmospheric research and an overview of the methods can be found in Liu *et al.* (2005).

Furthermore, water vapour and ozone absorb solar irradiance in different spectral ranges. Water vapour mainly influences the solar irradiance spectrum in the thermal range ($\lambda > 780$ nm). Ozone absorbs the solar irradiance mainly in the spectrum range smaller than 320 nm and its influence is less compared to water vapour. The ozone variation is dependent on the latitude and time of the year (Schillings *et al.*, 2004). Different spatially distributed datasets are used for the modelling of the clear-sky atmosphere. A briefly overview about datasets for aerosols, water vapour and ozone is also given in Espinar *et al.* (2014). Oxygen and carbon dioxide only have a small influence on the solar irradiance absorption and are negligent in comparison to the water vapour and ozone (Liou, 1992).

Linke (1922) introduced a turbidity factor ($TL$, also known as Linke turbidity factor) as a practical approximation for the atmospheric absorption and scattering under clear-sky conditions. It describes the optical thickness of the atmosphere caused by absorption and scattering effects of aerosols and water vapour relative to a dry and clean atmosphere and therefore the extinction of the beam irradiance. $TL$ includes the influence of permanent atmospheric gases, e.g. CO2, O2, etc. The extinction increases with increasing $TL$. For clean and dry sky conditions, $TL$ would be equal to 1.0. A typical $TL$ for Europe is 3.0 while in a turbid atmosphere, e.g. with pollution, $TL$ can reach values of 6.0 to 7.0. The variability of $TL$ is also high in space and time (Espinar *et al.*, 2014).

In its original form, $TL$ is dependent on $AM$. Several approaches exist to avoid this dependency on $AM$ (e.g. Kasten, 1988; Grenier *et al.*, 1994; Ineichen and Perez, 2002). The generation of a worldwide database for $TL$ has been proposed by Remund *et al.* (2003). The database contains monthly mean values based on several years and a spatial resolution of 5' of arc angle. The previously described parameters have major influence on the clear-sky irradiance. To point this out, Figure 2.2 shows the influences for a typical day of clouds, aerosols, water vapour, Rayleigh scattering, ozone and permanent atmospheric gases (here O2 and CO2) on *BNI* calculated with the method proposed by Schillings *et al.* (2004). The atmospheric parameters were kept constant but the influence of sun elevation is evident.

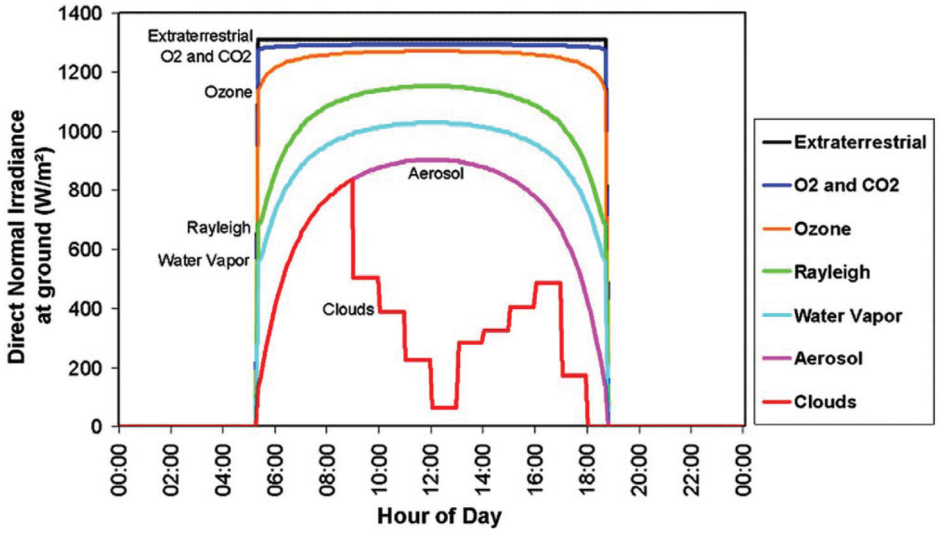


Figure 2.2: Example of the influence of different atmospheric gases, aerosols and clouds on the BNI. Figure and values are from Schillings *et al.* (2004).

### 2.1.3 Influence of the clouds

Clouds influence the solar irradiance in several ways: by reflection, absorption and transmittance. The amount of each effect depends on the cloud optical depth, the geometry between clouds, sun and point of interest. The basic scattering and absorption properties of cloud particles are determined by the particle size distribution. Furthermore, the scattering properties are also related to the particle type, water droplets or ice crystals, and shape, spherical and non-spherical. Clouds are also able to reflect and transmit irradiance emitted from the atmosphere or reflected from the surface (Liou, 1992).

Additionally, the direct irradiance can interact with layered clouds and result in reflected diffuse irradiance. Furthermore, a part of the direct and diffuse irradiance reflected by the surface can contribute to the multiply reflected irradiance which depends on reflectance properties of the cloud system and of the surface (Iqbal, 1983). Reflection can lead to irradiance enhancements on the ground, reaching values higher than under clear-sky conditions (Zehner *et al.*, 2010). Detailed model descriptions of these complex interactions can be found in Liou (1992). Simulations of those complex systems can be performed by using radiative transfer models e.g. libRadtran (Mayer and Kylling, 2005).

However, the atmospheric influence on the irradiance can be described within irradiance ratios. The first ratio is denoted as clearness index $kT$ and given by

$$kT = \frac{GHI}{G_{ext}}. \tag{2.8}$$

This index includes the influence of clouds and the atmosphere on the $GHI$ received at ground level. The next index is denoted as clear-sky index $kC$ and describes only the influence of the clouds as a ratio of $GHI$ at ground level related on $GHI_{cs}$ under clear-sky conditions by

$$kC = \frac{GHI}{GHI_{cs}}. \tag{2.9}$$

The clear-sky index $kC$ is equal to 1 when the sky is clear and decreasing inversely with cloudiness.

## 2.2 Satellite-derived irradiance measurement with the Heliosat method

Irradiance measurements from satellites have the advantage of providing data over a large area. There is no need for interpolation between ground measurements. Several approaches were developed to compute the ground irradiance based on satellite images. The method to calculate the clear-sky irradiance and taking into account cloud information provided by satellite images for the irradiance reduction is a standard according to Köpke (2012). The so-called Heliosat method provides the irradiance data used in this work and is described in this section.

The original Heliosat method was developed by Cano *et al.* (1986) at MINES ParisTech. The objective is the calculation of radiation at ground level using data from meteorological satellites. The fundamental principle of the method is the difference in reflectance between clouds and ground. The satellite sensor detects the

reflected radiation from earth and will measure an increased signal in pixels with clouds (brighter) than in cloud-free pixels. The difference between both depends on the depletion of the downward radiation by the atmosphere. Heliosat compares the detected radiation with modelled radiation which should occur under clear-sky conditions at the same pixel and time. Therefore, the calculation is performed in two steps: First, the cloud index is determined from the satellite images. Second, the radiation at ground level is calculated taking into account the cloud index.

The original Heliosat method uses the clearness index $kT$, the ratio between the $GHI$ and the irradiance at the top of the atmosphere $G_{ext}$. It characterizes the reduction of the solar radiation by the whole atmosphere. The translation of $kT$ into the cloud index $n$ is performed by an empirical function

$$kT = a \cdot n + b. \tag{2.10}$$

The parameters $a$ and $b$ are calculated by comparison of ground measurements and related satellite data. The parameter values between the ground measurement stations are spatially interpolated (Cano *et al.*, 1986) and could also be averaged (Diabaté *et al.*, 1989).

The method was improved by Beyer *et al.* (1996) and was later called Heliosat-1. The major adoption is the usage of the clear-sky index $kC$ instead of the clearness index $kT$. The clear-sky index is independent of atmospheric influences and only related to the cloud conditions, while $kT$ takes into account the whole atmosphere including scattering effects and clouds. This leads to a general relation between $kC$ and the cloud index $n$ by

$$kC = 1 - n. \tag{2.11}$$

Further improvements were done by the partial removal of the dependence of the received radiance with the viewing angle. In addition, the empirical parameters for determining the ground and cloud albedo were revisited and adopted with actual measurements from European ground stations.

The next version, Heliosat-2, was designed at MINES ParisTech (Rigollier *et al.*, 2004). This version is based on Heliosat-1 and is looking for the removal of the empirical parameters. Therefore, several models were adopted and linked to Heliosat. Important issues were the calibration of the Meteosat images to convert the image grey values into radiation and reflectance and the adoption of the clear-sky model proposed in the European Solar Radiation Atlas (ESRA, Rigollier *et al.*, 2000). The databases SOLEMI and HelioClim-3 (version 4, denoted as HC3v4) used in this thesis are based on Heliosat-2, and will be described in detail in the appendix in

Chapter 10.1.

The implementation of the SOLIS clear-sky module was a major improvement in the version called Heliosat-3 (Mueller *et al.*, 2004). Nowadays, the Heliosat method has been adapted by many researchers and is used in several implementations and with various adaptions in several systems and projects (Ineichen, 2013).

During the EU funded projects MACC and MACC-II (Monitoring atmospheric composition climate, FP7) Heliosat-4 was developed jointly by MINES ParisTech and the German Aerospace Center (DLR). The major variation to the previous versions is the separated calculation of the clear-sky irradiance with zero ground albedo and the influencing effects of clouds and the surface (Qu *et al.*, 2012). The MACC-RAD service is online [1] and available for free since end of 2014. Recently, MACC-RAD is renamed to *CAMS radiation service*. The service is part of the Copernicus Atmosphere Monitoring Service (CAMS).

## 2.3 Irradiance on tilted planes

Usually, PV systems are not mounted horizontally and tracker systems are also not common in Europe. Therefore, the irradiances has to be calculated into the tilted plane.

### 2.3.1 Angle definitions

The definitions of the required angles for the sun position and the orientation of the tilted plane are described in the following section and shown in Figure 2.3.

The zenith is defined as perpendicular to a horizontal surface and pointing to a point in the sky dome exactly above the location. The extension in the opposite direction, below the horizontal surface, is called nadir.

The position of the sun is given by the sun azimuth $\alpha_s$ (clockwise, 0° = North to 270° = West) and the sun elevation $\gamma_s$ both in degree. With these angles a vector $s$ is given pointing to the sun. The angle between $s$ and the the zenith is defined as $\Theta_z$ with the relation $\Theta_z = 90° - \gamma_s$.

The tilted plane is defined by the angle $\alpha_p$ between North and its surface azimuth angle. This azimuth angle follows the same convention as $\alpha_s$ meaning in degrees east of north (e.g. North = 0°, East = 90°, West = 270°). The tilt angle is denoted as $\gamma_p$ and defined as degrees from the horizontal. The normal vector $N$ of the tilted plane is a vector perpendicular to it. The angle between the $s$ and $N$ is denoted as

[1] www.soda-pro.com

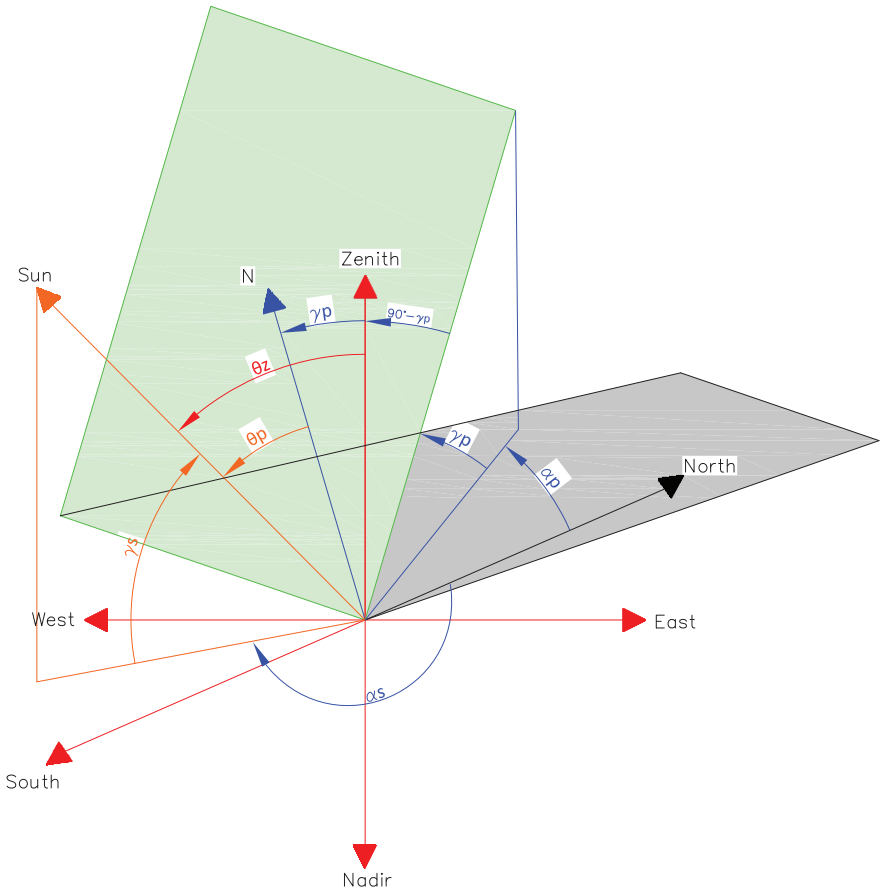


Figure 2.3: Angle definitions for sun position and tilted plane.

$\Theta_p$ and determine the angle of incidence. $\Theta_p$ is calculated by

$$\Theta_p = \arccos\left(-\cos\left(\gamma_s\right)\sin\left(\gamma_p\right)\cos\left(\alpha_s - \alpha_p\right) + \sin\left(\gamma_s\right)\cos\left(\gamma_p\right)\right). \tag{2.12}$$

The relation defined in equation 2.3 is also valid for tilted planes by

$$GTI = BTI + DTI, \tag{2.13}$$

where $GTI$ is the global irradiance, $BTI$ the beam irradiance and $DTI$ the diffuse irradiance, each on the tilted plane.

### 2.3.2 Calculation of beam irradiance

The beam irradiance on the tilted plane can be calculated using trigonometric functions considering the position of the sun and the orientation of the plane by

$$BTI = BHI\frac{\cos\left(\Theta_P\right)}{\sin\left(\gamma_s\right)}, \tag{2.14}$$

where $\Theta_P$ is the angle of incidence and $\gamma_s$ is the sun elevation.

### 2.3.3 Calculation of diffuse irradiance

The calculation from $DHI$ to $DTI$ is not given by simple trigonometric equations. Therefore, several models were developed to compute $DTI$ based on empirical relations (e.g. Hottel and Woertz, 1942; Reindl *et al.*, 1990a,b; Perez *et al.*, 1990). Loutzenhiser *et al.* (2007) gives an overview about $DHI$ conversion models. $DTI$ can be estimated by considering the diffuse irradiance received from the sky $DTI_{sky}$ and the diffuse irradiance reflected by the ground $DTI_{ground}$ as well as parts of the irradiance from the circumsolar area $DTI_{circumsolar}$ and the horizon brightening $DTI_{horizon}$ by

$$DTI = DTI_{sky} + DTI_{circumsolar} + DTI_{horizon} + DTI_{ground}. \tag{2.15}$$

The circumsolar irradiance $DTI_{circumsolar}$ is the diffuse fraction from the surrounding area of the sun disc and has multiple definitions in literature. Blanc *et al.* (2014a) gives an overview of the various definitions and summarize a common definition by solar experts from the International Energy Agency Solar Heating and Cooling Programme (IEA SHC) Task 46. The diffuse irradiance coming from close to the horizon increases due to a larger portion of the incident radiation scattering. This

depends on the irradiance path length through the atmosphere (Reindl *et al.*, 1990a).

Originally, the $DTI$ calculation models were developed for hourly irradiance data. Gueymard (2009) shows that these models are also accurate for time resolutions like 1 minute and sensitive to the accuracy of the input data e.g. $GHI$, $BNI$ and $\rho_{ground}$.

#### 2.3.3.1 Ground reflected diffuse irradiance model

The diffuse fraction reflected by the ground depends on the ground albedo $\rho_{ground}$ and the tilt angle $\gamma_p$. It is given by

$$DTI_{ground} = GHI \cdot \rho_{ground} \left( \frac{1 - \cos(\gamma_P)}{2} \right). \tag{2.16}$$

Typical values for $\rho_{ground}$ are listed in Table 2.1 (Iqbal, 1983).

Table 2.1: Typical values for $\rho_{ground}$ from some surfaces (Iqbal, 1983).

| *Surface* | $\rho_{ground}$ |
|---|---|
| Grass, dry | 0.19-0.22 |
| Grass, wet, no sun | 0.14-0.26 |
| Grass, wet, sun | 0.33-0.37 |
| Soil, dry, leveled | 0.2 |
| Soil, moist, leveled | 0.12 |
| Sand | 0.21-0.43 |
| Forest, coniferous | 0.12 |
| Forest, coniferous and deciduous | 0.12-0.20 |
| Snow, dry, new fallen | 0.82 |
| Snow, compacted, dry, clean | 0.66-0.80 |
| Snow, melting | 0.35 |
| Asphalt, new | 0.09 |
| Asphalt, weathered | 0.18 |
| Tiles, red | 0.33 |
| Tiles, concrete, uncolored | 0.35 |
| Wood | 0.22 |
| Aluminium | 0.85 |
| Steel | 0.8 |
| Paint, oil paint, cream, light | 0.7 |

#### 2.3.3.2 Isotropic DTI calculation model

The simplest $DTI$ calculation model is the isotropic model according to Hottel and Woertz (1942) and given by

$$DTI_{sky} = DHI\left(\frac{1+\cos(\gamma_T)}{2}\right). \tag{2.17}$$

This model assumes a uniform distribution of the diffuse irradiance from everywhere within the sky dome. However, this model does not consider the horizon brightening and circumsolar irradiance which leads to underestimation in clear-sky and partly cloudy conditions. Therefore more complex models are required.

#### 2.3.3.3 Anisotropic DTI calculation model

An example for such more complex $DTI$ calculation model was developed by Reindl *et al.* (1990a). This model considers both diffuse irradiance from the circumsolar area and diffuse irradiance from the horizon brightening. The description of further anisotropic $DTI$ calculation models can be found in Loutzenhiser *et al.* (2007). The three components $DTI_{sky}$, $DTI_{circumsolar}$ and $DTI_{horizon}$ are calculated by

$$\begin{aligned} &DTI_{sky} + DTI_{circumsolar} + DTI_{horizon} = \\ &DHI\left[(1-A)\left(\tfrac{1+\cos(\gamma_P)}{2}\right)\left(1+\sqrt{\tfrac{BHI}{GHI}}\sin^3\left(\tfrac{\gamma_P}{2}\right)\right)+A\cdot R\right] \end{aligned}, \tag{2.18}$$

where $A$ is the anisotropy index and $R$ is the ratio of tilted and horizontal solar beam irradiance. Both $A$ and $R$ are given by

$$A = \frac{BNI}{G_{ext}} \tag{2.19}$$

and

$$R = \frac{\max(\cos(\Theta_P), 0)}{\max(\cos(\Theta_z), 0.01745)}. \tag{2.20}$$

## 2.4 Photovoltaic systems

This section describes the basic technology of photovoltaic systems. Photovoltaic systems are based on the photoelectric effect, explained by Einstein (1905). A grid connected PV system consists of a PV generator built up of PV modules and an inverter to convert the DC power into AC power to feed-in.

### 2.4.1 Photovoltaic cell

The photons at a specific wavelength $\lambda$ are absorbed within the semiconductor of a PV cell and raise electrons into the conduction band. Besides, the intensity, the spectrum is relevant. The energy of a photon must reach the energy defined by the width of the band gap of the semi-conductor material. Photons lower than this threshold will not be absorbed. Photons with more energy will be absorbed but only the portion of the energy depending on the band gap will raise electrons into the conduction band. The excess energy is transformed into heat.

Several models for the description of PV cells exist, based on an equivalent electric circuit and with different accuracies (Paulescu *et al.*, 2012). Normally, the model equations could only be solved numerically and gives the current-voltage curve (IV-curve) of the PV cell (Figure 2.4 top). The point of intersection of the IV-curve with the voltage axis is denoted as open-circuit voltage $V_{OC}$ and describes the voltage across the cell under no load condition. The point of intersection of the characteristic with the current axis is denoted as short-circuit current $I_{SC}$. The multiplication of $I$ and $V$ leads to the power curve (Figure 2.4 bottom). The power curve shows that there is a maximum point, denoted as maximum power point (MPP) $P_{MPP}$ with the corresponding voltage $U_{MPP}$ and current $I_{MPP}$.

The efficiency of a PV cell $\eta_{MPP}$ can be calculated by

$$\eta_{MPP} = \frac{P_{MPP}}{G \cdot A_C}, \tag{2.21}$$

where $G$ is the irradiance in W/m$^2$ and $A_C$ is the cell area. According to the semi-annual updated solar cell efficiency table (Green *et al.*, 2015) is the highest efficiency in research laboratories for crystalline silicon cells 25.6 % and the overall efficiency of 37.9 % is given for a multijunction cell. The efficiencies for PV modules ranges from 12.2 % (amorphous silicon) over 17.5 % (thin film) and 22.9 % (crystalline silicon) to 24.1 % (gallium arsenide).

The PV cell is not only dependent on the irradiance but also on the temperature. With increasing temperature the $I_{SC}$ increases while the $V_{OC}$ decreases. Overall prevails the decrease of $V_{OC}$ and leads to a decrease in the output power. The decrease can be expressed with a temperature coefficient $\alpha_P$ which is dependent on the cell technology. These dependencies are shown in Figure 2.5. In the upper part of the image is the influence of the irradiance on the IV-curve visible. The IV-curve is shown for a PV cell and four irradiance values (from 1000 W/m$^2$ to 250 W/m$^2$). The decrease of the irradiance leads to a strong decrease of $I_{SC}$ and a minor decrease of $V_{OC}$. The lower part of the Figure 2.5 shows the dependency of the IV-curve on

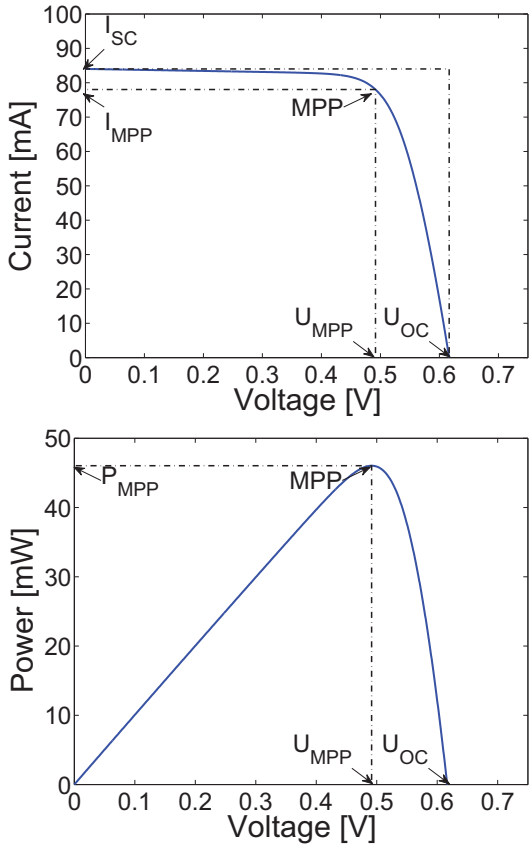


Figure 2.4: IV-curve of a PV cell and the corresponding power-curve. The short-circuit current $I_{SC}$ and open-circuit voltage $V_{OC}$ as well as the maximum power point (MPP) $P_{MPP}$ with the corresponding voltage $U_{MPP}$ and current $I_{MPP}$ are marked.

the cell temperature. The cell temperature of the IV-curve at an irradiance of 1000 W/m$^2$ is varied from 0°C to 75°C. The increase of the cell temperature leads to a decrease of $V_{OC}$ and a minor increase of $I_{SC}$. However, the decrease of $V_{OC}$ is predominant and overall $P_{MPP}$ decreases.

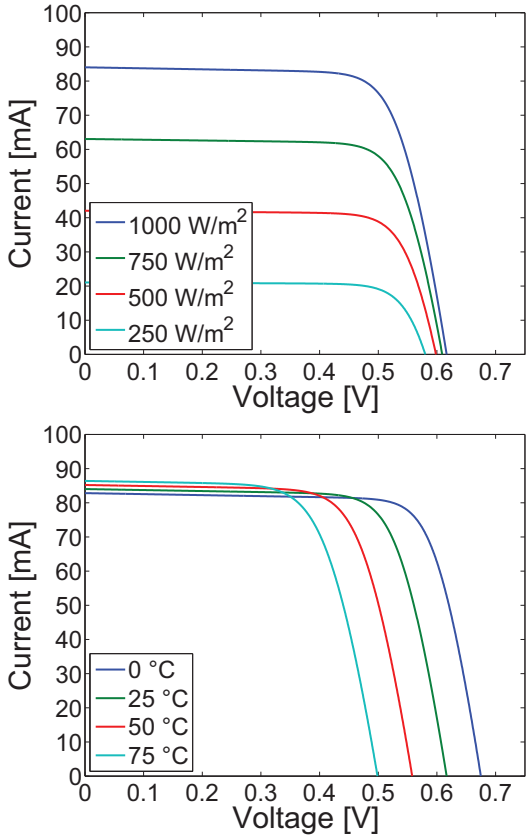


Figure 2.5: Influence of irradiance from 1000 W/m$^2$ to 250 W/m$^2$ (above) and temperature from 0°C to 75°C (below) on the IV-curve of a PV cell.

### 2.4.2 Photovoltaic module

The combination of several electrically conducted cells (in parallel and/or serial connection) into a frame is named as PV module.

PV modules follow the same dependencies as PV cells: mainly irradiance and temperature. The nominal values of PV modules are normally related to the standard test conditions (STC) meaning an irradiance of 1000 W/m$^2$, cell temperature of 25°C and a irradiance spectrum of $AM1.5$. The electric operation parameters ($V_{OC}$, $I_{SC}$, $V_{MPP}$, $I_{MPP}$ and $P_{MPP}$) under STC conditions and the temperature coefficients have to be given by the data sheet of the module (DIN EN 50461, 2007). These are

the nominal operation conditions, therefore $P_{MPP}$ is denoted as $P_{STC}$. The unit $P_{STC}$ is defined as Wp (watt-peak) to highlight the dependency on operation conditions.

However, it is rare that PV modules work under STC conditions. The solar irradiance and air temperature vary in wide ranges as does the solar spectrum. Moreover, the irradiance received at the module leads to a increase of the PV cell temperature. Similarly, as in the variance of irradiance models, there are several models for the adaption from model IV-curves into operational conditions. Based on the equivalent electric circuit models there are models using a different number of parameters to describe the IV-curve. These parameters have to be determined by accurate laboratory measurements or considering assumptions to calculate the model parameters under outdoor conditions (Paulescu *et al.*, 2012). The effort to identify the parameter can be avoided. A simplified model for the estimation of the DC output under outdoor conditions for different PV technologies was proposed by Beyer *et al.* (2004). This model provides $\eta_{MPP}$ as a function of the irradiance and temperature. It requires four empiric parameters depending on the device.

King *et al.* (2004) describes a photovoltaic array performance model developed at Sandia National Laboratories over several years. It is denoted as Sandia array performance model (SAPM). This empirical model includes electrical, thermal and optical characteristics of PV modules and was validated for modules with different technologies (King *et al.*, 1997a,b; Kroposki *et al.*, 2000). The model is based on measured module parameters from outdoor tests and available in databases for a variety of modules. It is defined by a set of 10 equations describing the electrical performance for individual PV modules and scalable for a wide range from PV cells to large arrays. This equation set considers the non-linear characteristic of PV modules. It describes the IV-curve by the three points mentioned above: $V_{OC}$, $I_{SC}$ and the maximum-power point. Furthermore, two additional points on the curve are defined to improve the curve shape. The fourth point is defined at $V_{OC}/2$ and denoted as $I_x$. The fifth point is defined at $(V_{OC}+V_{MPP})/2$ and denoted as $I_{xx}$. All points are shown in Figure 2.6.

These five points describe the basic shape of the IV-curve. The maximum-power point, $I_x$ and $I_{xx}$ are adopted with a set of eight performance coefficients related to the influence of irradiance. The detailed description of the equations and guidelines to estimate the performance coefficients can be found in King *et al.* (2004). SAPM is part of the PVLib which is publicly available from the PV Performance Modeling Collaborative[2] (PVPMC; Stein, 2012).

[2] `pvpmc.sandia.gov`

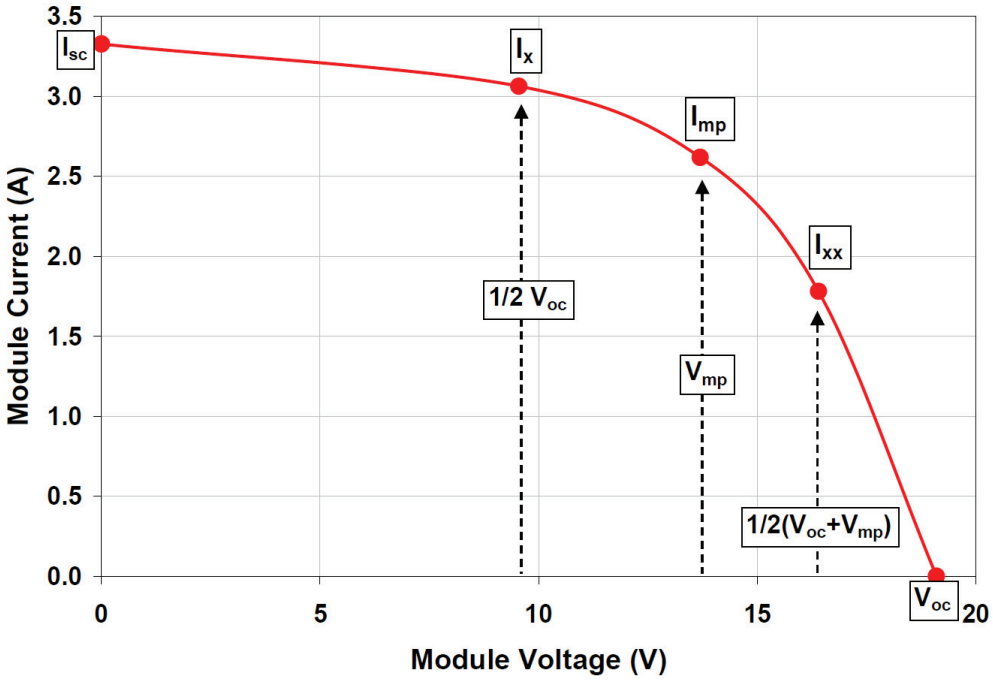


Figure 2.6: Illustration of a module IV-curve showing the five points on the curve that are provided by the SAPM (King *et al.*, 2004).

### 2.4.3 Photovoltaic inverter

Inverters are relevant parts of grid-connected PV systems. Their objective is the transformation from the direct current (DC) provided by the PV generator into alternating current (AC) for the feed-in into the electric grid considering the required constraints e.g. voltage, frequency and quality (DIN EN 50160, 2011). They are also able to provide services for the grid stability like reactive power provision or power reduction dependent on frequency (VDE-AR-N 4105, 2011). The inverter input contains a DC/DC converter operating as MPP tracker (MPPT) ensuring the maximum power adaptation between the PV generator and inverter to reduce the power mismatch losses. On the output side a DC/AC-converter (single or three-phase) is implemented. Taking into consideration the losses inside an inverter, the inverter efficiency $\eta_{Inv}$ is defined by

$$\eta_{Inv} = \frac{P_{AC}}{P_{DC}}, \tag{2.22}$$

where $P_{AC}$ is the AC output power feed in into the electric system and $P_{DC}$ is the DC input power from the PV generator. Normally, $\eta_{Inv}$ has a maximum below the rated nominal inverter DC power $P_{DC,Inv,nom}$ and slightly decreases towards the

$P_{DC,Inv,nom}$. However, if $P_{DC}$ is below approximately 10 % of $P_{DC,Inv,nom}$, $\eta_{Inv}$ shows a steep drop (Mertens, 2013). The distribution of irradiance in Europe shows high frequencies with low irradiance values while high irradiances seldom occur. As a consequence, to maximize the annual yield take into account optimal investment costs, there are recommendations for the ratio between the $P_{DC,Inv,nom}$ and the nominal PV generator power. This nominal power ratio *NPR* is defined by

$$NPR = \frac{P_{DC,Inv,nom}}{P_{STC}}. \tag{2.23}$$

A *NPR* of 1.0 means that the inverter has the same nominal power as the PV generator. Values below 1.0 indicate a smaller $P_{DC,Inv,nom}$ than the nominal power of the PV generator and are recommended in Germany (Albrecht and Schröder, 2013).

King *et al.* (2007) describes an empirical performance model for grid-connected PV inverters (SGPI) provided by Sandia. Instead of electrical engineering model using circuit characteristics, it uses a set of measured performance coefficients. Depending on the accuracy of the measured data the model accuracy and complexity can be improved. The required initial coefficients are available in inverter data sheets while more complex coefficients can be taken from measurements in operation or a laboratory. The SGPI models the inverter as a complex system with a non-linear response to several factors. Each factor is described as a linear relation to independent variables. Similarly to the SAPM, the SGPI is able to address several objectives like the calculation of system performance, electrical characteristics or monitoring of existing systems. The set of equations describing SGPI and the four inverter specific empirical coefficients can be found in King *et al.* (2007).

The model depends on the PV generator voltage and power and does not consider the MPPT because of its high efficiency and the high effort for the MPPT measurement. It does also not consider the air temperature of the inverter because of the low efficiency dependence on temperature. The SGPI is also part of the PVlib (Stein, 2012).

## 2.5 Load profiles

This section describes the background of load profiles which was state-of-the-art and adequate for planning and operation of distribution grids until the increase of decentralized volatile generators. The effort to measure each household as a time-series was too expensive but with the development of smart meters as enabler for smart grids this became reachable (Ernest and Young GmbH, 2013). In Germany,

there is still no roll-out of smart meters because of delays in the development of a smart meter protection profile to ensure the data safety and data security.

### 2.5.1 Standard load profiles

In the past there was no economic solution for the consumption measurement as time-series for each household. Only customers with an annual demand larger than 100 MWh or a power demand higher than 500 kW are normally equipped with meters measuring and recording the consumption (so-called RLM meter) according to StromNZV (2014). Based on a measurement campaign with several DSOs in the 1980s, the German Association of Energy and Water Industries (BDEW, German: Bundesverband der Energie- und Wasserwirtschaft e. V.) developed so-called standard load profiles (SLP). These profiles represent the normalized consumption for different types of customers (commercial, agricultural and residential) as a time-series with 15-minute resolution and normalized to an annual consumption of 1000 kWh. The SLPs are created for each year in advance based on typical days and with respect to the calendar including working days, Saturdays and Sundays (also used for public holidays). There are typical days for each season of the year: summer time, winter time and transition time. Summer time is defined as the time period from the 15$^{th}$ May to 14$^{th}$ September and winter time is defined as the time period from 1$^{st}$ November to 20$^{th}$ March. The days between are related to transition time.

The construction of the SLP for residential customers (called H0-profile) is briefly described in the following (Fünfgeld and Tiedemann, 2000). The load profiles of the typical days are rearranged according to the calendar days considering Saturdays, Sundays and public holidays (also regional). The typical days are chosen from the three different times of the year. The load profiles of the typical days are sorted according to the order of the calendar and result in a time-series for the observation period, normally one year. Afterwards this time-series is normalized to the annual consumption of 1000 kWh. A dynamic function is multiplied with each instant value of the time-series because residential profiles show a strong correlation to the changes in the seasons. The dynamic function is a fourth order polynomial function. The result of this multiplication is the H0-profile considering the high consumption during winter and low consumption during summer.

According to Düwall (1985), it can be assumed that the deviation is within $\pm 10\,\%$ of the H0-profile for the number of 400 or more households. However, according to Engels (2000), the deviation is around the mean of the H0-profile for at least 150 households and can be used as first approximation. The application of

an SLP in a specific case or area could be performed by multiply the SLP and the annual consumption.

Beside the H0-profile different SLPs or different groups of consumers exist, e.g. residential, agriculture and commercials. Eight SLPs for commercial and three for agricultural consumers are used in Germany (Fünfgeld and Tiedemann, 2000). In this work, two are considered for commercial consumers and one for agricultural consumers. The two commercial profiles represents average commercials (denoted as G0) and commercials operating around-the-clock (denoted as G3), respectively. The profile denoted as L0 represents an averaged agricultural consumer.

### 2.5.2 Reference load profiles according to VDI 4655

In areas with fewer than 150 households, a linear interpolation between the minimum power value of the SLP and the stand-by consumption (approx. 160 W for 10 buildings) can be done for steady state studies (Kerber, 2011). However, this is a constant value for grid planning issues and not a time-series for load flow calculations. Therefore another type of load profile is evaluated.

The Association of German Engineers (VDI) has developed reference load profiles (RLP) of single-family and multi-family housing for the use of combined heat and power systems (VDI 4655, 2008). These load profiles are based on measurements of electrical, heating and domestic hot-water energy consumption of single and multi-family houses over at least one year. The load profiles have a resolution of one-minute averages for single-family houses or 15-minute averages for multi-family houses. Out of the measured data typical load curves for typical days were computed. There are ten typical days defined by the division into:

- workday or Sunday
- fine or cloudy
- time of year: transition, summer or winter

The distinction into workdays and Sundays is based on the calendar for the period. Furthermore, holidays also are taken into account. The distinction into fine and cloudy is based on the average cloud amount of a day (24 hours). Cloud amount is expressed in eights and a day is defined as fine if the cloud amount average of this day is below 5/8. Otherwise this day is defined as cloudy. The distinction into transition, summer or winter time is based on the average temperature of a day (24 hours). A day is related to summer time if the average temperature is above 15°C. A day is related to winter time if the average temperature is below 5°C. Days with an average temperature between 5°C and 15°C are related to transition time.

The calculation of the reference profiles for each typical day is performed using meteorological data from a typical meteorological year (TMY) provided by the German Weather Service (DWD). This TMY divides Germany into 15 climate zones. The location of the building under consideration is used for the allocation of the building into a climate zone and influences the empirical factors for the daily energy demand. The determination of these empirical factors is described in Dubielzig (2007) while the detailed calculation guideline can be found in VDI 4655 (2008).

The advantage of these RLPs over the SLPs is the usability as time-series for single buildings or building areas with less than 150 buildings where the SLP is not valid. Another advantage is the high time resolution of single-family houses which is helpful for research in self-consumption with PV (Tjaden *et al.*, 2014). The major drawback of these RLPs for aggregated load profiles at a transformer is the coincidence. This leads to implausibly high demand values and have to be considered in the simulation setup of an area with several houses.

Hence, there is a great deal of research towards the development of synthetic load profiles, but this is not in the scope of this work. Details can be found in recent literature (e.g. Dickert and Schegner, 2011; Pflugradt and Platzer, 2012; Wieland *et al.*, 2015)

# Chapter 3

# Data Sources

This chapter introduces and describes the applied data and their sources. The irradiance data based on satellite images and meteorological measurements from ground stations are input for the PV feed-in power calculation. The described test site for both low voltage and medium voltage level is assigned for the application of the method and its validation.

Furthermore, not all data are available at the same time period because of measurement system roll-out during different measurement campaigns in the research projects and data logger failure and maintenance. The availability of the data is illustrated in Figure 3.1. The satellite irradiance data from SOLEMI, HelioClim-3 and MACC-RAD are available for 2012. The low voltage transformer load flow measurement is also available in 2012. The meteorological ground data except the *GHI* ground measurement and irradiance from MACC-RAD are available during the whole investigation period from $1^{st}$ January 2012 to $31^{th}$ December 2014. The ground-based *GHI* measurement has a gap in June 2013 because of a measurement system failure. Measurements of the single PV systems are available since $15^{th}$ May 2013 and measurements of the medium voltage line load flow at the substation since $12^{th}$ March 2013. In 2014, data from all local measurement systems are available within two month namely $7^{th}$ August 2014 to $9^{th}$ October 2014.

## 3.1 Satellite-derived irradiances

This section describes the availability of satellite irradiance data used in the three different sources. These irradiance data are the input parameters of the model for calculation of the load flow at the transformer.

The irradiance data from the Solar Energy Mining (SOLEMI) database are provided by DLR for the location of the weather station at the campus of Ulm Univer-

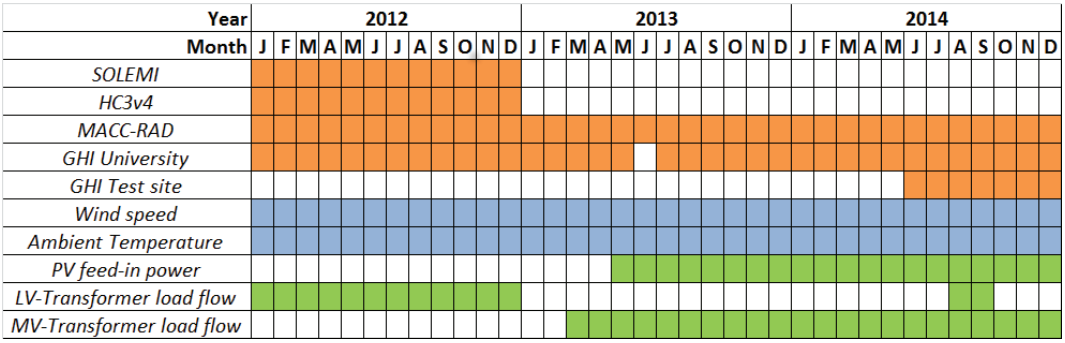


Figure 3.1: Available data from 1$^{st}$ January 2012 to 31$^{th}$ December 2014.

sity of Applied Science and for the test site for the years 2006 to 2012. The data set contains hourly average values for $GHI$, $DHI$ and $BNI$ as well as $GHI_{cs}$, $DHI_{cs}$ and $BNI_{cs}$. For the same locations as mentioned above, MINES ParisTech provided data from the HelioClim-3 (version 4, denoted as HC3v4) database for the years 2011 to 2012. The data set contains 15-minute average values for $GHI$, $GHI_{cs}$, $DHI$ and $BHI$ as well as $GNI$, $DNI$ and $BNI$. Both SOLEMI and HC3v4 data are computed with the Heliosat-2 method and differ in the time resolution and the clear-sky irradiance model as described in Section 10.1. The MACC-RAD service (version 2.6) provides public and online[1] irradiance data for dates later than 1$^{st}$ February 2004. The irradiance data are computed with the Heliosat-4 method (see Section 10.2). The dataset contains 15-minute average values for $GHI$, $DHI$, $BHI$ and $BNI$ as well as $GHI_{cs}$, $DHI_{cs}$, $BHI_{cs}$ and $BNI_{cs}$ for the locations mentioned above.

For the year 2012, all irradiance data are compared with the related 15-minute averages of the ground station at the university campus. The SOLEMI data are linearly interpolated to 15-minute time resolution. The analysis is performed following the guidelines for benchmarking of single point broadband solar radiation data according to Beyer *et al.* (2009). The standard measures chosen for describing the model quality are the mean error ($ME$), root-mean-squared error ($RMSE$) and correlation coefficient ($CC$) as well as the relative values of $ME$ and $RMSE$ denoted as $rME$ and $rRMSE$. The description and equations can be found in Section 9.1. The comparison considers all data pairs with a sun elevation angle above 15° because the physical processes of the Heliosat method are not valid below that limit and ensures the comparability to the literature (e.g. Rigollier *et al.*, 2004). Furthermore, only pairs are considered with a ground measured value of at least 10 W/m$^2$. Figure 3.2 shows the scatter plots of the comparison for all three satellite irradiance services.

[1] `www.soda-pro.com`

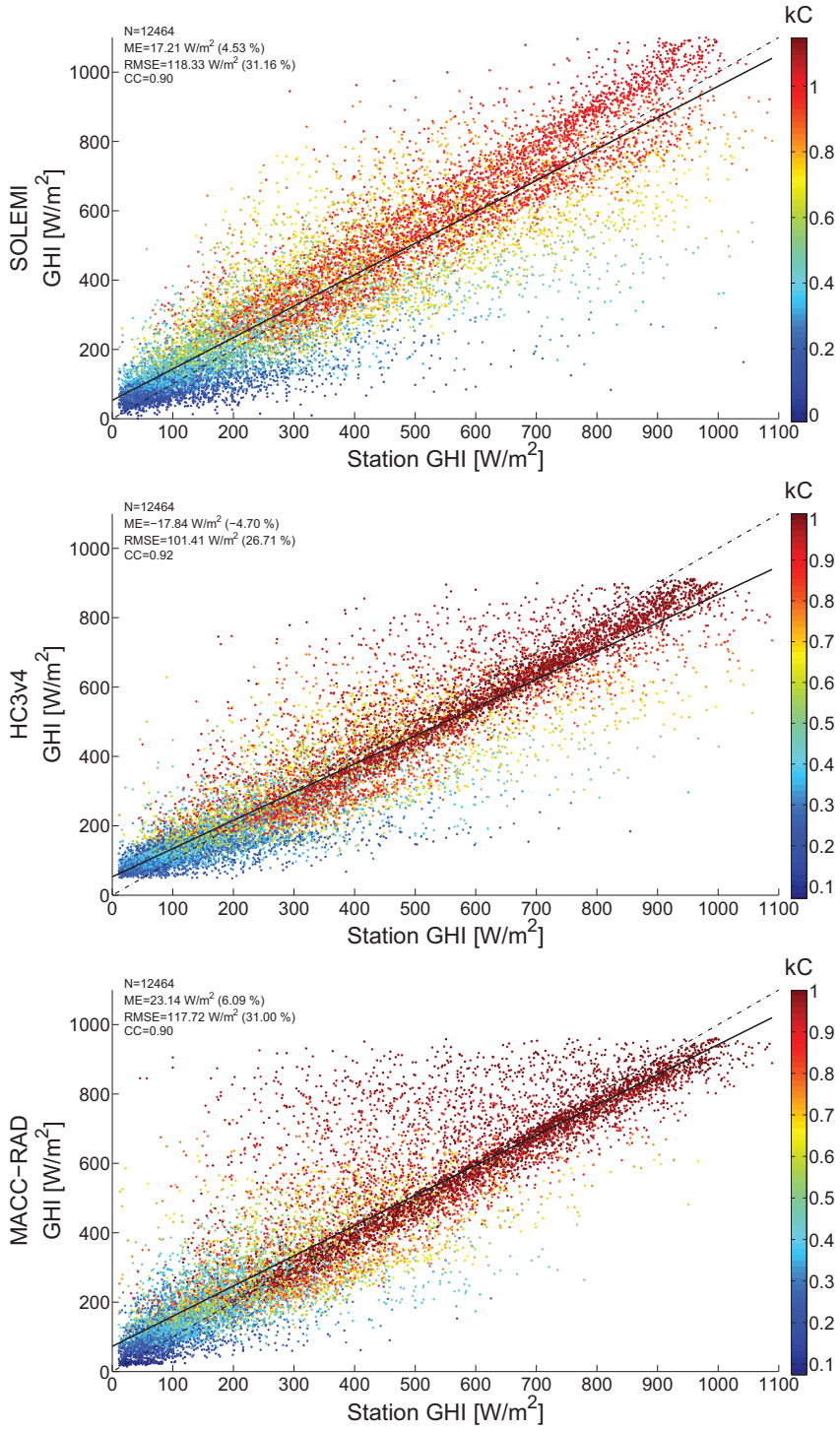


Figure 3.2: Comparison between ground measured *GHI* (Station GHI) on the x-axis and satellite measured *GHI* of SOLEMI, HC3v4 and MACC-RAD on the y-axis in 2012. The clear-sky index *kC* is colour-coded. Red illustrates high *kC* values while blue indicates low *kC* values. The main diagonal is shown as the chain dotted line. The black solid lines indicate the linear regressions. All values are 15-minute averages.

The detailed results of the *GHI* comparison of the different satellite sources are shown in Table 3.1. The highest irradiance with almost 1100 W/m$^2$ and the lowest *ME* are given for SOLEMI. MACC-RAD shows a slightly larger *ME*, but performs similar to SOLEMI in *RMSE*, while HC3v4 shows the best *RMSE*. In terms of *CC* all datasets are almost equal. The scatter plot of MACC-RAD shows a higher level of scatteredness values above the main diagonal axis indicating an overestimation. This is also visible in the positive *ME*.

Table 3.1: Comparison of the *GHI* between SOLEMI, HC3v4 and MACC-RAD validated with ground measurements in Ulm

| | ***SOLEMI*** | ***HC3v4*** | ***MACC-RAD*** |
|---|---|---|---|
| *ME* [W/m$^2$] | 17.08 | -18.08 | 22.98 |
| *rME* [%] | 4.49 | -4.75 | 6.04 |
| *RMSE* [W/m$^2$] | 118.41 | 101.45 | 117.69 |
| *rRMSE* [%] | 31.10 | 26.65 | 30.91 |
| *CC* | 0.90 | 0.92 | 0.90 |

In this work, the validation of *GHI* is performed for a single point only and does not give a general answer about the accuracy of the irradiance data. However, the statistical measures are in the range of publicised results (DLR, 1999; Qu *et al.*, 2012). It can therefore be assumed that there are no local effects in the area of Ulm preventing the usage of the satellite data.

## 3.2 Ground-based meteorological data

### 3.2.1 Ground-measured data

Ulm University of Applied Science operates a meteorological station on the roof of the campus (latitude 48.42°N, longitude 10.00°E, 650 m above sea level). The distance to the test site location where the method is applied in a low voltage grid is 11 km. The university station measures temperature with a Thies *hygro-thermo transmitter compact* (operating range from -30°C to 70°C, accuracy $\pm$ 0.1 K at 0°C), wind speed and wind direction with a cup-anemometer (operating range from 0.5 m/s to 75 m/s, accuracy $\pm$ 0.5 m/s or 2.0 % of the measured value) in combination with wind direction sensors, also manufactured by Thies. The ground-based *GHI* is measured with a calibrated pyranometer (First class according to ISO 9060 (1990)) manufactured by Theodor Friedrichs GmbH. The data are available for the performance analysis from 1$^{st}$ January 2012 to 31$^{th}$ December 2014 with a lack of data in June 2013 due to a data logger failure. The data logger acquires the instant

measure values each second and stores them. Afterwards, 15-minute average values are calculated.

### 3.2.2 Comparison with a reference meteorological station

The averaged ambient temperature and wind values of this weather station are used as input for the PV feed-in power model. However, the weather station does not correspond with the guidelines for observation of the World Meteorological Organisation (WMO) because it is installed on a building roof (WMO, 2008).

The closest WMO-conform station is at a distance of 5.8 km (latitude 48.38°N, longitude 9.95°E, 570 m above sea level) and operated by the German Weather Service (DWD). The DWD weather station is assumed to be a highly accurate reference station. The technical details of the sensors at the DWD weather station are unknown, however, it can be strongly assumed that the accuracy is at least as high as for the university station.

The 10-minute average data from the year 2012 are taken to compare the ambient temperature and wind speed of both DWD and university weather stations. The comparison of the ambient temperature shows a strong correlation ($ME$ = 0.01°C, $RMSE$ = 0.58°C, $CC$ = 1.00). For wind speed, the error values increases ($ME$ = 0.16 m/s, $RMSE$ = 0.79 m/s, $CC$ = 0.81). Therefore, the data of the university station can be assumed as accurate because of the low error values and high correlation.

### 3.2.3 Comparison with measurements at the test site

Since June 2014, a compact weather station has been mounted at the transformer station and is used for the comparison of ambient temperature and wind speed between the weather station at the university campus and the test site. The results are an indicator for the deviation because both university campus and test site do not correspond to the WMO guidelines for weather stations. Ambient temperature as well as wind speed and wind direction at the test site are provided by a *Vaisala weather transmitter WXT520* using an ultrasonic transducer to measure the wind speed. The accuracy of the weather transmitter is stated as $\pm$ 0.3 K at a temperature of 20°C and $\pm$ 3 % at wind speed of 10 m/s. The ambient temperature also shows a strong correlation ($ME$ = 0.35°C, $RMSE$ = 1.92°C, $CC$ = 0.97) while the wind speed is overestimated by the university campus weather station ($ME$ = 1.04 m/s, $RMSE$ = 1.37 m/s, $CC$ = 0.69).

However, according to Krauter *et al.* (2008) an error in the ambient temperature of 1°C leads to approximately 0.5 % change in $P_{MPP}$ of the PV modules. A deviation

in error of wind speed of 50 % affects the annual PV yield with 1.5 %. The higher deviation in wind speed measurements is assumed as acceptable because of the low impact on the PV feed-in power.

## 3.3 Test case for a low voltage transformer

This section describes the test site with the current PV systems and household consumptions. The load flow at the low voltage transformers is calculated for this location. The installed measurement systems provide accurate data for the validation.

### 3.3.1 Test site

A test site is defined in the suburban Einsingen close to the city of Ulm, Southern Germany. In cooperation with the local DSO Stadtwerke Ulm/Neu-Ulm Netze GmbH (SWU), the test site was equipped with several measurement systems during different measurement campaigns.

The test site covers the area of 470 x 615 $m^2$ defined by the area supplied via a 630 kVA low voltage transformer and 133 houses attached via eight feeder lines. Figure 3.3 shows an aerial image of the test side. The 12 PV systems equipped with smart meters are marked in red, the other 9 PV systems are in blue.

Figure 3.4 illustrates the spatial ratios of the test site (green-filled polygon) to the city districts of the city of Ulm (black polygons) and the size of the MSG pixels.

### 3.3.2 Residential photovoltaic systems

#### 3.3.2.1 System data

At the test site, there are 21 roof-mounted residential PV systems installed with an overall nominal power $P_{STC}$ = 233 kWp and ranging from 2.2 kWp to 47.84 kWp (named PV1 to PV21) each. The average nominal power per roof is 11.07 kWp and close to the average value for southern Germany according to Wirth *et al.* (2011). The PV systems are distributed in the overall test site and smart meters are installed at 12 PV systems providing 15 minutes average feed-in power values. The PV feed-in power is measured by Landis and Gyr *ZMD310* smart meters. This type is rated as class B according to DIN EN 50470-3 (2007) and the allowed calibration error limit by law for the 15-minute average energy value ranges from 2 % to 3 %. Experiences at the accredited calibration laboratory of SWU show errors lower than


Figure 3.3: Aerial image of the test site. The border of the test site is illustrated as a blue polygon. The PV systems equipped with smart meters are marked in red, others in blue. The position of the transformer station is marked embedded image. Airborne image © City of Ulm, measurement department

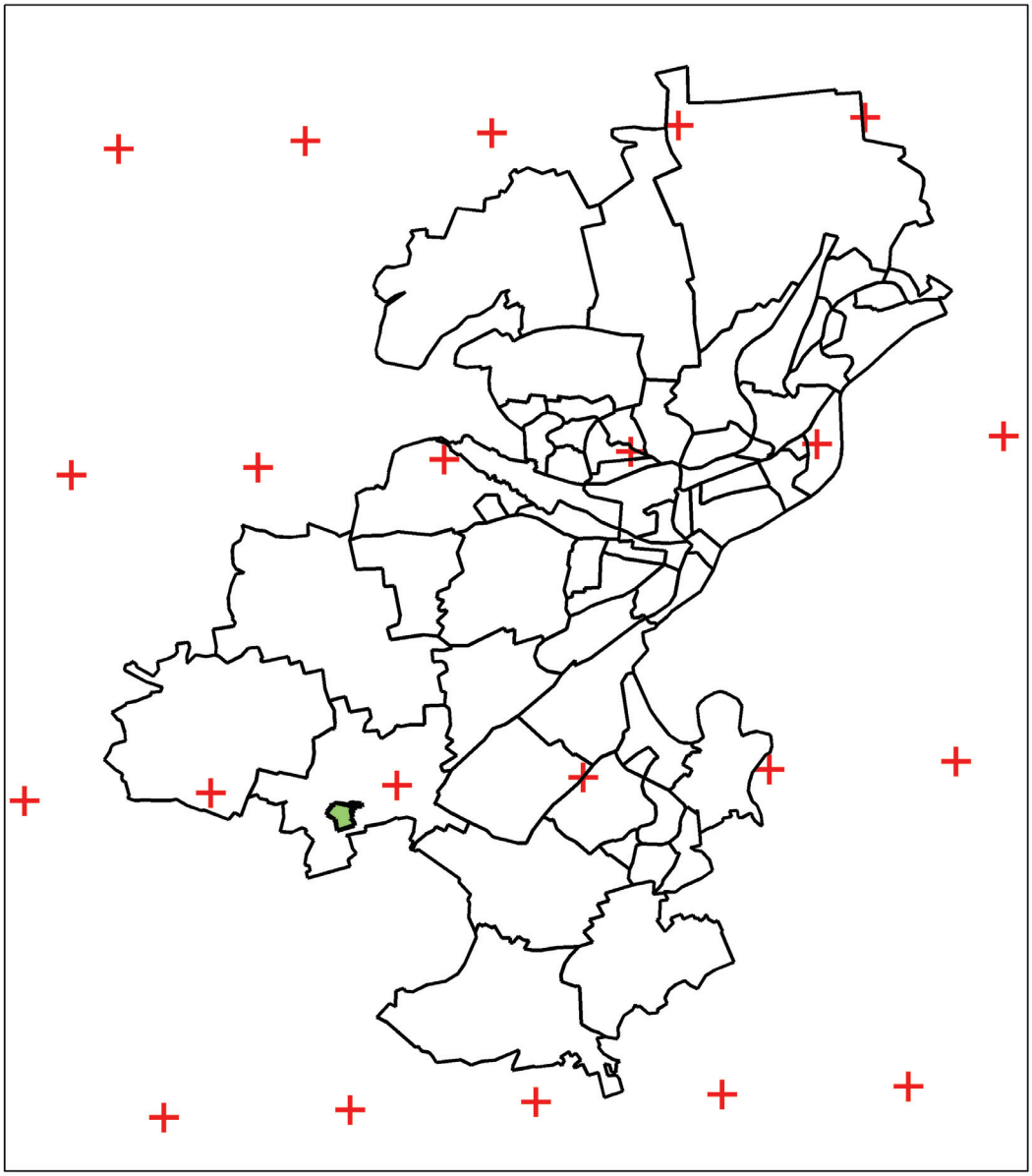

Figure 3.4: Relation of test site (green-filled polygon), the city districts of Ulm (black polygons) and MSG pixels (red crosses).

0.5 % (Katzmaier, 2015). The 12 smart meters were installed during a measurement campaign and have been in operation since $15^{th}$ May 2013.

Table 3.2 summarizes the nominal power of the PV systems and shows the PV systems with smart meters. The total monitored nominal power of the 12 measured PV systems is 152 kWp. This represents a fraction of 65 % of the overall installed PV power.

Table 3.2: $P_{STC}$ of the PV systems in the test site and available smart meter data. Note: PV14 and PV15 have only one common smart meter (marked with *).

| ***PV System*** | $P_{STC}$ ***[kWp]*** | ***Smart meter*** |
|---|---|---|
| PV1 | 47.8 | Yes |
| PV2 | 13 | Yes |
| PV3 | 5.5 | |
| PV4 | 12 | |
| PV5 | 13.2 | |
| PV6 | 2.2 | |
| PV7 | 9.6 | |
| PV8 | 9.6 | Yes |
| PV9 | 3.6 | |
| PV10 | 4.8 | Yes |
| PV11 | 4.4 | Yes |
| PV12 | 29.9 | |
| PV13 | 6.5 | Yes |
| PV14 | 8.6 | Yes* |
| PV15 | 2.9 | Yes* |
| PV16 | 7.8 | Yes |
| PV17 | 17 | Yes |
| PV18 | 10.6 | Yes |
| PV19 | 7.4 | Yes |
| PV20 | 8.2 | Yes |
| PV21 | 8.1 | Yes |

#### 3.3.2.2 PV system orientation

Usually, the DSO only knows the location and nominal power of the PV system. An optimal orientation (azimuth 180°, 30° tilt) is often assumed for grid planning. This assumption leads to a higher coincidence factor and increased errors (see section 5.1.3).

A manual data collection was done for the test site in 2012 to get more accurate data on the orientation of the PV systems. The angles are rounded to 5° instant values. The data from this collection are denoted as in-situ data.

Ruf *et al.* (2012a) suggest a new scheme for grid planning in distribution grids considering data from a solar power roof potential analysis. Such a roof potential analysis can be based on stereoscopic aerial images or laser scan data (denoted as LiDAR). The study shows the deviation of using stereoscopic aerial images by two examples and the higher accuracy using laser scan data. Therefore, the roof potential analysis for the solar cadaster[2] of the city of Ulm was created by using airborne laser-scan data from a flight in March 2013. The orientation of the PV systems at the test site are estimated by using manually defined masks in the azimuth and tilt angle data created from the laser-scan height profile. As orientation angles of the PV systems the median from all pixels inside the mask are taken into account and denoted as LiDAR mask.

The manual definition of masks could be done for a small number of PV systems inside a test site. The effort for several thousands of PV systems is too high. Therefore, a simple investigation window method to estimate the azimuth and tilt angle from given coordinates of the PV systems was proposed by Ruf *et al.* (2015). Instead of a mask a window with the size of 9 x 9 to 13 x 13 pixels are used to estimate the median of the PV system orientation angles. The error of the angles based on the laser-scan data is assumed as less than 10° because of the accuracy of the laser scanner. These orientation angle data are denoted as LiDAR window. The data from these three data sets are listed in Table 3.3. With the assumption of an optimal orientation there are four options which are taken into account: in-situ data, LiDAR mask, LiDAR window and optimal orientation.

### 3.3.3 Low voltage distribution grid

At the test site only the annual energy consumption of the households are available. The installation of smart meters for customers was delayed over several years because of the development of a smart meter protection profile to ensure the data safety and data security as well as the need for a cost-benefit analysis verifying the macroeconomic benefit (Kaufmann *et al.*, 2014). The annual consumption in the test site was 1,051 MWh in 2012. The annual consumption of residential consumers is 84.7 % of the overall consumption.

For this customer group the time series are generated with the standard load profile (see Section 2.5.1), the VDI-4655 reference load profile (see Section 2.5.2) and measured profiles (denoted as NoSLP) from another measurement campaign in Ulm (Heilscher *et al.*, 2010). The measured NoSLP profiles based on data from 145 randomly selected households in Ulm, monitored from May 2009 to April 2010.

[2] www.ulm.de/solarkataster/

Table 3.3: Various PV system orientation angles based on different measurement approaches

| ***PV System*** | ***azimuth [°]*** | | | ***tilt [°]*** | | |
|---|---|---|---|---|---|---|
| | ***in situ*** | ***LiDAR mask*** | ***LiDAR window*** | ***in situ*** | ***LiDAR mask*** | ***LiDAR window*** |
| PV1 | 80 | 90 | 90 | 20 | 24.9 | 24.1 |
| PV2 | 200 | 180 | 180 | 50 | 45.8 | 46.7 |
| PV3 | 170 | 180 | 171.8 | 45 | 50.2 | 50.4 |
| PV4 | 110 | 153.4 | 135 | 45 | 45.7 | 45.8 |
| PV5 | 200 | 206.5 | 198.4 | 40 | 39.6 | 38.3 |
| PV6 | 290 | 116.5 | 116.5 | 30 | 30.5 | 30.2 |
| PV7 | 210 | 198.4 | 191.3 | 40 | 41.7 | 44.4 |
| PV8 | 150 | 153.4 | 135 | 45 | 46 | 53.9 |
| PV9 | 180 | 180 | 153.4 | 45 | 42.9 | 35.3 |
| PV10 | 140 | 180 | 168.6 | 40 | 42.1 | 40.6 |
| PV11 | 140 | 180 | 180 | 40 | 42.7 | 43.3 |
| PV12 | 175 | 135 | 135 | 15 | 19.6 | 18.1 |
| PV13 | 155 | 153.4 | 113.2 | 45 | 44.6 | 34.7 |
| PV14 | 200 | 90 | 95.2 | 40 | 41.5 | 17.3 |
| PV15 | 200 | 180 | 180 | 40 | 36.3 | 36.7 |
| PV16 | 200 | 153.4 | 161.6 | 30 | 32.6 | 34.2 |
| PV17 | 230 | 206 | 206.6 | 30 | 34.6 | 34.6 |
| PV18 | 230 | 206 | 198.4 | 30 | 33.1 | 32.9 |
| PV19 | 165 | 153.4 | 156.8 | 35 | 35.2 | 36.6 |
| PV20 | 180 | 180 | 180 | 40 | 47.2 | 47.5 |
| PV21 | 245 | 243.4 | 233.1 | 40 | 41.9 | 42.3 |

The average time series of all these NoSLP profiles was rearranged with respect to the weekdays and weekends in 2012. The original consumptions range is from 0.5 MWh to 7.753 MWh with a mean of 2.739 MWh. Both SLP and NoSLP have a temporal resolution of 15 minutes.

The VDI profiles were developed for single buildings. The simple use of the VDI profiles for several houses leads to implausibly high coincidence factor with high peaks in the consumption. Therefore, the VDI profiles are randomly shifted for one hour following a Gaussian distribution. The Gaussian distribution is chosen to simulate the different times of the daily activities of household occupants (Ge *et al.*, 2015).

Agricultural consumers are assumed with the SLP load profile L0 and 3.7 % of the annual overall consumption. Commercial consumers are taken into account with G0 and G3 SLPs, respectively (6.7 % and 4.9 % of the annual consumption). A grid simulation considering only SLP consumption and no PV feed-in power shows a loss in the grid in the range of 2.17 % of the annual overall consumption.

For the load flow measurement at the transformer, a special data logger was developed at Ulm University of Applied Science based on a programmable logic control manufactured by Beckhoff GmbH. The device measures the current at each feeder line and the voltage at the low voltage bus bar in one-second time resolution. According to the accuracy of the used components a measuring error of approximately 3 % can be assumed.

## 3.4 Example for medium voltage transformer load flow simulations

### 3.4.1 Medium voltage feeder

The medium voltage feeder supplying the test site was investigated for scaling up the approach. Eleven other transformers are connected to this medium voltage feeder besides the transformer at the test site. The location of these transformers and the relation to the test site is illustrated in Figure 3.5. The substation is located far outside the investigated MSG pixel and does not have to be considered in the irradiance source setup because there are no further loads or generators between the substation location and the first transformer. All transformers in the suburban location are almost in the same MSG pixel or close to the border of the same pixel. The SEVIRI instrument has a spatial point spread function of the radiance detection with a overlap to the neighbourhood pixels (Deneke and Roebeling, 2010). There-

fore, the irradiance from the same pixel as for the test site can be used as assumption for the close transformers. Based on the availability of the validation data only irradiance from the MACC-RAD service is taken into account. In the investigated

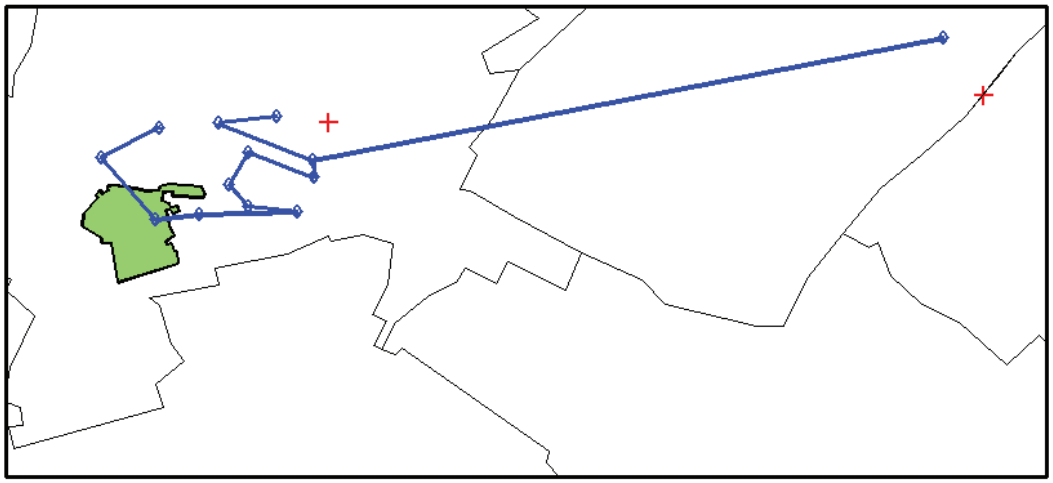

Figure 3.5: Overview about the test site (green-filled polygon) and its relation to the medium voltage grid. The blue diamond symbols mark the positions of the medium-to-low-voltage transformers. The blue diamond symbol on the right indicates the position of the substation. The blue lines illustrate the direct connection of the medium voltage feeder from one transformer to another. The red crosses indicate the corners of the MSG image pixels.

area, 112 PV systems with an overall nominal power $P_{STC} = 1{,}413\,\text{kWp}$ are connected to the low voltage grids supplied by the medium voltage feeder. The average $P_{STC}$ is 12.6 kWp ranging from 1.4 kWp to 119.6 kWp. The orientation and tilt angle of each PV system is estimated from laser-scan data with the LiDAR window approach (Ruf *et al.*, 2015). The median of orientation is 179.6° and tilt is 35.7°. The PV systems are allocated to the 12 medium-to-low voltage transformers by a nearest-neighbour approximation searching for minimum distance between the location of the transformer and the metering point. This approximation leads to an error for the single medium-to-low voltage transformers but is compensated at the higher aggregation level at the substation.

### 3.4.2 Load assumptions

Over 1,350 load customer metering points have been taken into consideration. These metering points are also allocated to the 12 medium-to-low voltage transformers by a nearest-neighbour approximation. The measured demand was 4,292 MWh in 2013 and 4,182 MWh in 2014. It is assumed that the distribution of the consumption at

each transformer is equal to the distribution in the test site, that is 84.7 % are residential consumers, 3.7 % are agricultural consumers and 11.6 % are commercial consumers (6.7 % assumed with G0 SLP and 4.9 % with G3 SLP). The measured NoSLP profiles are analysed to confirm the assumption. The maximum measured annual consumption within the NoSLP profiles is 7,753 kWh. If all metering points with a measured consumption of 7,753 kWh or less are related as households with H0 profile then this profile group is 87 % of the overall energy consumption. This percentage is close to the value from the test site.

In the medium voltage level analysis only SLP profiles are considered. Special load profiles e.g. for temperature-dependent electric heating, street lighting or mobile network transmission stations are not taken into account.

The grid losses at the low voltage level are assumed with 2.17 % of the annual overall consumption. Based on a grid simulation without PV the annual grid losses of the medium voltage level are 0.7 % of the annual consumption in this area and constant grid configuration. The losses of the power transformation between medium and low voltage grid are 1.34 % of the annual consumption (Freymiller, 2015).

### 3.4.3 Measured validation data

For validation, the load flow of the medium voltage feeder is measured at the substation since $11^{th}$ March 2013 to $13^{th}$ December 2014. Due to the fact that only the line current and line voltage of a single phase are measured at the substation, the load flow is defined as the absolute value of the active power. Reversal load flow cannot be detected because the measurement do not distinguish between the current directions. Furthermore, some assumptions has to be taken into account. First, a symmetric utilisation of all three lines is assumed. The 10-minute-averaged unbalance factor in the medium voltage level has to be below 0.7 % according to TAB (2008). Second, the displacement factor $cos\,\varphi$ is assumed with 0.9 inductive (TAB, 2008). With these assumptions the active power $P$ is given by

$$P = \sqrt{3} \cdot U_{L2} \cdot I_{L2} \cdot \cos\varphi. \tag{3.1}$$

The voltage $U_{L2}$ is the line voltage between the lines L1 and L2 and $I_{L2}$ is the apparent current of the line L2. Third, the configuration of the medium voltage grid is assumed as constant. Switching operations changes the consumption and generation by connecting additional transformer substations and low voltage grids.

The active power load flow based on the current and voltage measurements at

the substation is shown in Figure 3.6. This is the validation data set and it can be seen that there are two periods without measured data. These were caused by a failure at the data acquisition system. The periods are from $6^{th}$ July 2014 to $13^{th}$ July 2014 and from $12^{th}$ October 2014 to $26^{th}$ October 2014. Furthermore, there are three periods with outlier in the load flow. The two outliers in May 2013 and August 2014 are caused of maintenance activities of SWU (Mürdel, 2015). The reason for the third outlier period in October 2013 is unknown. All outliers and missing data periods are marked as non-valid and not considered in the validation. The load flow follows the annual cycle with high values during the winter because the higher demand and lower values during summer. The diurnal spread of the load flow is 50 kW to 600 kW in summer and 50 kW to 1,100 kW in winter. As mentioned before, the current measurement do not consider the current direction and negative load flows indicating a reversal load flow are not detected.

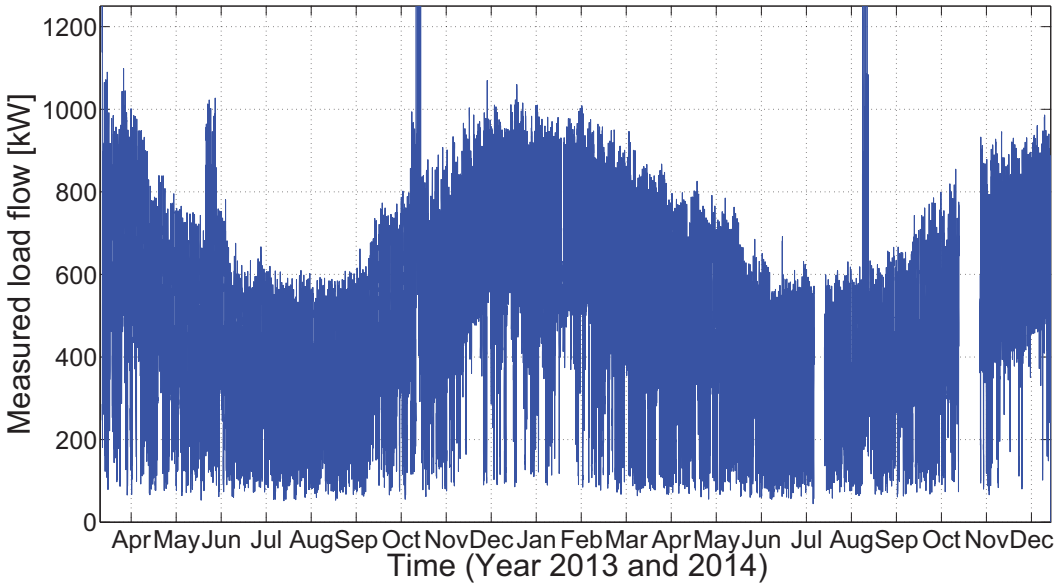


Figure 3.6: Absolute values of active power based on the current and voltage measurements at the substation. The $cos\,\varphi$ is assumed with 0.9 inductive.

# Chapter 4

# Method

This chapter describes the applied models and the validation approach to determine the results of the usage of satellite irradiance data for the load flow calculation at transformers.

## 4.1 Model description

The models to calculate the load flow at a low voltage transformer are described in this section. For the conversion of *GHI* into PV feed-in power the PV systems have to be described with a model providing a high accuracy. The load flow at the transformer is given by the time series of the PV feed-in power and the consumed power of the grid-connected loads.

### 4.1.1 Residential photovoltaic system model

For the calculation of the PV feed-in power several parameters are considered. The location (as longitude and latitude) and $P_{STC}$ are taken from the data of the DSO. The azimuth angle and tilt angle of the PV generator plane are taken from one of the data sets described in Section 3.3.2.2.

DSOs typically consider the orientation of PV systems for grid planning or operations, by using a theoretically optimum orientation for each system because they do not know any more details. However, often they even assume only a coincidence factor of the PV feed-in power (Pardatscher *et al.*, 2011). To ensure the applicability of this work from the DSO's perspective, the PV simulation model is also defined according to this currently applied approach. The consideration of multi-orientations would significantly increase the time and effort in identifying and modelling PV systems. This can be done manually for a small number of PV systems

like in the test site but not in a larger grid area as Ulm with more than 4,500 PV systems.

In this work only one orientation and inclination is used for the PV system. PV systems with different azimuth angles are not frequent. An optical inspection based on aerial images of 442 PV systems in Ulm shows that 39 PV systems (8.8 %) have two different azimuth angles and only 15 systems (3.4 %) have three or more orientation.

The required irradiance data are *GHI*, *DHI* and *BHI* delivered by the irradiance data sets (see Section 3.1). These irradiances are transferred into the tilted irradiance *GTI*. The beam part is translated according to equation 2.14. The diffuse part of the irradiance is calculated with the Reindl model (see Section 2.3.3.3). This model was chosen because of its stability using suboptimal input data (Gueymard, 2009) and its consideration of horizontal brightening and circumsolar diffuse irradiance.

The ground reflected part is calculated according to equation 2.16 assuming a constant albedo value of 0.2. This value is a usual assumption for Germany (Fath *et al.*, 2015) and in the range of common surface material e.g. grass, asphalt or soil (see Table 2.1).

The PV system simulation uses the calculated *GTI* and the air temperature to calculate the cell temperature reducing the efficiency of the PV array with rising *GTI* and air temperature. Several models exist to estimate the temperature influence (Skoplaki and Palyvos, 2009). In this work, the cell temperature is determined using the SAPM model according to King *et al.* (2004) because of the consistent module characteristic input data. The air temperature and wind speed are delivered by the meteorological station at the university campus. The cell temperature $T_{cell}$ is given by

$$T_{cell} = T_{module} + \frac{GTI}{GTI_{STC}} \Delta T, \tag{4.1}$$

where GTI is the irradiance in the module plane $GTI_{STC}$ as irradiance under STC (1000 $W/m^2$). The parameter $\Delta T$ is the empirical temperature difference between the cell and the module back surface at $GTI_{STC}$ and ranges between 2 and 3 K for on-roof mounted flat-plate modules (King *et al.*, 2004). $\Delta T$ is part of the module parameter set provided by Sandia for the PVLib (Stein, 2012). The module temperature $T_{module}$ is estimated by

$$T_{module} = G\left(e^{a+bv_{wind}}\right) + T, \tag{4.2}$$

where $T$ is the air temperature, $v_{wind}$ is the wind speed and $a$ and $b$ are the empirical coefficients depending on the module. The 2-meter air temperature from the meteo-

rological station of the university is used as $T$. The coefficient $a$ describes the upper limit for the module temperature at low wind speed and high irradiance conditions while $b$ describes the temperature decrease caused by increased wind speed (King *et al.*, 2004).

The non-linear PV module and inverter behaviour is considered using the SAPM and SGPI model (see Section 2.4). A simulation model for a reference PV system is setup, which will be scaled to $P_{STC}$ of each installed PV system. The chosen PV module type of the reference PV system is *Yingli Solar YL230-29b* together with one *Blueplanet 6400xi supreme* inverter produced by Kaco New Energy GmbH (Yingli, 2012; KACO, 2010). For the system modelling a poly-crystalline PV module model is selected from the PVLib library. This is justified by the fact that this technology is mostly used in Germany (Glunz *et al.*, 2012).

The real PV module string configurations of the single PV systems are unknown in this study. A typical string configuration for a residential system is assumed. This configuration leads to a PV system of 28 PV modules from the type as mentioned before, which are divided into two strings with 14 modules each. These two strings are connected to the PV inverter. The calculated output power time series of this reference PV system is normalized to the reference PV system nominal power under STC and scaled up to the nominal power of the installed PV modules at the test site.

In Germany, the recommendations for *NPR* vary from 0.85 for north-facing roofs and east-west-facing systems to 1 for optimally oriented PV systems (30 $^{\circ}$ tilted and facing south) (Albrecht and Schröder, 2013). Pardatscher *et al.* (2011) validates the use of this recommendation in a study considering 934 PV systems in Southern Germany with an average *NPR* of 0.89.

However, Zehner *et al.* (2010) and Luoma *et al.* (2012) show the amount of the energy contained in irradiance enhancements which should be considered in the *NPR* in future. Therefore, the *NPR* is set to 1.0.

Each PV system is treated with its individual orientation. However, the solar potential analysis provides no time series of shadows hence these are not taken into account because these data are not available for the test site.

In the simulation it is assumed that losses due to the system set-up (e.g. wiring losses) or due to the maximum power point tracker of the inverter are negligible. Typically, residential PV systems are designed such that the cable losses are below 1% of the rated power (Albrecht and Schröder, 2013). The efficiency of maximum power point tracker systems and DC/AC converters ranges from 96 to 99% (Bendib *et al.*, 2015). Both losses are within the tolerance of the PV module rating and not determinable without additional system-specific information. The PV feed-in power

is calculated for each single PV system as a time series in 15-minute resolution. Furthermore, the influence of PV system degradation is not considered because without detailed information about the installed PV module technology and type as well as the history of the ambient condition it is very complex to determine the correct degradation rate. There are various degradation rates and degradation modes in literature available ranging from 0.2% per annum to around 5% per annum (Gutnik *et al.*, 2012; Ndiaye *et al.*, 2013).

### 4.1.2 Transformer load flow model

This section describes the model used to calculate the load flow time-series at low voltage transformers for distribution grids with a high number of PV systems.

The load flow at the transformer $P_{Trafo}$ is the residuum of the consumption power $P_{Load}$ and $P_{PV}$ and is given by

$$P_{Trafo}(t) = P_{Load}(t) - P_{PV}(t). \tag{4.3}$$

$P_{Load}$ is given by

$$P_{Load}(t) = \left(1 + \frac{W_{loss}}{\sum_{k=1}^{M}\left(W_{Consumption,k}\right)}\right) \cdot \sum_{k=1}^{M}\left(\frac{W_{Consumption,k}}{\sum_{t=1}^{T} LP(t)_k} LP(t)_k\right), \tag{4.4}$$

where $W_{loss}$ is the annual loss energy within the grid, $M$ is the number of load profile classes, $W_{Consumption,k}$ is the annual consumption of all consumers inside the same load profile class $k$ and $LP$ (e.g H0, G0, G3 and L0 according to Fünfgeld and Tiedemann (2000)) is the corresponding load profile as time series. In this work, the $LP$ time series can be a SLP, NoSLP or VDI profile. $W_{Consumption,k}$ is defined by

$$W_{Consumption,k} = \sum_{j=1}^{C(k)} W_{Consumption,j}, \tag{4.5}$$

where $W_{Consumption,j}$ is the annual consumption of a consumer connected to the investigated grid area and classified as member of a load profile class $k$. $C(k)$ denotes the number of consumers inside a load profile class $k$. $W_{Consumption,j}$ is measured by the DSO with energy meters.

$W_{loss}$ is assumed as a constant value of 2.17 % of the annual consumption for the low voltage grid. The amount of $W_{loss}$ increase with the length of the lines and decrease with increasing cross section. An increasing number of PV systems

leads to a reduction of $W_{loss}$ to an optimum where the reduction can reach almost 20 % according to Bucher *et al.* (2013b). If the number of installed PV systems further increases $W_{loss}$ increases again. This can lead to higher values of $W_{loss}$ than without PV systems (Cohen and Callaway, 2016). This reduction and increase of $W_{loss}$ dependent on the installed PV systems is neglected in this work.

Furthermore, it is assumed that the separate phases of the three-phase power system are symmetrically loaded. The DSO is authorized to define further specifications and rules in the so-called technical connection conditions (TAB, 2008; TAB, 2009). These technical connection conditions prescribe the maximal non-symmetrical value of each phase.

As further assumption, no temperature-dependent load profiles are taken into account. The application of those load profiles requires information about installed heat pumps or night storage heating systems. DSOs know only consumers operating heat pumps and off-peak storage heating systems, respectively, if they concluded a contract on special electricity tariffs for such systems. However, due to the low price spread between the different peak and off-peak electricity tariffs as well as additional costs for metering there is a increasing number of such systems unknown to the DSO (Bärwaldt and Kurrat, 2008).

The PV feed-in power time-series $P_{PV}$ for a given PV system $i$ of $N$ systems is described by

$$P_{PV}(t) = \sum_{i=1}^{N} P_{STC,i} \cdot \frac{P_{ref}(GHI(t), T(t), WS(t), \alpha_T, \gamma_T)_i}{P_{STC,ref}}, \tag{4.6}$$

where $P_{STC,i}$ is the power, as rated by the manufacturer, of the PV system $i$. The power of the PV model $P_{ref}$ depends on the orientation of the system $i$ (described with $\alpha_T$ and $\gamma_T$), $GHI(t)_i$, air temperature $T(t)$ and wind speed $WS(t)$. It is normalized to the rated power of the reference system $P_{STC,ref}$ within the model. This is described in detail in Section 4.1.1. *GHI* values are taken from SOLEMI, HC3v4 and MACC-RAD. The calculation time step is 15 minutes.

The calculation approach is visualized in Figure 4.1. The upper line in the picture shows the calculation of $P_{PV}$ considering the *GHI*, $T$ and $WS$ as well as the PV system data namely $P_{STC}$, $\alpha_T$, $\gamma_T$ and the PV model. The next line shows the calculation of $P_{Trafo}$ by subtracting $P_{PV}$ from $P_{Load}$. The lower line shows the calculation of the $P_{Load}$ based on load profiles, the annual energy consumption and an estimated grid loss. $P_{Load}$ is approximated by using the SLP, NoSLP or VDI 4655 RLP time series for residential customers based on their annual consumption. The corresponding SLPs are used for both commercial and agricultural customers (see

Section 3.3.3).

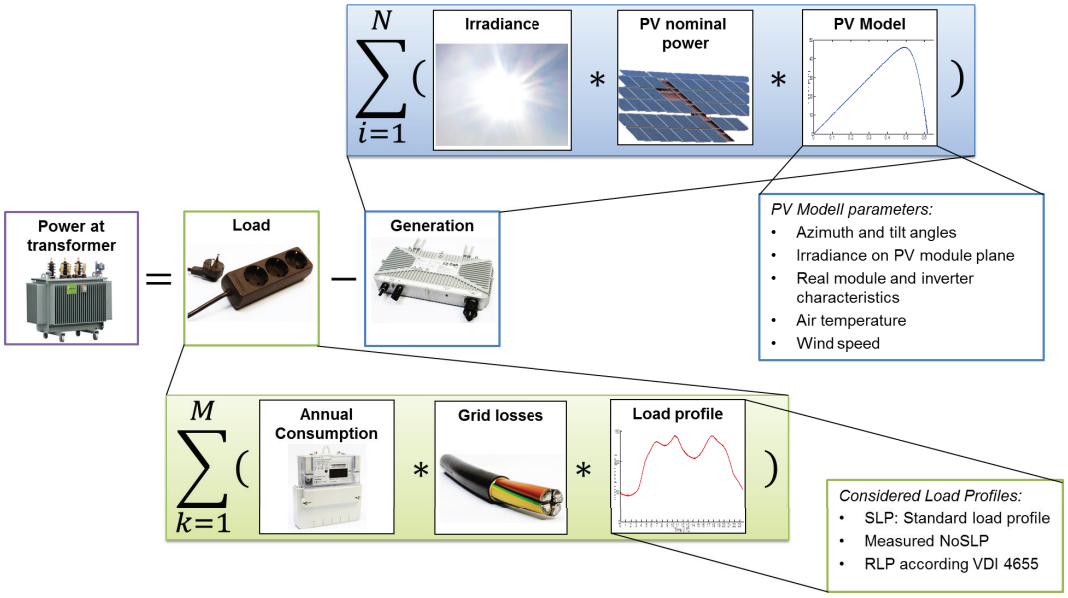


Figure 4.1: Scheme to calculate the power at a transformer in distribution grids with a high number of PV systems.

### 4.1.3 Aggregation to the medium voltage level

The calculation of the load flow at the medium voltage level is based on the transformer load flow model as described in the section before (Section 4.1.2). The load flow is calculated for each transformer connected to the medium voltage feeder. As mentioned in Section 3.4, the PV systems and consumer locations are allocated to the transformers by a nearest-neighbour assumption. The total active power time-series at the substation is given by

$$P_{Substation} = \sum_{j=1}^{N} P_{Trafo,j}. \tag{4.7}$$

The index $j$ is the number of the transformer in the range from 1 to $N$. For the medium voltage the annual loss energy within the grid $W_{loss}$ in equation 4.4 is assumed as a constant value of 4.21 % of the annual consumption. This value is made up of 2.17 % from the low voltage level, 0.7 % from the medium voltage level and 1.34 % from the transformation losses between medium and low voltage grid (see Section 3.3.3). These loss values are estimated by a grid simulation without PV feed-in power.

## 4.2 Validation scheme

This section introduces the different schemes for the data validation and analysis of the results. Besides the classical statistical measures, these are scores for the detection of events reaching a threshold and a variation analysis to determine the influence of different data sources and calculation models.

### 4.2.1 Statistical measures

The determination of the deviation between calculation and measured values as well as the comparison of different results require statistical key figures. The root-mean-squared error (*RMSE*), mean error (*ME*) and correlation coefficient (*CC*) are important statistical values to describe the accuracy of the approach and compare results. The relative values of *ME* and *RMSE* are rated to the mean values of the measurements and denoted as *rME* and *rRMSE*. Furthermore, *ME* and *RMSE* of the PV feed-in power calculation are normalized to the rated power of the PV systems to compare the results of different PV systems directly. These normalized statistical measures are denoted as *nME* and *nRMSE*. The definitions and equations are described in Section 9.1.

In analysing and comparing the results the *RMSE* is the most important statistical value because of the sensitivity to errors with high magnitudes. It is followed, in order of relevance, by *ME* and *CC* (Meier, 2014). Depending on the value, the *ME* can be interpreted as an additional threshold in the grid planning and operation e.g. utilization of assets or voltage band violations. The *CC* is useful for the comparison of different simulation models with real values.

### 4.2.2 Event detection scores

For single PV systems, DSOs are interested in the questions of whether the specific PV system reaches a defined PV feed-in power threshold e.g. 70 % or 100 % of $P_{STC}$ or whether the voltage at the connection point exceeds a defined value. In Germany, this voltage threshold is related to different voltage values e.g. change of voltage not more than 3 % in cases without PV feed-in power (VDE-AR-N 4105, 2011) or 10 % of the nominal voltage (DIN EN 50160, 2011). The 70 % feed-in power threshold depends on §6 of EEG (2014). This law calling for PV systems up to 30 kWp nominal power to either generally reduce their maximum feed-in power to this threshold or have to install a feed-in management system which is remotely controllable by the responsible DSO. Furthermore, the possibility of 100 % feed-

in power depends on various system-specific parameters e.g. NPR or irradiance enhancements caused by special cloud formations. However, the quantifying of irradiance enhancement driven energy yield requires data with a very high temporal resolution (Zehner *et al.*, 2010). Therefore, this is not in the scope of this work. The presented approach is not able to calculate voltages. This voltage calculation requires a detailed grid simulation with information about the grid topology, length and types of the lines and is also beyond the scope of this work. The investigated question for the PV systems is the occurrence of feed-in power larger than 70 % of the PV system nominal power.

Relevant binary questions at the transformer level for grid planning and operation are: does the utilization exceed 90 % of the nominal transformer power, do reversal load flows occur or does the oil reach the maximum temperature (Meier, 2014; DIN IEC 60076-7, 2008)? These indicators for the transformer state are useful as input for a feed-in management control system or grid planning systems. However, the calculation of the oil temperature as function of the load flow requires a detailed thermal transformer model taking into account the transformer-housing properties and meteorological parameters e.g. air temperature, solar irradiance and wind speed. This model is the objective of recent research (e.g. Stakic *et al.*, 2015). Furthermore, the analysis of the measured data in 1-minute resolution shows that the utilization did not exceed the 90 % nominal transformer power. The question investigated in this work is the occurrence of reversal load flows.

The verification and assessment of such event detection techniques could be solved by using statistical values based on contingency tables. Those statistical values, denoted as scores, are state-of-the-art key performance indicators in the performance analysis and comparison of forecasts but also useful in the assessment of remotely sensed measurements (Wilks, 2011). Scores used to describe the threshold detection are proportion correct (*PC*), threat score ($THS$), false alarm rate (*FAR*), contingency table bias ($CTB$), probability of detection (*POD*) and probability of false detection ($POFD$).

The *PC* and $THS$ indicate the accuracy between calculation and measured events. *PC* considers both ”yes” and ”no” events in the same way and leads to satisfying results if both occur equally. However, if the ”yes” event is rare $THS$ should be considered because $THS$ can be viewed as a *PC* for analysis after removing correct ”no” events from consideration. For both *PC* and $THS$ is 0.0 the worst result and 1.0 the best possible result (Wilks, 2011). The *FAR* describes the ratio of computed events which do not occur. The best possible *FAR* is 0.0, and the worst possible *FAR* is 1.0, therefore a smaller value of *FAR* is preferred. $CTB$ is the comparison

of the average calculation with the average observation and represents the ratio of the numbers of ”yes” calculations with the number of ”yes” observations. An unbiased calculation offers a $CTB = 1$, while $CTB > 1$ indicates that the event was computed more often than observed. $CTB < 1$ indicates that the event was computed less often than observed. The *POD* describes the ratio of the number of events computed and occurred to the number of all events observed. Furthermore, $POFD$ describes the ratio of the number of events computed but not occurred to the number of all situations where the event was not observed. The definitions and calculations of the different scores are described in Section 9.2.

### 4.2.3 Variation analysis

As shown in chapter 2, various models for the calculation of *GHI* from satellite images, computation of $DTI$, approximation of the PV cell temperature and simulation of PV system components exist. Several models with different complexities are taken into account by the variation analysis. This analysis quantifies the impact of the different models on the proposed scheme. The variation analysis is done for the PV fleet equipped with the smart meters and the transformer load flow calculation. The various calculation results are expressed in the statistical measures (see Section 4.2.1).

Figure 4.2 illustrates the set-up of the PV feed-in power variation analyses of the PV fleet. The red arrows highlight the proposed calculation scheme. Two irradiance sources are taken into consideration, the satellite-derived irradiance from MACC-RAD (see Section 3.1) and the ground-measured irradiance from the university meteorological station (see Section 3.2).

The sun position is calculated with four different algorithms, namely DIN 5034-2 (1985), Sandias ephemeris approximation (Stein, 2012), the solar position algorithm (SPA) (Reda and Andreas, 2004, 2007) and the Solar-Geometry-2 algorithm (Blanc and Wald, 2012). Furthermore, four alternatives for the PV system orientation are considered, namely in-situ measurement, the orientation angles from laser-scan data (using a mask and a window function) and an assumed optimal orientation. The details can be found in Section 3.3.2.2. The computation of the diffuse part of irradiance on a tilted plane is performed by the isotropic model (see Section 2.3.3.2) while the Reindl and Perez models are representatives for anisotropic models (Section 2.3.3.3), (Perez *et al.*, 1990). For the estimation of the PV cell temperature three approximations are considered (Faiman, 2008; King *et al.*, 2004; DGS, 2012) using the 2m air temperature. The calculation of the DC power of the PV generator is performed with a simple linear PV module model and the SAPM

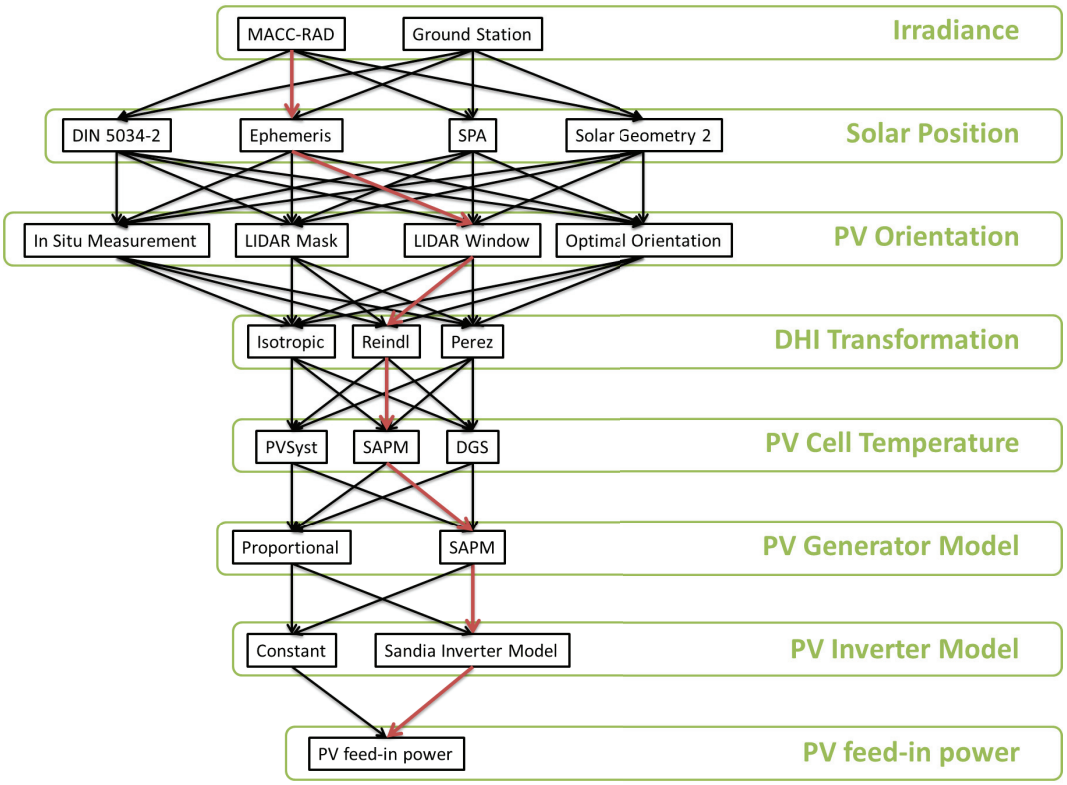


Figure 4.2: Scheme of the variation analyses for PV systems. The proposed path is highlighted in red.

(King *et al.*, 2004). The linear model assumes a linear relation of irradiance and output power and does not consider the non-linear characteristic of PV modules. The characteristic of the PV inverter is also taken into account using two different models. These are a simple model with a constant efficiency of 95.5 % as average value of the European inverter efficiency and the SGPI model describebd in Section 2.4.3 (King *et al.*, 2007). These numbers of variants lead to 1152 variations to calculate the PV feed-in power. Each variation result is compared with the measured PV feed-in power of the PV systems at the test site. The results are expressed in the statistical measures *RMSE*, *ME* and *CC* as well as *nRMSE* and *nME*.

The scheme for the variation analysis of the transformer load flow calculation is shown in Figure 4.3. The investigated irradiance sources are the three satellite services SOLEMI, HC3v4 and MACC-RAD. The calculation of the PV feed-in power is undertaken as described in Section 4.1.1. Furthermore, three load profiles for private households are taken into account namely SLP, NoSLP and VDI (see Section 2.5 and 3.3.3). These numbers of variants lead to nine variations to calculate the load flow at the transformer. The calculation of the PV feed-in power is based on the PV model described in Section 4.1.1. Each variation result is compared with the measured load flow at the transformer at the test site. The results are expressed in the statistical measures *RMSE*, *ME* and *CC*.

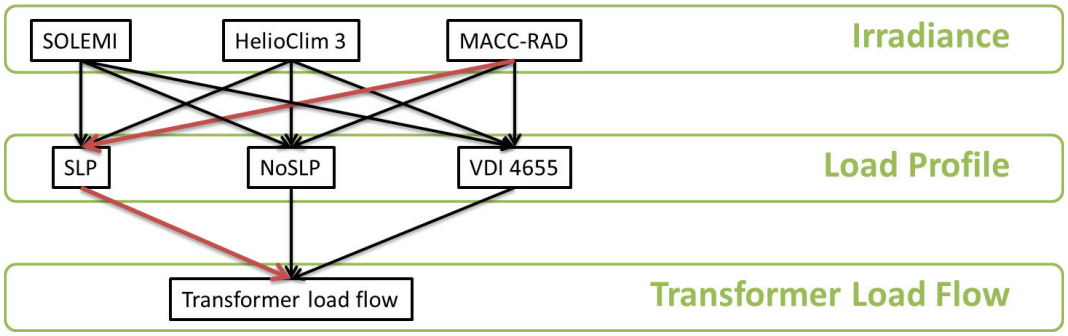


Figure 4.3: Scheme of the variation analyses for transformer load flow. The proposed path is highlighted in red. The PV feed-in power is only computed with the proposed approach and algorithms.

# Chapter 5

# Application in the Distribution Grid

This chapter shows the application of the proposed scheme to calculate the PV feed-in power of residential PV systems, the load flow at a low voltage transformer and the load flow of a medium voltage feeder at a test site in Ulm, Germany. Each calculation result is compared with measurements to determine the accuracy of the approach.

## 5.1 PV feed-in power simulation

This section describes the validation of satellite-based calculations of PV feed-in power versus the smart meter measurements obtained at each PV system. The statistical measures are discussed at the level of the single PV systems within the test site. The calculation objectives are the magnitude of the PV feed-in power, the detection of reaching PV feed-in power thresholds and the stability on variation of the methods and algorithms used.

The analysis of the calculated feed-in power and the comparison with measured feed-in power is performed with MACC-RAD and ground-based irradiance data.

### 5.1.1 Results of the proposed simulation scheme

The simulation model as described in Section 4.1.1 uses the satellite irradiance and the PV system-depending parameters e.g. orientation and nominal power to calculate the instant PV feed-in power. This PV feed-in power is calculated for each PV system and summed. This sum represents the PV feed-in power of the PV fleet as part of the load flow at the transformer.

The scatter plots in Figure 5.1 show the 15 minute averages of both the calculation and measurement for each PV system at the test site which are equipped with

feed-in power smart meters. There is a positive correlation of the calculated and measured data.

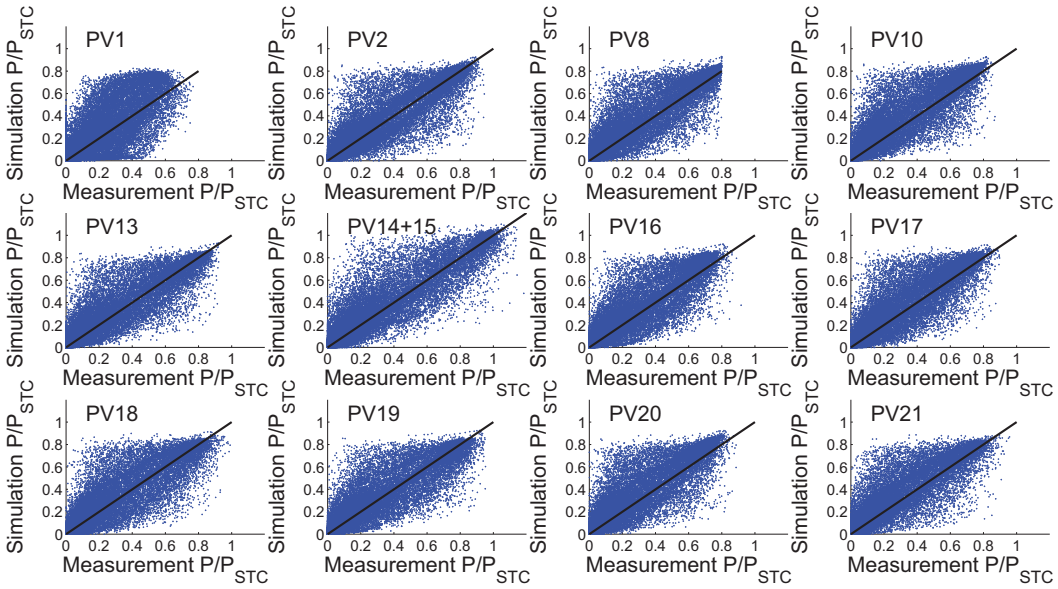


Figure 5.1: Comparison of calculated and measured PV feed-in power normalized to $P_{STC}$ of each PV system. The measured values refer to the x-axis and calculated values refer to the y-axis. The black line indicates the main diagonal.

All systems show positive biases, but PV1 obviously differs from the other systems because of an East-West orientation. The aerial image confirms a majority of PV modules on the western roof. The simulation model uses a single tilt and azimuth angle for each PV system which leads to a low correlation with the real measured values.

For PV8 the measured data show an abrupt limitation of the feed-in power. This could occur because of an active feed-in limitation of this PV system to 70 % of the rated power, according to an amendment in the EEG (2014). The amendment calls for a limitation of the feed-in power to a fraction of the nominal power if no device for external control is installed (EEG, 2014). Furthermore, it can occur because of a low *NPR* value resulting in a PV feed-in power limitation by the nominal power of the inverter.

The combined PV system (PV14 + PV15) is the only system that reaches a PV feed-in power of more than the nominal power. Both PV systems are separately calculated and the PV feed-in power combined afterwards.

The detailed statistical results of the calculated PV feed-in power are listed in Table 5.1. The *ME* ranges from 0.21 kW to 0.89 kW with an additional outlier of 2.63 kW at PV1 due to its two-sided orientation. Overall, this results in a mean

*ME* for all systems of 0.59 kW. The *RMSE* range is from 0.65 kW to 2.27 kW with the PV1-based outlier of 7.67 kW and the overall average of 1.76 kW. The *CC* is around 0.88 with the outlier of 0.75 for PV1. The accumulated PV feed-in power of the fleet at transformer level results in *ME* of 7.12 kW and *RMSE* of 18.73 kW, while the *CC* is 0.87.

Furthermore, the *ME* and *RMSE* is normalized to $P_{STC}$ of each PV system in order to compare the results. Thes measures are denoted as *nME* and *nRMSE*, respectively. The *nME* ranges from 0.03 kW/kWp to 0.06 kW/kWp with a mean of 0.05 kW/kWp. The *nRMSE* ranges from 0.12 kW/kWp to 0.16 kW/kWp with a mean of 0.14 kW/kWp.

The normalized values show that the errors are independent of the PV system size and satisfying for residential PV simulations. The values are sufficient for grid planning issues and the positive *ME* is considered as an additional margin of safety threshold in grid operation (Meier, 2014).

Table 5.1: Statistical measures of calculated PV feed-in power compared with measured PV feed-in power.

| ***PV System*** | ***ME [kW]*** | ***RMSE [kW]*** | ***rME [%]*** | ***rRMSE [%]*** | ***nME [kW/kWp]*** | ***nRMSE [kW/kWp]*** | ***CC*** |
|---|---|---|---|---|---|---|---|
| PV1 | 2.63 | 7.67 | 28.7 | 83.7 | 0.05 | 0.16 | 0.75 |
| PV2 | 0.39 | 1.67 | 12.1 | 51.5 | 0.03 | 0.13 | 0.89 |
| PV8 | 0.44 | 1.22 | 20.5 | 56.4 | 0.05 | 0.13 | 0.89 |
| PV10 | 0.29 | 0.65 | 27.1 | 61.5 | 0.06 | 0.14 | 0.89 |
| PV13 | 0.24 | 0.81 | 15.7 | 52.9 | 0.04 | 0.12 | 0.89 |
| PV14+15 | 0.39 | 1.24 | 16.2 | 51.8 | 0.04 | 0.14 | 0.89 |
| PV16 | 0.37 | 1.01 | 20.4 | 55.8 | 0.05 | 0.13 | 0.89 |
| PV17 | 0.89 | 2.27 | 22.4 | 57.2 | 0.05 | 0.13 | 0.88 |
| PV18 | 0.37 | 1.4 | 13.9 | 53 | 0.04 | 0.13 | 0.88 |
| PV19 | 0.21 | 0.93 | 11.7 | 50.7 | 0.03 | 0.13 | 0.89 |
| PV20 | 0.5 | 1.14 | 27.8 | 63.7 | 0.06 | 0.14 | 0.88 |
| PV21 | 0.41 | 1.06 | 23.8 | 61.3 | 0.05 | 0.13 | 0.88 |
| PV Fleet | 7.12 | 18.73 | 21.4 | 56.2 | 0.05 | 0.13 | 0.87 |
| Mean w/o PV1 | 0.41 | 1.22 | 19.2 | 56.0 | 0.04 | 0.13 | 0.89 |

### 5.1.2 PV feed-in power threshold exceedance monitoring

In this section, the correct calculation of the occurence of feed-in power values of single PV systems and the overall PV fleet higher than the defined PV feed-in power threshold of 70 % of $P_{STC}$ is analysed.

The scores (see Section 4.2.2) in which PV feed-in power exceeds single PV and PV fleet thresholds are presented in Table 5.2.

The feed-in power of PV1 rarely reaches 70 % of the rated PV power and leads to invalid scores. Therefore, PV1 is an outlier in the threshold exceedance monitoring analysis. The *PC* shows a high detection rate above 0.91 of the threshold exceedance for all PV systems including PV1. The $THS$ is in the range from 0.28 to 0.59 with an outlier of 0.004 for the PV1 system. The average $THS$ without PV 1 is 0.42 while it is 0.16 for the whole PV fleet. The *FAR* ranges from 0.33 to 0.71 and has a mean of 0.56 with an outlier of 1.00 for PV1. For the PV fleet $FAR = 0.83$. The $CTB$ is larger than 1.0 for each system meaning the detection has been overestimated. This means that the detection of $P_{STC}$ exceeding 70 % is calculated more often than it actually occurs. The *POD* shows values of at least 74 % for single PV systems with an outlier for PV 1. The overall *POD* for the PV fleet is 66 %. The $POFD$ is in the range from 5 % to 9 % for single PV systems. The $POFD$ for the PV fleet is 6 %. Therefore, the possibility of PV feed-in power threshold detection should be considered with care as a systematic overestimation is found. However, this error will result in excessive grid reinforcement. At least, any planning based on this scheme will not compromise the grid security.

Table 5.2: Scores of PV feed-in power reaching 70 % $P_{STC}$ threshold.

| ***PV System*** | ***PC*** | ***THS*** | ***FAR*** | ***B*** | ***POD*** | ***POFD*** |
|---|---|---|---|---|---|---|
| PV1 | 0.94 | 0.004 | 1 | 36.98 | 0.14 | 0.06 |
| PV2 | 0.93 | 0.5 | 0.4 | 1.26 | 0.75 | 0.05 |
| PV8 | 0.93 | 0.43 | 0.52 | 1.75 | 0.83 | 0.06 |
| PV10 | 0.91 | 0.31 | 0.67 | 2.54 | 0.84 | 0.09 |
| PV13 | 0.93 | 0.5 | 0.41 | 1.31 | 0.77 | 0.05 |
| PV14+15 | 0.93 | 0.59 | 0.33 | 1.25 | 0.83 | 0.06 |
| PV16 | 0.91 | 0.28 | 0.7 | 2.74 | 0.82 | 0.08 |
| PV17 | 0.92 | 0.35 | 0.62 | 2.23 | 0.84 | 0.08 |
| PV18 | 0.93 | 0.47 | 0.44 | 1.36 | 0.76 | 0.06 |
| PV19 | 0.93 | 0.52 | 0.37 | 1.17 | 0.74 | 0.05 |
| PV20 | 0.91 | 0.28 | 0.71 | 2.78 | 0.82 | 0.09 |
| PV21 | 0.94 | 0.4 | 0.56 | 1.81 | 0.8 | 0.05 |
| PV Fleet | 0.93 | 0.16 | 0.83 | 3.89 | 0.66 | 0.06 |
| Mean w/o PV1 | 0.92 | 0.42 | 0.52 | 1.83 | 0.80 | 0.06 |

### 5.1.3 Stability versus algorithm variation

The variation analysis shows the influence of different models and data sources on the accuracy of the PV simulation and its results (see Section 4.2.3).

The results are expressed in statistical measures normalized to $P_{STC}$ and visualized with scatter plots. Each point within those scatter plots is the result of the comparison of the calculated and measured PV feed-in power of the PV fleet for one of the 1152 investigated variations. The result points express the normalized *ME* (*nME*, x-coordinate) and normalized *RMSE* (*nRMSE*, y-coordinate) as well as the colour-coded *CC*. The results of the different algorithms are marked with different symbols. A perfect result would have a $nRMSE = 0.0$ kW/kWp, $nME = 0.0$ kW/kWp and $CC = 1.0$.

The results show a strong influence of the applied PV generator model. This is illustrated in Figure 5.2.

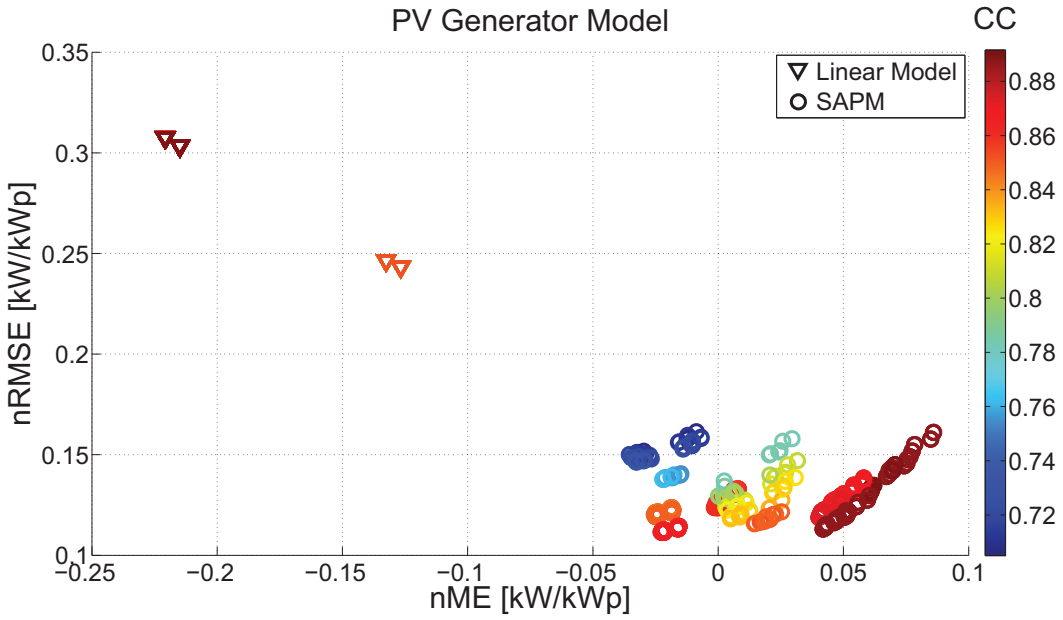


Figure 5.2: Variation of the PV generator model considering linear relation model and SAPM model. The upside-down triangles show the results taking into account the linear PV generator model while the circles show the results considering the SAPM. The result points express the normalized *ME* (*nME*, x-coordinate) and normalized *RMSE* (*nRMSE*, y-coordinate) as well as the colour-coded *CC*. Blue colour represents a low *CC* and red colour a high *CC*.

The linear PV model shows two groups of calculation results in the range of *nRMSE* from 0.24 to 0.32 kW/kWp and *nME* from -0.23 to -0.13 kW/kWp. The *CC* is higher than 0.84. The results using SAPM are in the range of *nRMSE* from 0.11 to 0.17 kW/kWp and *nME* from -0.04 to 0.08 kW/kWp. The *CC* ranges from

0.7 to 0.9. Only the results of the calculations using SAPM are further presented and investigated due to the linear PV model is not suitable.

In the first stage of the variation analysis the irradiance source measurement is varied. The results are presented in Figure 5.3.

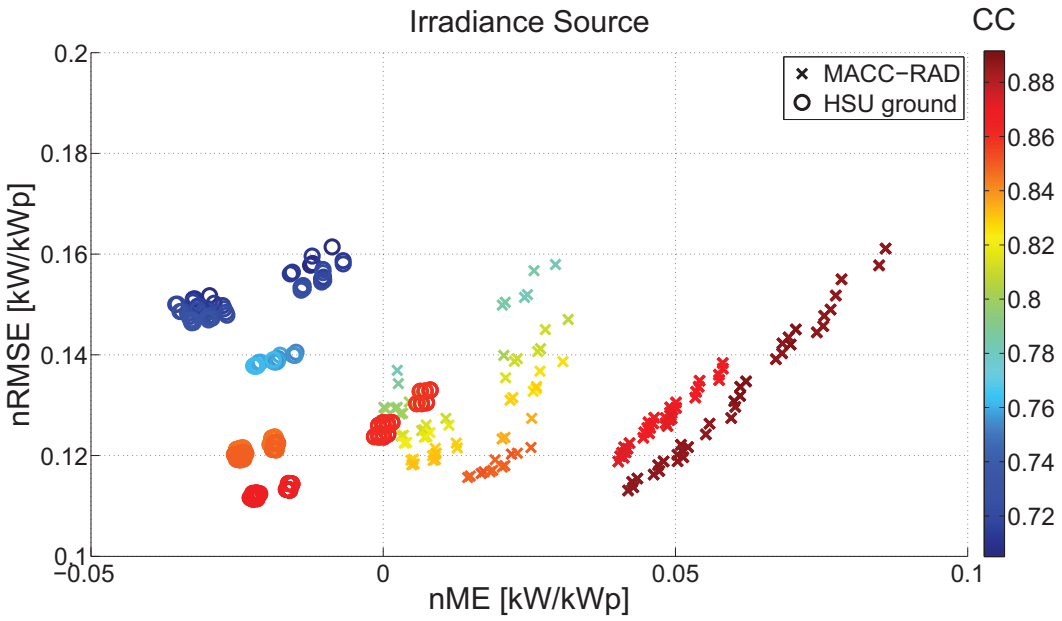


Figure 5.3: Variation of the irradiance source considering GHI ground measurements and MACC-RAD. The calculation results using the satellite irradiance data from MACC-RAD are marked with diagonal crosses while the results calculated with the ground measurements with data from the university campus are marked with circles. The result points express the normalized *ME* (*nME*, x-coordinate) and normalized *RMSE* (*nRMSE*, y-coordinate) as well as the colour-coded *CC*. Blue colour represents a low *CC* and red colour a high *CC*.

The MACC-RAD results are in the range of *nRMSE* from 0.11 to 0.17 kW/kWp and *nME* from 0 to 0.08 kW/kWp. The *CC* ranges from 0.77 to 0.9. The ground measurement results are in the range of *nRMSE* from 0.11 to 0.165 kW/kWp and *nME* from -0.03 to 0.01 kW/kWp. The *CC* ranges from 0.7 to 0.86. The *nRMSE* values of MACC are in the same range as the ground measurements but show a higher *nME*. This positive *nME* is also visible in the direct comparison (see Section 3.1). Normally, satellite irradiance data have a higher *nRMSE* compared with ground measurements. Ground measurements are point measurements only and do not fully represent the natural spatial and temporal variability of a distributed PV fleet in an area. In contrast, satellite-based irradiances provide the spatial information, but with restrictions in the available spatial and temporal resolution with their km sized pixels and their 5 to 15 minute temporally resolved observation scheme.

The *nRMSE* of the ground measurements increases with the distance to the location from the PV fleet. However, if the distance of the ground station is too large, the usage of satellite-irradiance is recommended (Zelenka *et al.*, 1999).

The next stage is the variation of the sun position calculation algorithms. The results are plotted in Figure 5.4.

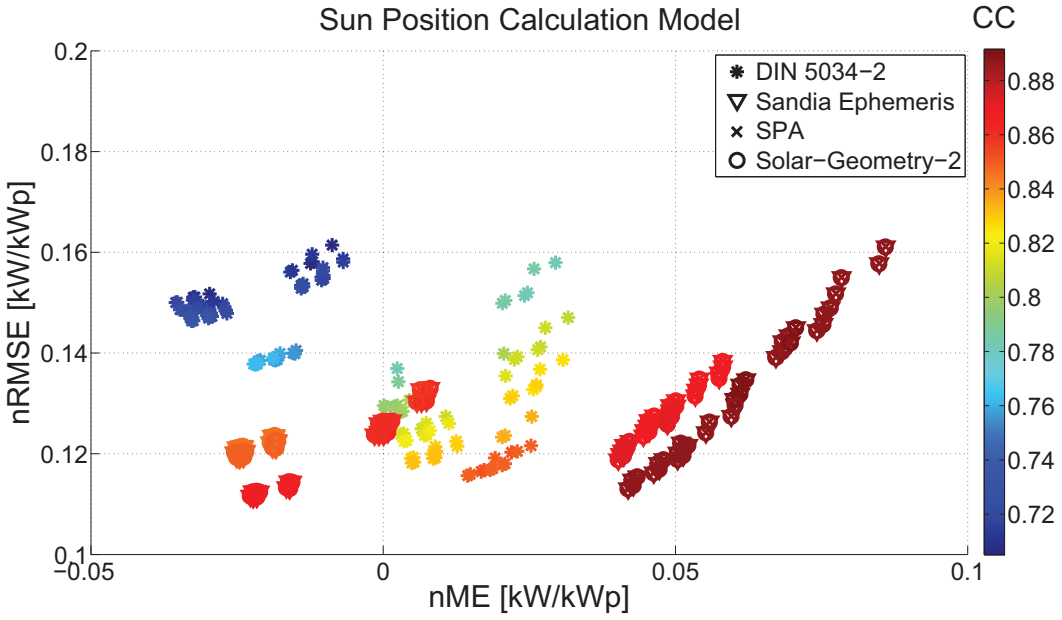


Figure 5.4: Variation of the sun position calculation algorithm considering DIN 5034-2 (stars), Sandias ephemeris (upside-down triangles), SPA (diagonal crosses) and Solar-Geometry-2 (circles). The result points express the normalized *ME* (*nME*, x-coordinate) and normalized *RMSE* (*nRMSE*, y-coordinate) as well as the colour-coded *CC*. Blue colour represents a low *CC* and red colour a high *CC*.

The results using Sandia ephemeris, SPA and Solar-Geometry-2 show only a small deviation from one another in the range of *nRMSE* from 0.11 to 0.17 kW/kWp and *nME* from -0.02 to 0.08 kW/kWp. The *CC*s are at least 0.84. However, the results of the DIN 5034-2 algorithm also show deviations compared to the other three algorithms. The DIN algorithm is in the range of *nRMSE* from 0.12 to 0.17 kW/kWp and *nME* from -0.03 to 0.03 kW/kWp. The *CC*s range from 0.7 to 0.85.

The orientation (azimuth and tilt angles) of the PV system influence the accuracy of the simulation in a small area like the investigated test site. The influence of the orientation on the overall PV feed-in power results of the PV fleet is shown in Figure 5.5.

The results using the in-situ orientation show only small deviations from one another in the range of *nRMSE* from 0.11 to 0.14 kW/kWp and *nME* from -0.03 to

0.06 kW/kWp. The *CC*s range between 0.76 to 0.9. It is visible that these areas with small deviations from one another have similar shapes as the groups of the LiDAR results but show a tendency to lower *nRMSE* values.

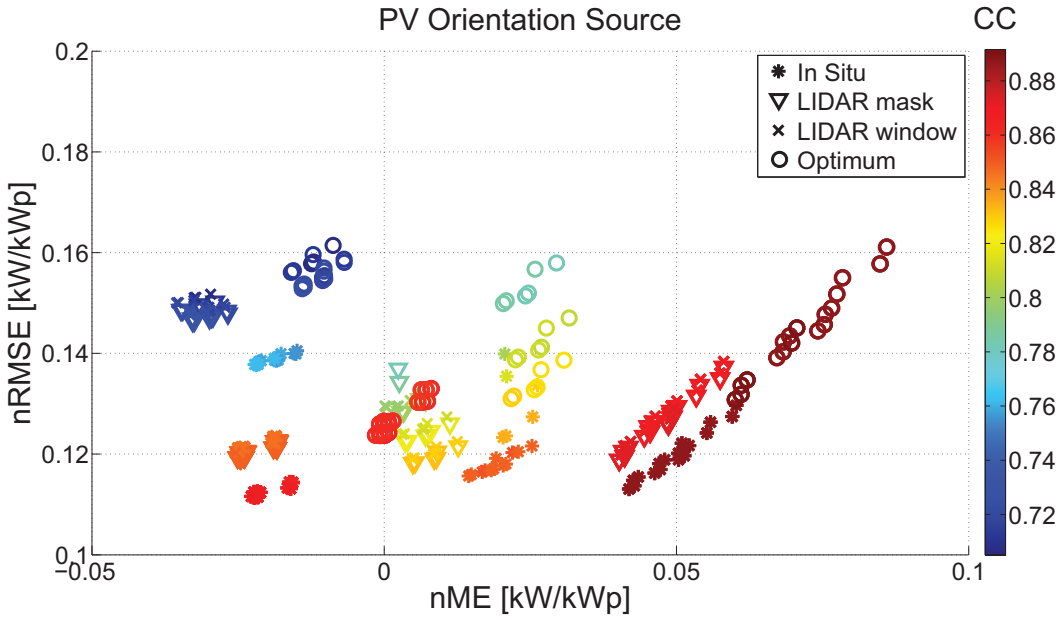


Figure 5.5: Variation of the PV generator orientation angle source considering in situ (stars), LiDAR mask (upside-down triangles), LiDAR window (diagonal crosses) and assumed optimal orientation (circles). The result points express the normalized *ME* (*nME*, x-coordinate) and normalized *RMSE* (*nRMSE*, y-coordinate) as well as the colour-coded *CC*. Blue colour represents a low *CC* and red colour a high *CC*.

The results of both LiDAR mask and LiDAR window are close together on the graph with minor differences. The LiDAR window results tend toward higher *nRMSE* values. Both are in the range of *nRMSE* from 0.12 to 0.15 kW/kWp and *nME* from -0.03 to 0.06 kW/kWp. The *CC*s are from 0.70 to 0.86.

The assumed optimal orientation also results in groups with similar shapes as the LiDAR results. However, these results have increased *nRMSE* and *nME* values. The optimal orientation results are in the range of *nRMSE* from 0.12 to 0.16 kW/kWp and *nME* from -0.02 to 0.08 kW/kWp. The *CC*s range from 0.70 to 0.9.

For single PV systems, the orientation angle has a stronger impact on the PV feed-in power calculation accuracy than for a PV fleet where errors can be compensated. For the proposed model in Section 3.3.2.2 considering the LiDAR window data the *nME* ranges from 0.03 kW/kWp to 0.06 kW/kWp with a mean of 0.05 kW/kWp. The *nRMSE* ranges from 0.12 kW/kWp to 0.16 kW/kWp with a

mean of 0.14 kW/kWp. Making assumptions about optimal orientation of the PV system increases the errors. Namely, the normalized *nME* ranges from 0.04 kW/kWp to 0.11 kW/kWp with a mean of 0.06 kW/kWp while the normalized *nRMSE* ranges from 0.13 kW/kWp to 0.22 kW/kWp with a mean of 0.15 kW/kWp.

The variation of the *DTI* calculation models is limited to three: the isotropic, the model according to Reindl and the Perez model. The isotropic model is the simplest *DTI* model and used in commercial grid simulation tools (e.g. DIgSILENT, 2014). Both the Reindl and Perez model are taken into account because of their high accuracy in calculations (Gueymard, 2009). Further models are not taken into account to reduce the number of variations. The results of the variation of the *DTI* models are shown in Figure 5.6.

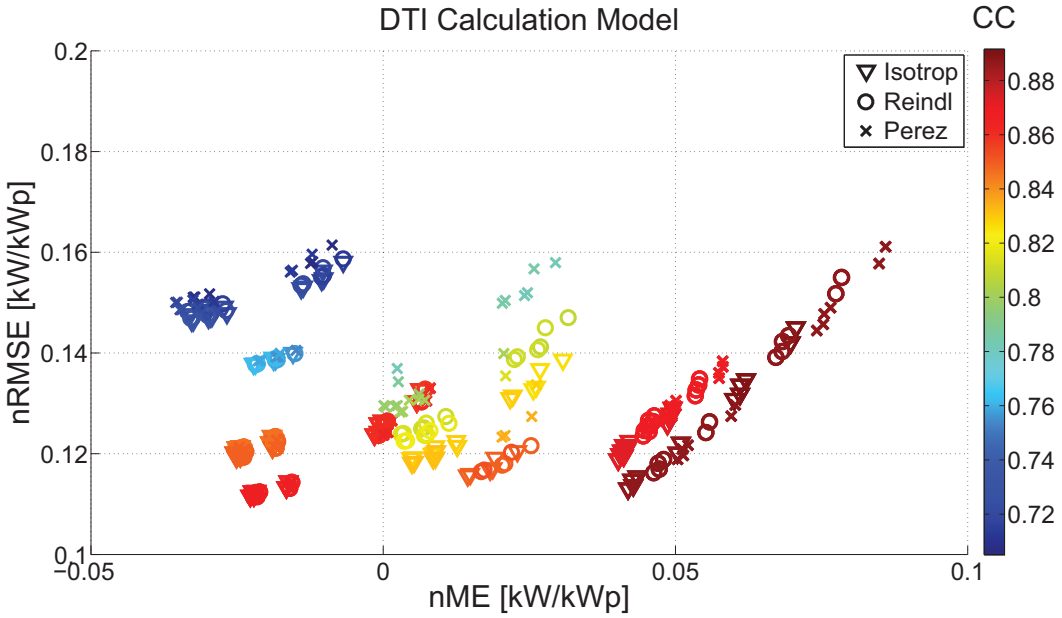


Figure 5.6: Variation of the *DTI* calculation model considering the isotropic model (upside-down triangles), Reindl (circles) and Perez models (diagonal crosses). The result points express the normalized *ME* (*nME*, x-coordinate) and normalized *RMSE* (*nRMSE*, y-coordinate) as well as the colour-coded *CC*. Blue colour represents a low *CC* and red colour a high *CC*.

The results using the isotropic model show only a small deviation from one another in the range of *nRMSE* from 0.11 to 0.16 kW/kWp and *nME* from -0.03 to 0.07 kW/kWp. The *CC*s range between 0.7 to 0.9. Each variation leads to an area showing only a small deviation from one another and similar shapes. The results of the Reindl model are in the range of *nRMSE* from 0.11 to 0.16 kW/kWp and *nME* from -0.03 to 0.07 kW/kWp. The *CC*s range between 0.70 to 0.9. However, the results calculated with the Perez model tend to reflect higher *nRMSE* values and an

increased absolute value of *nME*. The results of the Perez model are in the range of *nRMSE* from 0.11 to 0.16 kW/kWp and *nME* from -0.03 to 0.08 kW/kWp. The *CC*s range between 0.70 to 0.9.

Three PV cell temperature calculation models are taken into account in the variation analysis: the Faiman model, the Sandia model and the DGS model. The results of these variations are shown in Figure 5.7.

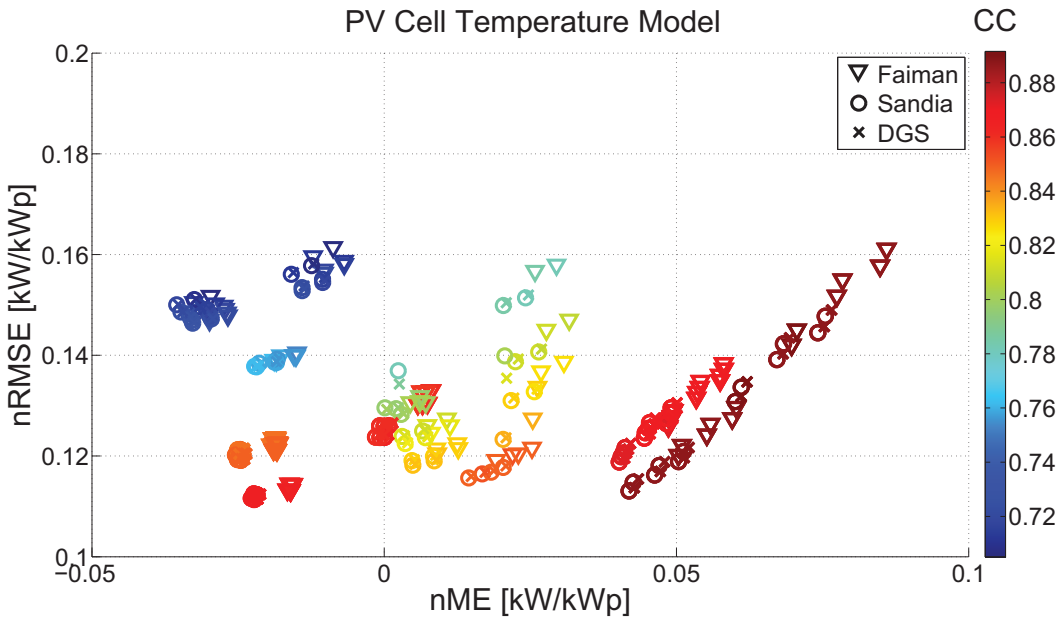


Figure 5.7: Variation of the PV cell temperature calculation model considering the Faiman (upside-down triangles), SAPM (circles) and DGS (diagonal crosses) model. The result points express the normalized *ME* (*nME*, x-coordinate) and normalized *RMSE* (*nRMSE*, y-coordinate) as well as the colour-coded *CC*. Blue colour represents a low *CC* and red colour a high *CC*.

The results using the Faiman model tend to reflect higher *nRMSE* and *nME* values and are in the range of *nRMSE* from 0.11 to 0.16 kW/kWp and *nME* from -0.03 to 0.08 kW/kWp. The *CC*s are in the range of 0.7 to 0.9. Both the Sandia model and the DGS model have only minor differences. Their results are in the range of *nRMSE* from 0.11 to 0.16 kW/kWp and *nME* from -0.04 to 0.08 kW/kWp. The *CC*s are also in the range of 0.7 to 0.9.

Finally, there are two inverter efficiency models used. The first model assumes a constant efficiency and the second model is the SGPI (see Section 2.4.3) The results are presented in Figure 5.8.

The SGPI model tends to result in lower *ME* and *RMSE* values than the constant-efficiency model. However, the deviations are small namely 0.003 kW/kWp for the *nME* and 0.002 kW/kWp for the *nRMSE*. Both have similar *CC*s in the range from

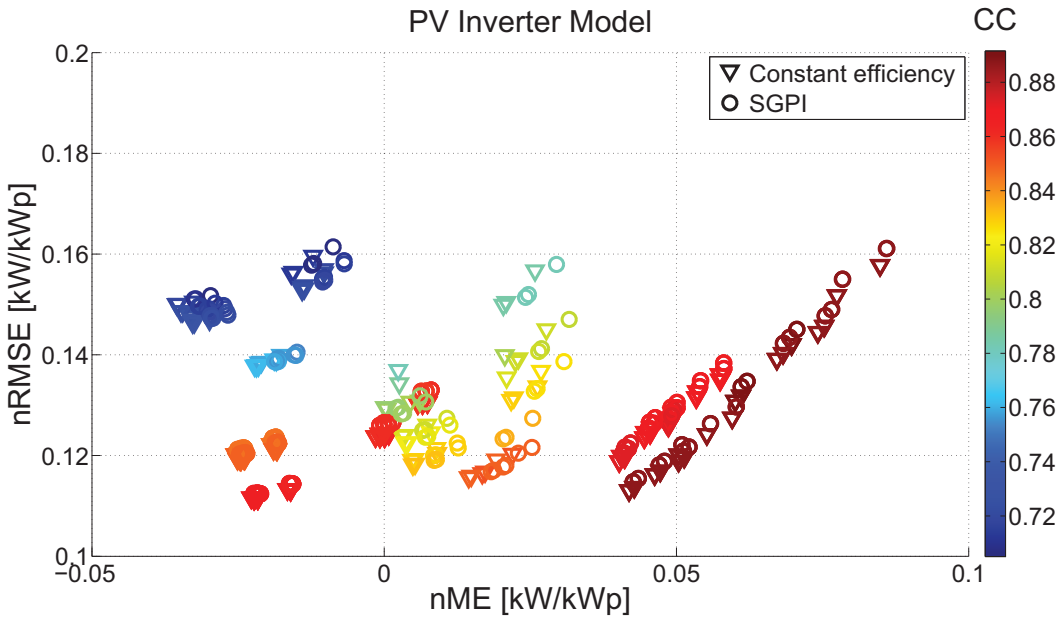


Figure 5.8: Variation of the PV inverter model considering a constant efficiency (upside-down triangles) and SGPI (circles) model. The result points express the normalized *ME* (*nME*, x-coordinate) and normalized *RMSE* (*nRMSE*, y-coordinate) as well as the colour-coded *CC*. Blue colour represents a low *CC* and red colour a high *CC*.

0.7 to 0.9.

## 5.2 Low voltage transformer load flow simulation

This section presents the results of the load flow calculation at the transformer. In addition to the results from the previous Section 5.1 different load profiles have been used.

### 5.2.1 Monthly statistics

The first analysis is based on monthly statistical measures and gives an indication of seasonal effects.

The monthly *rRMSE* values of the three satellite irradiance sources and the three load profiles are shown in Figure 5.9. As expected, there are only minor differences caused by the irradiance source. This is in line with *rRMSE* values of the ground-based irradiance measurements (see Section 3.1). However, the load profiles strongly affect the *rRMSE* of the transformer load flow. During the winter months all load profiles have similar *rRMSE* values. The *rRMSE* increases during

the summer months because of the higher variability of the load flow due to the PV feed-in power. Especially the VDI profile increases by 40 % compared to SLP and NoSLP.

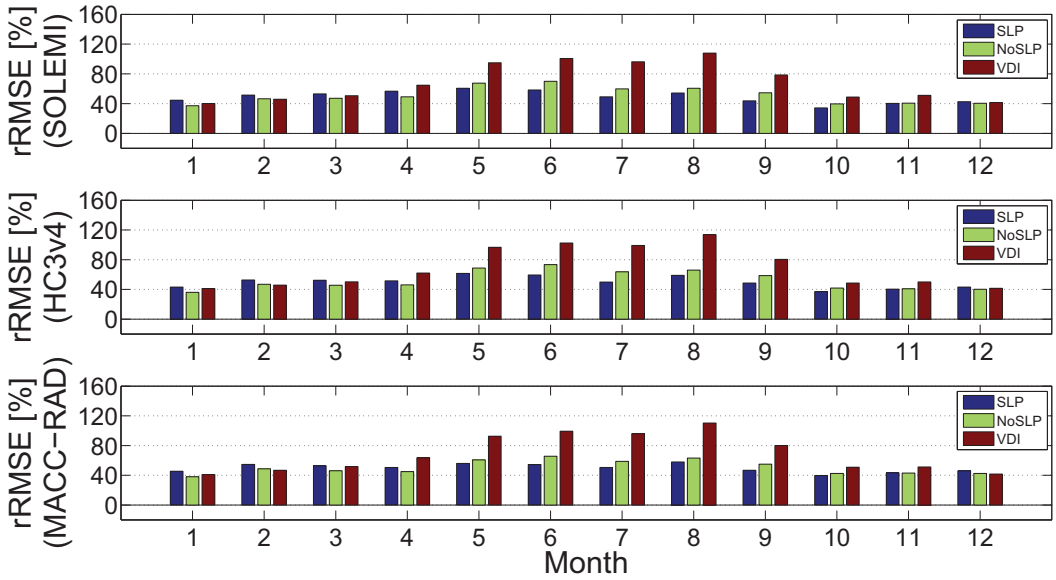


Figure 5.9: Monthly *rRMSE* values of the transformer load flow distinguishing between irradiance sources and considered load profiles. Each irradiance source has its own bar graph. The different load profiles are colour-coded. The results using SLP are blue, NoSLP are green and VDI reference profile are brown.

The seasonal or monthly effects have a strong impact on the monthly *rME* values, as shown in Figure 5.10. During the summer months the *rME* of MACC-RAD is equal to or lower than SOLEMI and HC3v4. During the winter months the lowest *rME* is given for SOLEMI. February shows a negative *rME*. The very low air temperature below 0°C causes this negative *rME*. The multi-annual monthly average of the air temperature in February is -0.1°C based on the measurement values of the years 1950 to 2013 (DWD, 2015). However, the average monthly air temperature in February 2012 was -4.2°C. This cold in February leads to a higher consumption than assumed by the load profiles. Therefore, a underestimation occurs. Based on the measurements in 2012 of the both temperature and load flow at the transformer, a *CC* of -0.57 is found at night. The lower the temperature at night the higher the load flow. The deviation between the single satellite sources using the same load profile are below 15 % for each month.

The effects of the applied load profiles on the differences in *rME* results are visible. During the winter months the *rME* of all load profiles ranges from 0 to 20 % with February as outlier. Both NoSLP and VDI tend to result in lower *rME* values than SLP. However, this changes during the summer months. During this

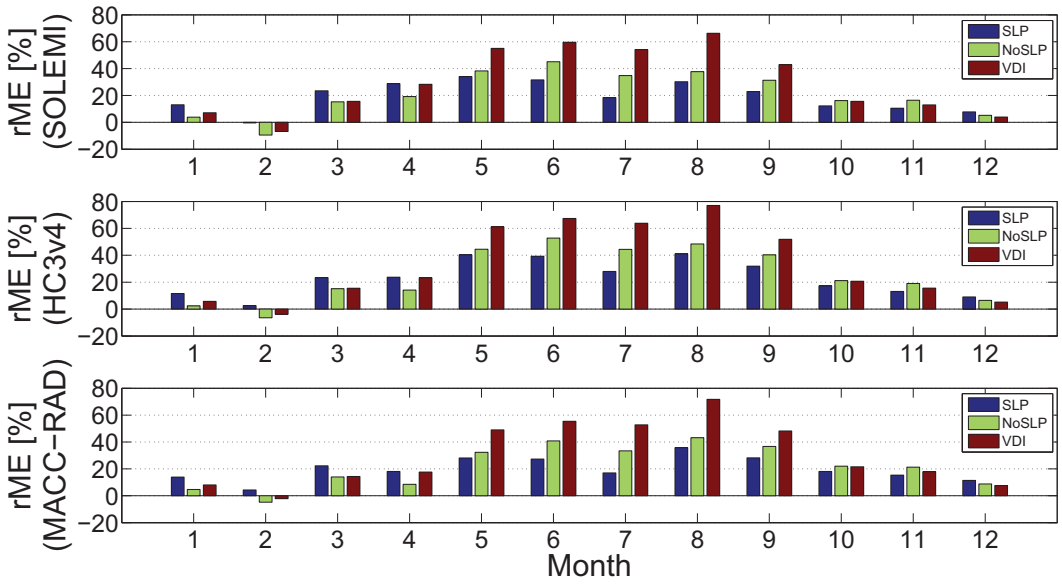


Figure 5.10: Monthly *rME* values of the transformer load flow distinguishing between irradiance source and considered load profile. Each irradiance source has its own bar graph.

time period all profiles result in higher *rME* values. This effect can be caused by the overestimation of the PV model as well as a reduced consumption due to vacation time. The calculations using SLP are in the range of 20 to 40 %. The calculations taking into account the NoSLP range from 30 to 50 % and the results using the VDI profiles are in the range of 40 to 75 %.

In terms of *CC*, there are minor differences between the three satellite-based irradiance sources except in February where *CC*s are between 0.3 and 0.6. This is shown in Figure 5.11. The reasons for the outlier in February are assumed to be the very low temperatures and the high demand which is not considered in the load profiles (see above). In this month the *CC* of MACC-RAD was 0.1 lower than SOLEMI. HC3v4 lies in the middle. During March to October the *CC*s are in a range of 0.7 to 0.9 for all irradiance measurement sources. In the other months the *CC*s range from 0.35 to 0.6.

The consideration of the load profiles shows only minor differences between SLP and NoSLP during the period from March to October. In the winter months the difference between both SLP and NoSLP increases to 0.1. The VDI shows lower *CC*s compared to the SLP and NoSLP during the summer months. The difference between VDI and the other two profiles is around 0.1. During the winter months it is in a similar range as SLP with an outlier in February where VDI is 0.2 points lower than SLP. However, the VDI profiles show the highest *CC* during the outlier

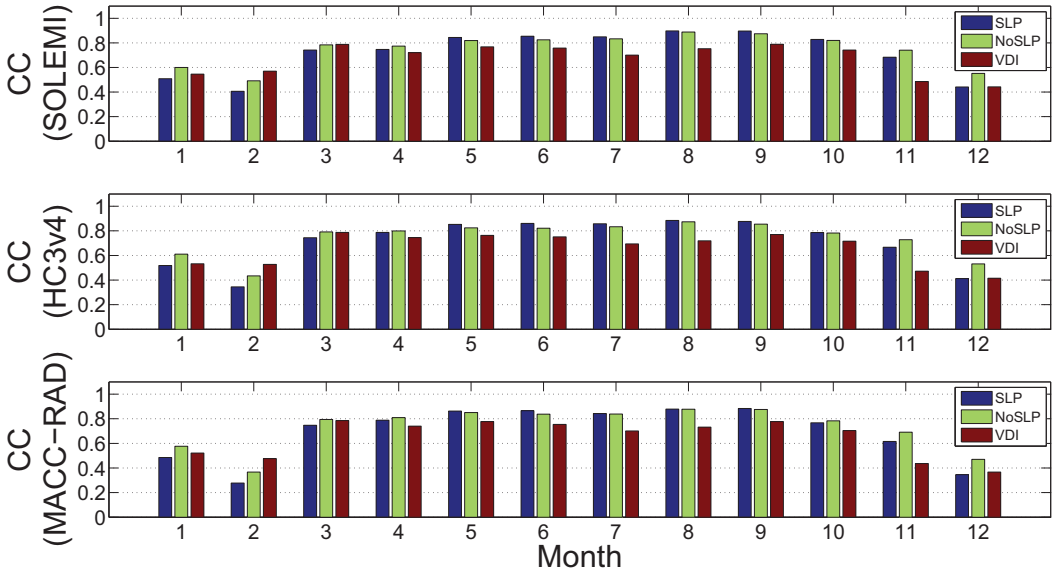


Figure 5.11: Monthly *CC* values of the transformer load flow distinguishing between irradiance source and considered load profile. Each irradiance source has its own bar graph.

month February.

### 5.2.2 Statistics of an annualized average day

The average day is calculated by averaging the same 15-minute interval of each day in the observation year. This is done for the simulation variations considering the different irradiance measurement sources and load profiles as well as for the measured load flow at the transformer. The results give an indicator of the diurnal effects on the calculation accuracy. The calculations and measurement time series of this average day are shown in Figure 5.12.

The maximum difference between each irradiance measurement source used is 10 kW and independent from the load profile. The interpolation of the hourly SOLEMI data to a 15-minute time resolution leads to oscillation effects during the time between sunrise and sunset. These small deviations correspond with the comparison results of the original irradiance measurement sources (Espinar *et al.*, 2014).

The differences in the time series depend on the applied load profiles. During the night SLP and NoSLP underestimate the load flow at the transformer while VDI overestimates. The amplitude of the morning peak is the same for both SLP and VDI however there is a time shift of one hour between both. This time shift can be caused by usage of uniform distribution to avoid a invalid high coincidence factor. The amplitude of the NoSLP is simultaneously 35 kW lower than SLP. During

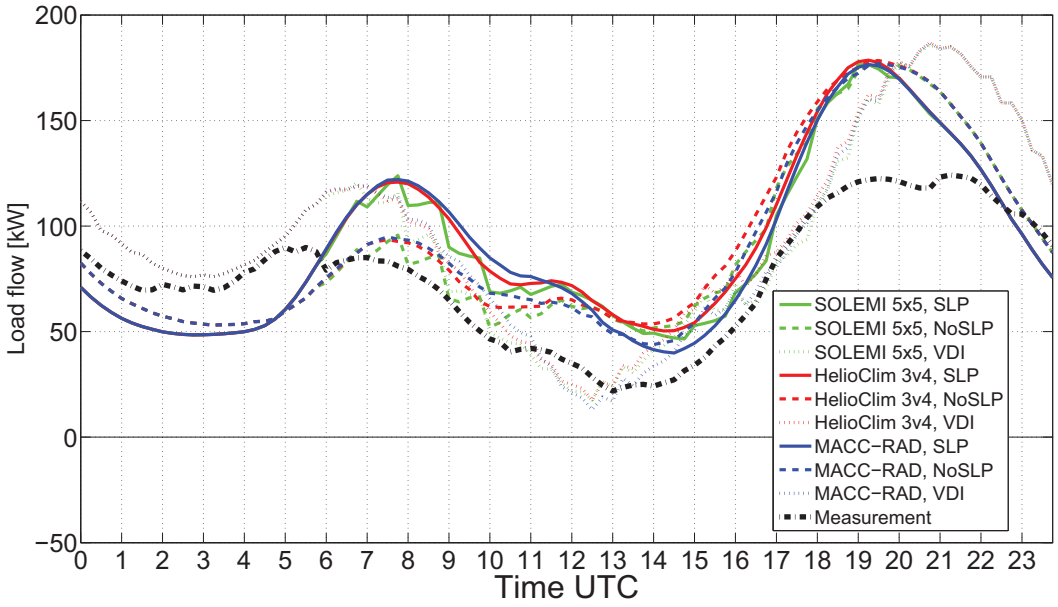


Figure 5.12: Comparison of calculated annualized averaged day load flow time series against the annualized averaged measurement. The irradiance measurement sources are distinguished by colours. The green lines shows the calculated load flows using the SOLEMI irradiance data, while HC3v4 is in red and MACC-RAD in blue. The applied load profiles are marked with the different line types. The calculated results taking into account the SLP are printed as solid lines, while calculations with NoSLP are dashed and calculations with VDI are dotted. The black dash-dotted line represents the measured average load flow at the transformer.

the day all profiles follow the diurnal cycle especially with the load flow reduction because of the PV feed-in power. The VDI profiles have the lowest deviation compared with the measurement. SLP and NoSLP have higher deviations and overestimate the load flow at the transformer. The amplitude of the evening peak is similar at each load profile. However, VDI is time-shifted by two hours and has a higher amplitude. The SLP and NoSLP show only a minor difference. All profiles overestimate the measured load profile by 60 to 70 kW.

For each 15-minute interval of the year, the statistical measures are calculated related to the measured 15-minute interval. These statistical measures are plotted over time in Figure 5.13.

As seen in the time series in Figure 5.12, the irradiance measurement sources do not cause large deviations. The oscillation effect of SOLEMI is also visible in the $ME$. MACC-RAD shows a tendency to lower $ME$ values during the afternoon hours. These $ME$ curves are the combination of the diurnal cycle of the PV feed-in power and the mismatch between the load profiles and the measurement. The $ME$ of SLP and NoSLP is below 0 kW during the night, that is, an underestimation of the load flow. The VDI profiles overestimate the night consumption. The SLP profile shows a higher $ME$ before noon than NoSLP and VDI. However, the NoSLP profile has a higher $ME$ during the afternoon than SLP and VDI. The VDI profile has two minima during noon time and before the evening peak where the load is underestimated. There is a time shift of approximately two hours between VDI and the other profiles because of the uniform distribution avoiding coincidence peaks in the time series (see above).

The standard deviation $STD$ also does not show a strong deviation caused by the irradiance measurement sources. The HC3v4 data has a lower $STD$ than the MACC-RAD data. The SOLEMI data has higher $STD$ before noon caused by the oscillation effects. The SLP and NoSLP show higher $STD$ during the day as a result of the diurnal cycle depending also on the irradiance data sources. The $STD$ of the VDI profile is higher than SLP and NoSLP. It has a maximum peak in the afternoon which is simultaneous with a local peak in the $ME$ between the two minima. The diurnal cycle seems be overlaid by the load profile variability.

There are minor deviations in the $RMSE$ curves because of the variation of the irradiance measurement sources. The $RMSE$ considering MACC-RAD is slightly higher in the morning than when considering SOLEMI and HC3v4. The SOLEMI $RMSE$ curve also shows the oscillation effect of the interpolation. In the afternoon the $RMSE$ of HC3v4 is higher than that of SOLEMI and MACC-RAD. The $RMSE$ of SLP and NoSLP increases during the morning hours and falls into a trough. This

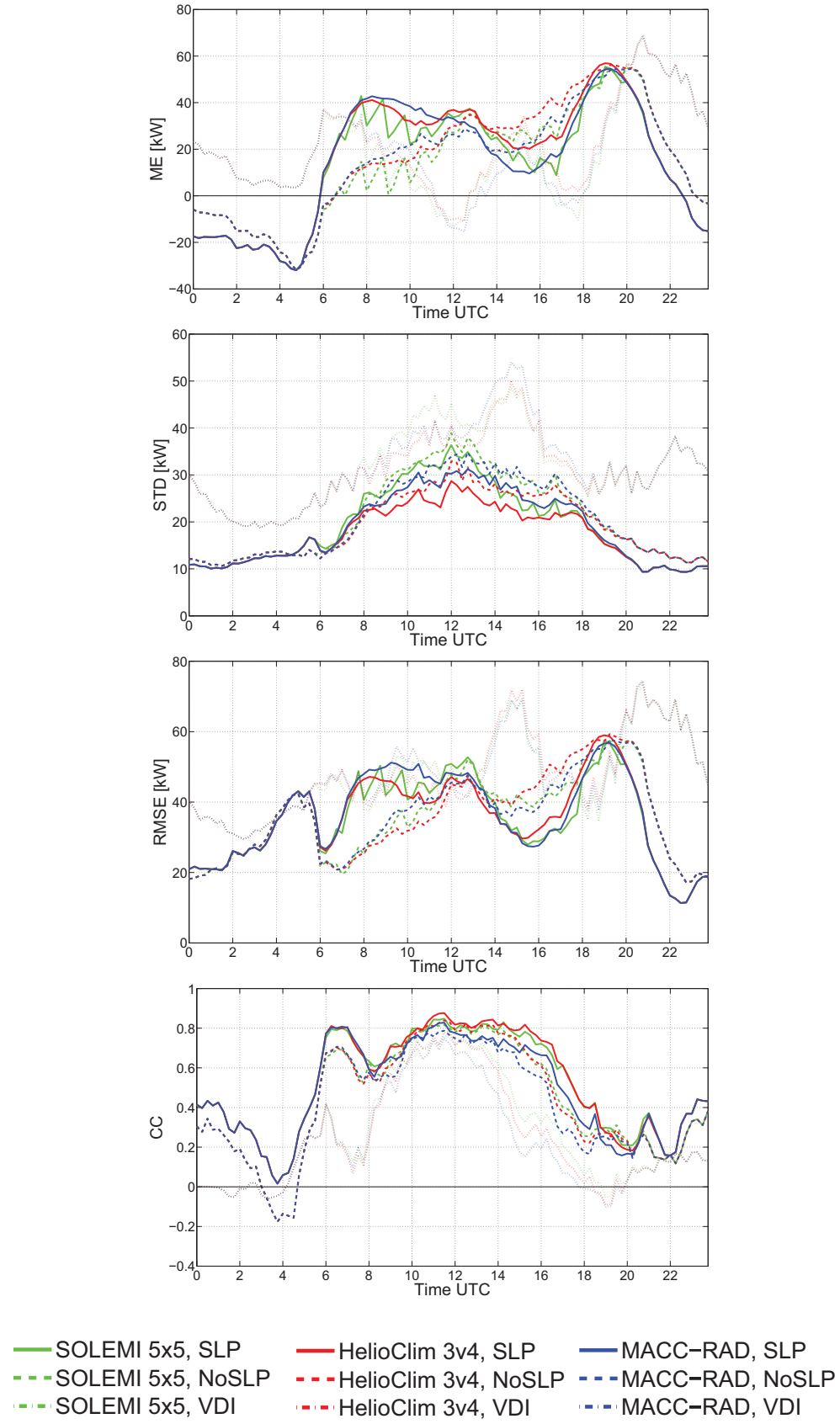


Figure 5.13: Statistical measures based on the comparison of calculated annualized average load flow time series against the annualized average measurement. The irradiance data sources are colour-coded (SOLEMI is green, HC3v4 is red, MACC-RAD is blue). The applied load profiles are marked with the different line types (SLP is solid, NoSLP is dashed, VDI is dotted).

trough is caused by the change of the *ME* from negative to positive while the *STD* is still low. Therefore, the VDI profile does not show such a trough. Before noon the SLP and VDI profiles have higher values of *RMSE* than NoSLP. Around noon all profiles shows a similar amplitude. In the afternoon the *RMSE* of the SLP drops to a local minimum while the *RMSE* of the NoSLP increases and the *RMSE* of the VDI shows a high peak. This peak is caused by the peak in *STD* due to the geometric relation of *ME* and *STD* to *RMSE*. All profiles have an additional peak in the evening. The *RMSE* of both SLP and NoSLP have the same amplitude and similar fall but the *RMSE* of VDI is shifted in time and has a higher amplitude. These *RMSE* curves are the combination of the diurnal cycle of the PV feed-in power and the mismatch between the load profiles and the measurement. The morning and evening peaks are not a result of the PV feed-in power because of its low impact related to assumed consumption by the load profiles at these times.

Basically, the *CC* also follows the diurnal cycle. During the day the *CC* is in a range of 0.6 to 0.8 and during the night in the range of -0.2 to 0.4 for both SLP and NoSLP. The effects of the different irradiance measurement sources lead to small effects during the day. In terms of *CC* the best performance has HC3v4 followed by SOLEMI and MACC-RAD. The VDI profile only has a high *CC* of at least 0.7 around noon. The rest of the time, the *CC* of the VDI profile ranges from -0.1 to 0.4.

### 5.2.3 Quarter-hourly value comparison

This section analyses the frequency distribution of the correlation between calculated and measured values as well as the occurrence of outliers. Therefore, several scatter plots are made to distinguish the effects during several periods of the day over the course of one year. For each combination of irradiance measurement source and load profile, a scatter plot taking into account all data pairs representing day and night. Furthermore, there are scatter plots showing only data pairs when the $\gamma_s$ is above $0^\circ$ and $15^\circ$ respectively, meaning only the effects during the day as well as scatter plots showing only data pairs when the $\gamma_s$ is below $0^\circ$ representing the night. For the SLP profile, there are also scatter plots distinguishing the morning and evening effects that are the periods where the $0^\circ \leq \gamma_s \leq 15^\circ$ and $15^\circ \geq \gamma_s \geq 0^\circ$, respectively.

The scatter plot of the comparison of simulated load flow values using the SLP and the measured load flow values is shown in Figure 5.14. The scatters of the whole day in the first row are similar for each irradiance source used. All running parallel to the main diagonal and have a positive bias. Furthermore, each have negative

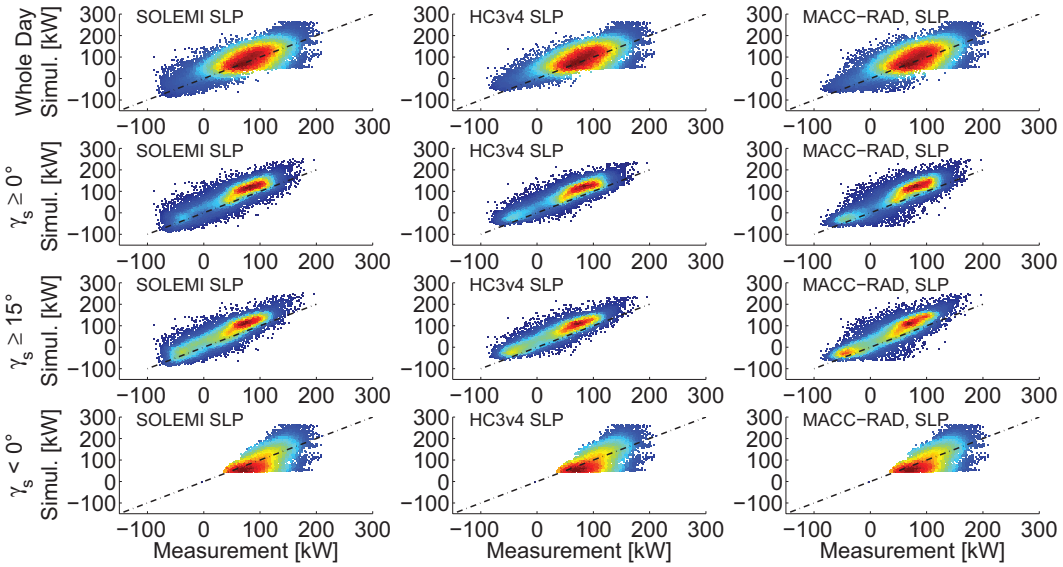


Figure 5.14: Comparison of calculated and measured load flow at the low voltage transformer. The calculation is based on the SLP profile. It is distinguished between the whole day (first row) and periods where $\gamma_s$ is above 0° and 15° (second and third row) respectively, and $\gamma_s$ is below 0° (fourth row) as well as the different irradiance sources. The frequency distribution is colour-coded. Red means frequent occurrence while blue stands for rare or single events. The main diagonal is shown as the chain dotted line and indicates a perfect correlation between calculation and measurement without error.

values indicating reversal load flows. There is noticeable edge in the scatter plots where the calculated load flow is constant at 50 kW and the measurement varies because of the mismatch between the SLP and the measurements during the night (see below).

The filtering of the data pairs to $\gamma_s$ above 0° and 15° respectively, reduces the variance. The frequency distribution shows a higher frequency running parallel to the main diagonal. This is visible as a greenish area close to the main diagonal and becomes clearer for $\gamma_s$ above 15°. The MACC-RAD data have a higher variance at low load flow values compared with both SOLEMI and HC3v4. This result corresponds to the comparison of the different satellite irradiance sources with the ground measurements in Section 3.1.

The periods with $\gamma_s$ below 0° show the variance of the SLP and the measurement at night. This result is not influenced by the PV feed-in power and shows the error of the load profile during the night. A horizontal edge is visible because of an assumed minimum load of 50 kW due to the load profiles while the measured consumption ranges from 50 to 187 kW. This assumption is caused by the low consumption of the SLP at night.

The scatter plot of the comparison of calculated load flow values using the NoSLP and the measured load flow values is shown in Figure 5.15. The plots of

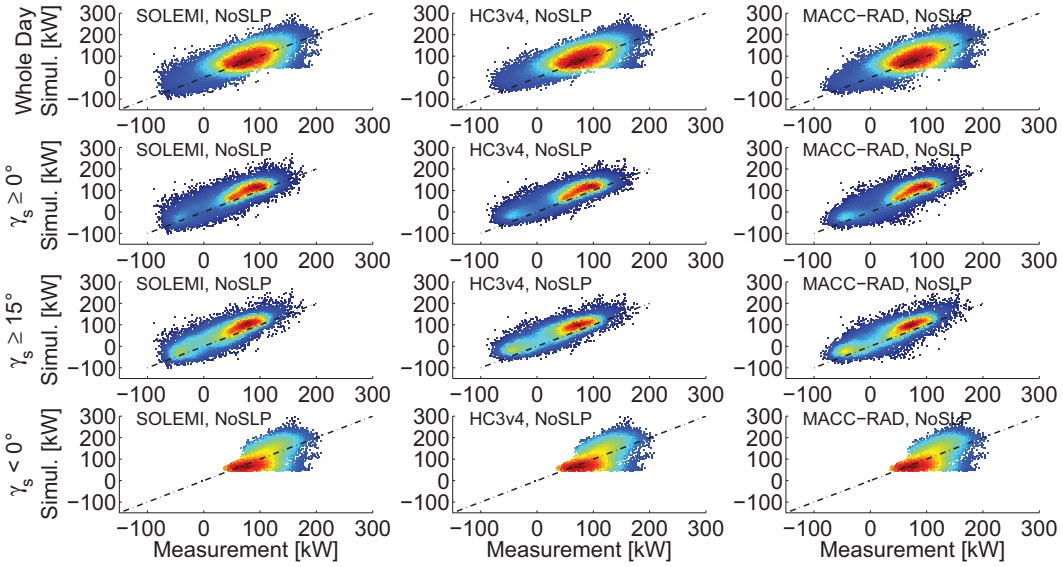


Figure 5.15: Comparison of calculated and measured load flow at the low voltage transformer. The calculation is based on the NoSLP profile. It distinguishes between the whole day (first row), periods with $\gamma_s$ above 0° and 15° (second and third row) respectively, and periods with $\gamma_s$ below 0° (fourth row) as well as the different irradiance sources. The frequency distribution is colour-coded. Red means frequent occurrence while blue stands for rare or single events. The main diagonal is shown as the chain dotted line and indicates a perfect correlation between calculation and measurement without error.

the NoSLP calculations considering all data as well as limited to $\gamma_s$ above 0° and 15° respectively, are very similar to those of the SLP calculations. All running parallel to the main diagonal, also show a positive bias and have negative values indicating reversal load flows. As in the SLP calculations, there is a noticeable edge in the scatter plots where the calculated load flow is constant at 50 kW and the measurement varies. The reason again is the variance at night. The NoSLP data have some higher outliers in the load compared with the SLP data.

Similar to the SLP results, filtering the data by $\gamma_s$ above 0° and 15° respectively, reduces the variance. The frequency distribution shows a higher frequency running parallel to the main diagonal. This is visible as a greenish area close to the main diagonal and becomes clearer for $\gamma_s$ above 15°. As with the SLP, the MACC-RAD data show a higher variance at low load flow values compared with both SOLEMI and HC3v4.

Also during the night hours the results of NoSLP are very similar to SLP. The periods with $\gamma_s$ below 0° show the variance of the SLP and the measurement at

night. Some higher outliers occur here compared with the SLP data. This result is not influenced by the PV feed-in power and shows the error of the load profile during the night. Similar to SLP, a horizontal edge is also visible for the NoSLP data because of the minimum load of 50 kW while the measured consumption ranges from 50 to 187 kW.

The scatter plot of the comparison of calculated load flow values using the VDI and the measured load flow values is shown in Figure 5.16. Generally, the scat-

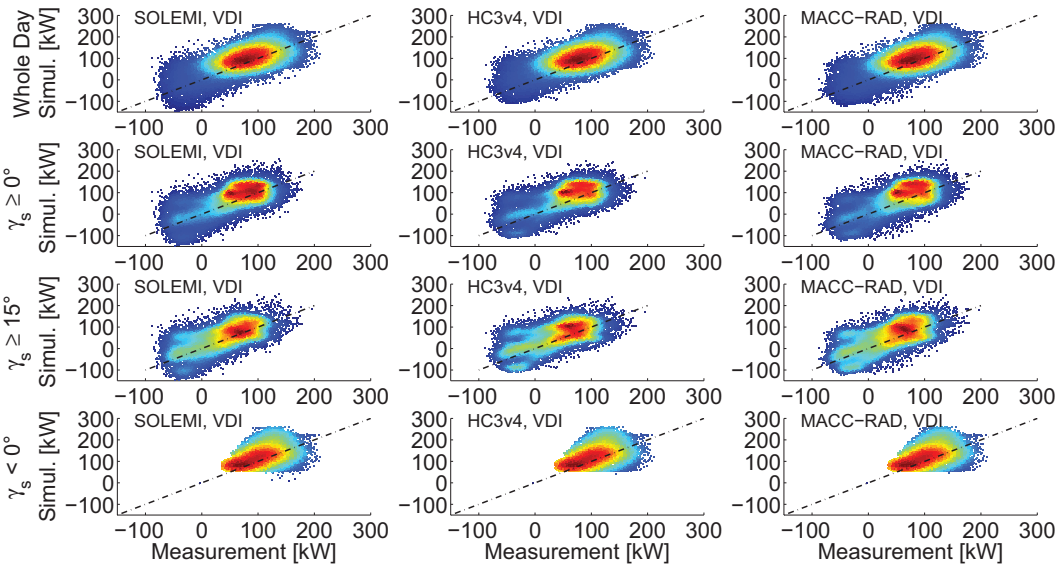


Figure 5.16: Comparison of calculated and measured load flow at the low voltage transformer. The calculation is based on the VDI profile. It distinguishes between the whole day (first row), periods with $\gamma_s$ above 0° and 15° (second and third row) respectively, and periods with $\gamma_s$ below 0° (fourth row) as well as the different irradiance sources. The frequency distribution is colour-coded. Red means frequent occurrence while blue stands for rare or single events. The main diagonal is shown as the chain dotted line and indicates a perfect correlation between calculation and measurement without error.

ter plots of the calculations based on the VDI profile considering all data as well as limited to $\gamma_s$ above 0° and 15° respectively, are similar to those of the SLP and NoSLP calculations. All running parallel to the main diagonal and have a positive bias. Furthermore, each have negative values indicating reversal load flows. However, the variability is higher compared to SLP and NoSLP and the edge indicating the mismatch during nighttime is almost overlaid by the scattering. The VDI profile shows the highest outlier also occurring during the night.

The filtering of the data pairs to $\gamma_s$ above 0° and 15° respectively, slightly reduces the variance. The frequency distribution shows a higher frequency following the main diagonal but with a higher variance. Especially during the low load and

reversal load situations the variance of the frequency distribution is increased. Both HC3v4 and MACC-RAD show a higher frequency of overestimation of the reversal load flows. The higher variance of MACC-RAD is not visible due to the load variance.

The periods with $\gamma_s$ below 0° show the variance of the VDI profile applied compared with the SLP and NoSLP. The frequency distribution is high over a wider range up to 150 kW compared to SLP and NoSLP.

The estimation of the reasons for the errors at morning and evening is only based on the SLP. Figure 5.17 shows the period between $\gamma_s$ above 0° and $\gamma_s$ below 15° divided into sunrise $(0° \leq \gamma_s \leq 15°)$ and sunset $(15° \geq \gamma_s \geq 0°)$.

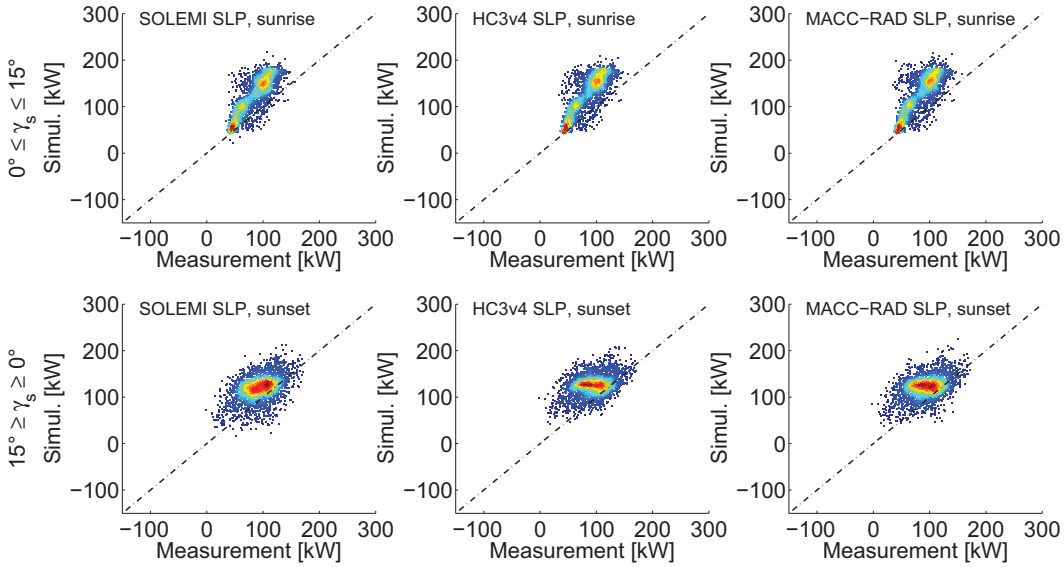


Figure 5.17: Comparison of calculated and measured load flow at the low voltage transformer. The calculation is based on the SLP profile. It differentiates between sunrise $(0° \leq \gamma_s \leq 15°)$ and sunset $(15° \geq \gamma_s \geq 0°)$. The comparison during the sunrise is shown in the first row and during the sunset in the last row, respectively.

During the period in which the sun is rising from 0° to 15°, a higher frequency of overestimation in the range of 40 kW to 180 kW is visible in green and red colours. The measurements range from 40 kW to 120 kW. However, the average calculated PV feed-in power is 6.4 kW for SOLEMI, 3.1 kW for HC3v4 and 2.6 kW for MACC-RAD during this period. The assumed averaged power of the SLP is 126.5 kW for the period of $0° \leq \gamma_s \leq 15°$. Therefore, the influence of the PV during the sunrise period can be neglected because of the strong influence of the load profile. The variance is very similar for each satellite irradiance source.

During the period in which the sun is setting from 15° to 0°, a high frequency of overestimation at 125 kW is visible in red colour. The measurements range

from 65 kW to 120 kW. The average calculated PV feed-in power is 30.2 kW for SOLEMI, 23.6 kW for HC3v4 and 26.9 kW for MACC-RAD. This is only 10 % to 13 % of the installed $P_{STC}$. The assumed averaged power of the SLP is 148.5 kW for the period of $15° \geq \gamma_s \geq 0°$. For the test site, the PV affects the load flow calculation at sunset more than at sunrise due to the PV system orientation. However, the load profile effect is 5 times as strong. Therefore, it can be assumed that the errors during sunset are a result of the load profile mismatch. The result using the SOLEMI-derived irradiance has a higher variance in the calculation compared to HC3v4 and MACC-RAD. The variance in the calculation of HC3v4 is the lowest.

### 5.2.4 Energy balance comparison

The period from $7^{th}$ August 2014 to $9^{th}$ October 2014 is used for the calculation of the energy values at the test site. Unfortunately, only within this period all in-situ measurements are available, namely the *GHI* at the test site, PV feed-in power from the smart meters of the PV systems and the transformer load flow. The MACC-RAD irradiance represents the satellite-derived irradiance. Note, that these results are only valid for two months and are not comparable to the annual results because of missing seasonal effects. The results of the comparison are shown in Table 5.3. The in-situ measurements at the test site are taken as reference and the relative error of measurement (*rEM*) is calculated. The *rEM* is defined as the difference between a measured value and a corresponding reference value (see equation 9.10 in Section 9.1).

The pyranometer of the weather station at the transformer measures irradiation of 200.3 kWh/m$^2$ during the 63 days of investigation and this value is used as reference. The pyranometer of the weather station at the university campus measures 210.5 kWh/m$^2$. This can be seen as an *rEM* of 5 % related to the irradiation measured at the test site. The MACC-RAD irradiation measured at the location of the test site is 238.5 kWh/m$^2$ equal to an *rEM* of 19 %.

The smart meter energy measurements of the 12 PV feed-in meters is 26.1 MWh for the investigation time. The calculated PV feed-in energy considering the irradiance data from the pyranometer at the test site is 26.8 MWh. This is an *rEM* of 3 % related to smart meter measurements. If the irradiance of the pyranometer at the university location is taken into account, the calculated PV feed-in energy is 28.2 MWh and is an *rEM* of 8 %. The calculated PV feed-in energy with the irradiance from MACC-RAD is 31.8 MWh. This represents an *rEM* of 22 %.

As described in the variation analysis (see Section 4.2.3), the orientation angle sources are also changed. The energy of the investigation period is calculated with

Table 5.3: Energy balance comparing calculated and measured energy in the test site during the period from $7^{th}$ August 2014 to $9^{th}$ October 2014.

| ***Parameter*** | ***Irradiance Source*** | ***Calculated Energy*** | ***Measured Energy*** | ***rEM*** |
|---|---|---|---|---|
| Irradiation $[kWh/m^2]$ | MACC-RAD | 238.5 | 200.3 | 19 % |
| | Pyranometer HSU | 210.4 | | 5 % |
| | Pyranometer test site | n/a | | n/a |
| PV feed-in energy $[MWh]$ | MACC-RAD | 31.8 | 26.1 | 22 % |
| | Pyranometer HSU | 28.2 | | 8 % |
| | Pyranometer test site | 26.8 | | 3 % |
| | MACC-RAD, in-situ orientation | 32.4 | | 24 % |
| | MACC-RAD, assumed optimal orientation | 34.6 | | 33 % |
| | MACC-RAD, at 25°C and no wind | 30.2 | | 16 % |
| | Pyranometer HSU, at 25°C and no wind | 26.7 | | 2 % |
| | Pyranometer test site, at 25°C and no wind | 25.5 | | -2 % |
| Energy at Transformer $[MWh]$ | MACC-RAD | 136.4 | 95.4 | 43 % |
| | Pyranometer HSU | 129.7 | | 36 % |
| | Pyranometer test site | 129.5 | | 36 % |

the in-situ measurement of tilt and azimuth angle and an assumed optimal orientation of the PV systems. This avoids an additional source of error from the LiDAR data. The calculation with the combination of MACC-RAD and the in-situ orientation data results in a PV feed-in energy of 32.4 MWh. This represents an *rEM* of 24 % related to smart meter measurements. Assuming an optimal orientation the calculated PV feed-in energy increases to 34.6 MWh equal to an *rEM* of 33 %.

The PV model considers the air temperature and wind speed as influencing parameters on the PV module efficiency. To analyse the impact of these meteorological parameters on the energy balance, additional calculations are performed with an air temperature of constant 25 °C and wind speed of 0.0 m/s. Under these conditions, the calculation considering the irradiance from the pyranometer at the test site results in a PV feed-in energy of 25.6 MWh. This represents an *rEM* of -2 % related to smart meter measurements. If the calculation is done with the irradiance data from the pyranometer at the university campus the PV feed-in energy is 26.7 MWh equal to an *rEM* of 2 %. The calculation using MACC-RAD irradiance with described ambient conditions leads to a PV feed-in energy of 30.2 MWh. This is an *rEM* of 16 %.

Furthermore, the energy transferred over the transformer is calculated with the proposed model considering the SLP. The measurement device at the transformer provides the reference measurements. The energy at the transformer station is 95.4 MWh during the investigation period. The calculation of the energy considering the irradiance data from the pyranometer at the test site results in an energy at the transformer station of 129.5 MWh. This represents an *rEM* of 36 %. The energy at the transformer station is 129.7 MWh if the irradiance from the pyranometer at the university is used for the calculation. This also represents an *rEM* of 36 % related to measurement at the transformer. The usage of the satellite irradiance data by MACC-RAD results in a energy at the transformer station of 136.4 MWh (*rEM* of 43 %).

The deviation from the measured values at the test site depends on the source of the irradiation measurement. As expected, MACC-RAD shows the highest *rEM* for irradiation followed by the pyranometer measurement at the university campus. The uncertainty of the pyranometer at the test site is not considered but is around $\pm 2$ %. The PV model to calculate the PV feed-in power presented here increases the *rEM* by 3 % and is independent from the irradiation measurement source. If the ambient temperature is assumed at constant 25°C and no wind, the *rEM* decreases by 5-6 %. The assumed optimal orientation of the PV systems increase the *rEM* by 2 %. The *rEM* of the transformer load flow calculation is strongly affected by the

load profile. It increases from 22 % to 43 % for MACC-RAD and from 8 % to 36 % for the pyranometer data.

### 5.2.5 Reversal load flow occurrence detection

The knowledge of the occurrence of reversal load flows is important for the grid operation. The reversal load flow occurs if the decentralized generators e.g. PV systems feed-in more power than consumed within the grid area. In these situations the voltage increases in both the low voltage level and the medium voltage level as well as the violation of technical restrictions regulation can occur depending on the ratio of PV feed-in power and consumption. Especially rural grids can have a high value of installed PV power and a coincident low consumption power resulting in high PV feed-in power values (Mohrmann *et al.*, 2012).

The detection of reversal load flows can be performed with the proposed method and the results are expressed as scores (see Section 4.2.2). The three different irradiance sources and the three different load profiles are taken into consideration. Furthermore, the results distinguish between the whole day and periods with $\gamma_s \geq 0°$ and $\gamma_s \geq 15°$ respectively.

The scores for the consideration of the whole day over one year are shown in Table 5.4.

Table 5.4: Scores for the detection of reversal load flow occurrence at the low voltage transformer considering data of the whole day.

| ***Irradiance, whole day*** | ***Load profile*** | ***PC*** | ***THS*** | ***FAR*** | ***CTB*** | ***POD*** | ***POFD*** |
|---|---|---|---|---|---|---|---|
| SOLEMI | SLP | 0.95 | 0.95 | 0.04 | 1.03 | 0.99 | 0.36 |
| | NoSLP | 0.94 | 0.94 | 0.05 | 1.03 | 0.99 | 0.41 |
| | VDI | 0.93 | 0.93 | 0.05 | 1.02 | 0.97 | 0.43 |
| HC3v4 | SLP | 0.95 | 0.95 | 0.05 | 1.05 | 0.99 | 0.44 |
| | NoSLP | 0.94 | 0.94 | 0.05 | 1.05 | 0.99 | 0.48 |
| | VDI | 0.93 | 0.93 | 0.05 | 1.03 | 0.98 | 0.48 |
| MACC-RAD | SLP | 0.95 | 0.95 | 0.04 | 1.02 | 0.98 | 0.32 |
| | NoSLP | 0.95 | 0.94 | 0.04 | 1.03 | 0.98 | 0.37 |
| | VDI | 0.93 | 0.93 | 0.05 | 1.02 | 0.97 | 0.42 |

As can be seen, the calculations using the SLP result in the highest values of *PC* and $THS$ as well as the lowest *FAR* compared to NoSLP and VDI. The consideration of SLP results in a better detection of reversal load flows at the transformer than NoSLP and VDI. The lowest *PC* and $THS$ values and the highest *FAR* are determined for calculations considering VDI. The results of NoSLP range between SLP

and VDI. The $CTB$ is larger than one for all load profiles meaning the detection of reversal load flows is overestimated. The probability of detection $POD$ ranges from 0.97 to 0.99 for all load profiles with the same order namely SLP with the highest value of $POD$, followed by NoSLP and VDI with the lowest value. The variability of the $POFD$ is larger than in the other scores. The $POFD$ ranges from 0.32 for SLP with irradiance data from MACC to 0.48 for NoSLP and VDI with irradiance data from HC3v4. The $POFD$ is lowest with SLP and highest with VDI taking into account the same irradiance source.

However, in the calculation of the whole day scores the differences between the load profiles used are small because of the consideration of the night. Naturally, during the night no reversal load flows caused by PV can occur and lead to high scores in detecting normal load flows. The satellite irradiance sources only slightly affect the scores of the whole day calculations. The appreciable dependencies on the irradiance are given for $CTB$ and $POFD$. The calculation using HC3v4 irradiance data shows an increased $CTB$ and $POFD$. For SOLEMI and MACC the $CTB$ is similar. MACC has the lowest $POFD$ followed by SOLEMI.

The scores for the detection of reversal load flow occurrence at the low voltage transformer considering only data when $\gamma_s \geq 0^\circ$ are shown in Table 5.5.

Table 5.5: Scores for the detection of reversal load flow occurrence at the low voltage transformer considering data of $\gamma_s \geq 0^\circ$.

| ***Irradiance,*** $\gamma_s \geq 0^\circ$ | ***Load profile*** | ***PC*** | ***THS*** | ***FAR*** | ***CTB*** | ***POD*** | ***POFD*** |
|---|---|---|---|---|---|---|---|
| SOLEMI | SLP | 0.9 | 0.89 | 0.09 | 1.07 | 0.97 | 0.37 |
| | NoSLP | 0.89 | 0.88 | 0.1 | 1.07 | 0.97 | 0.42 |
| | VDI | 0.86 | 0.84 | 0.11 | 1.05 | 0.94 | 0.44 |
| HC3v4 | SLP | 0.9 | 0.89 | 0.1 | 1.1 | 0.99 | 0.45 |
| | NoSLP | 0.89 | 0.87 | 0.11 | 1.1 | 0.98 | 0.49 |
| | VDI | 0.86 | 0.85 | 0.11 | 1.07 | 0.95 | 0.49 |
| MACC-RAD | SLP | 0.91 | 0.89 | 0.08 | 1.05 | 0.97 | 0.32 |
| | NoSLP | 0.89 | 0.88 | 0.09 | 1.06 | 0.96 | 0.38 |
| | VDI | 0.86 | 0.84 | 0.1 | 1.04 | 0.93 | 0.43 |

The best values for $PC$, $THS$ and $FAR$ show the calculation considering SLP followed by NoSLP and VDI with the worst scores. All calculations result in $CTB \geq 1.0$, that is, an overestimation of the event detection. The highest values of $CTB$ are given for the NoSLP. The $POD$ is still high in a range from 0.93 to 0.99. The low values of $POD$ are from VDI while the high values are from SLP. The difference between SLP and NoSLP are small. In the case of $POFD$ the SLP shows the lowest and therefore the best values with a range from 0.32 to 0.42 depending

on the irradiance source. The lowest results occur using VDI ranging from 0.43 to 0.49 also depending on the irradiance source.

The differences in *PC* and $THS$ as a result of the different irradiance data sources are negligible. The *FAR* is slightly higher for the calculations using HC3v4 data compared to SOLEMI and MACC. This increase is also visible in $CTB$ where the HC3v4 calculations are around 0.04 higher. The differences in *POD* between the irradiance data sources used are small with slightly higher results of HC3v4. The lowest values of $POFD$ show MACC ranging from 0.32 to 0.43 followed by SOLEMI and HC3v4 with the highest values ranging from 0.45 to 0.49.

The scores of the reversal load flow occurrence detection considering the data when $\gamma_s \geq 15°$ are shown in Table 5.6. The absolute values of the scores differs to these in table 5.5 considering data where $\gamma_s \geq 0°$. However, the tendencies are the same.

Table 5.6: Scores for the detection of reversal load flow occurrence at the low voltage transformer considering data of $\gamma_s \geq 15°$.

| ***Irradiance,*** $\gamma_s \geq 15°$ | ***Load profile*** | ***PC*** | ***THS*** | ***FAR*** | ***CTB*** | ***POD*** | ***POFD*** |
|---|---|---|---|---|---|---|---|
| SOLEMI | SLP | 0.86 | 0.84 | 0.13 | 1.11 | 0.96 | 0.37 |
| | NoSLP | 0.85 | 0.81 | 0.15 | 1.12 | 0.95 | 0.42 |
| | VDI | 0.8 | 0.77 | 0.16 | 1.07 | 0.9 | 0.44 |
| HC3v4 | SLP | 0.86 | 0.83 | 0.16 | 1.16 | 0.98 | 0.45 |
| | NoSLP | 0.84 | 0.81 | 0.17 | 1.16 | 0.97 | 0.49 |
| | VDI | 0.8 | 0.77 | 0.17 | 1.11 | 0.92 | 0.49 |
| MACC-RAD | SLP | 0.87 | 0.84 | 0.12 | 1.07 | 0.94 | 0.32 |
| | NoSLP | 0.85 | 0.82 | 0.14 | 1.1 | 0.94 | 0.38 |
| | VDI | 0.8 | 0.76 | 0.16 | 1.07 | 0.89 | 0.43 |

The best values of *PC*, $THS$ and *FAR* occur using the SLP calculations. The calculations using VDI result in the worst scores. The highest values of $CTB$ occur in the NoSLP calculations, followed by SLP with a high variance depending on the irradiance source and VDI with the lowest overestimation. The *POD* is high for SLP and NoSLP calculations and decreases for VDI like scores considering both the whole day and $\gamma_s \geq 0°$. The $POFD$ of the SLP calculations are in the range of 0.32 to 0.45, followed by those of NoSLP ranging from 0.38 to 0.49. The calculations using VDI profile have the highest $POFD$ avalues and the lowest variance ranging from 0.43 to 0.49.

The different irradiance sources affect the scores in a similar way as in the case taking into account all daylight hours. There are small deviations in *PC* and $THS$. The *FAR* is almost equal for the SOLEMI and MACC calculations and slightly in-

creased for the HC3v4 calculations. The HC3v4 also leads to higher values of $CTB$ compared with SOLEMI and MACC. The highest values of $POD$ are for HC3v4 while MACC has the lowest $POD$ values. The calculations using HC3v4 irradiance data have the highest $POFD$ values and MACC the lowest again.

It can be concluded that the $PC$ and $THS$ decreases from the calculations considering data from the whole day to those where $\gamma_s \geq 15°$. Vice versa, the $FAR$ and $CTB$ increase depending on the calculation period. This is caused by a statistical effect because of the score definition. At night no PV-driven reversal load flows can occur and increase the value of the denominator of the scores. This leads to better results in the score calculation. The $POD$ describes only the ratio of occurred events related to both detected and missed events. Therefore, it is independent of the diurnal cycle and almost constant. The same reason also applies for the $POFD$.

## 5.3 Medium voltage transformer load flow simulation

For each medium-to-low voltage transformer, the time-series of $P_{Trafo}$ is calculated using the irradiance provided by MACC-RAD. The load is assumed by the SLP based on the measured annual consumption. At this voltage level the load of the 1350 consumers can be described with the SLP (Fünfgeld and Tiedemann, 2000; Engels, 2000). Therefore, only SLP is considered and not NoSLP and VDI.

### 5.3.1 Annualized average day at medium voltage level

Similar to the analysis in Section 5.2.2, each instant time of the calculated and measured data in the investigation period is averaged and results in an average day profile. The resulting profiles of the averaging are shown in Figure 5.18.

Comparing the calculated results with the measurement, an underestimation of at least 100 kW during the night is visible. This is similar to the results at the low voltage level (see Section 5.2.2). The increase in the morning hours differs for both calculated load flow considering orientation data based on LiDAR and calculated load flow assuming optimal orientation. The calculated load flow considering orientation data based on LiDAR has a lower peak in the morning hours. Furthermore, the load flow using LiDAR increases to the evening peak sooner than the calculated load flow assuming an optimal orientation of the PV systems. The reason for this difference is a higher amount of the PV feed-in power during the morning hours because of a higher ratio of east-oriented PV systems than in assumed optimal ori-

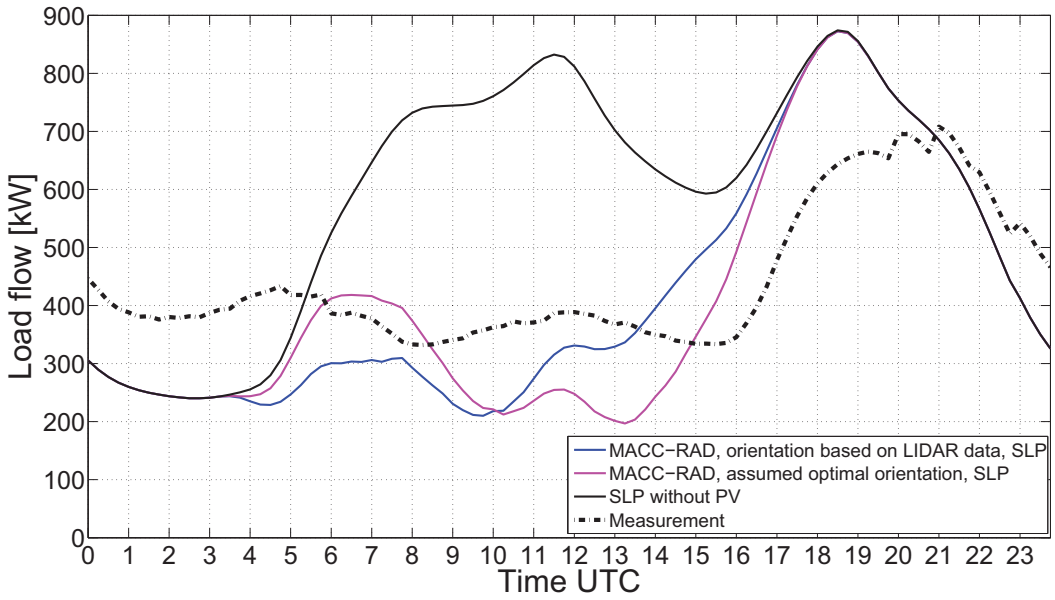


Figure 5.18: The annualized average of the measurement at the substation is plotted as a black dash-dotted line. The calculated absolute value considering the PV system orientation based on LiDAR data is shown as a blue solid line. The magenta solid line assumes an optimal orientation of the PV systems. The averaged SLP without an influence from PV is shown as a black solid line.

entation. During the day the calculation underestimates the load flow because of an overestimation of the PV feed-in power. Furthermore, the evening peak is overestimated in the calculations and time shifted by around two hours. These effects are similar to the results at the low voltage grid level. It is notable that the measured profile does not show an increase to a peak in consumption at noon because of the PV feed-in power even during low irradiance situation. The only peak is in the evening hours from approximately 16:30 UTC.

The statistical measures of the average day are shown in Figure 5.19. The *ME* is negative during the night because of the underestimation. The calculated load flows also show a negative *ME* while the SLP not considering the PV shows a high positive *ME*, as expected. Both calculated load profiles taking into account the PV feed-in power show a difference depending on the considered PV orientation angles. All profiles have a common positive *ME* during the evening peak from approximately 15:00 UTC to 20:00 UTC because of the low influence of the PV systems.

The *STD* of all profiles is around 100 kW during the night. The *STD* of the SLP shows a slight increase following the diurnal cycle. The *STD* of the calculated load flows are high during the day. This is caused by the high variation in the PV feed-in

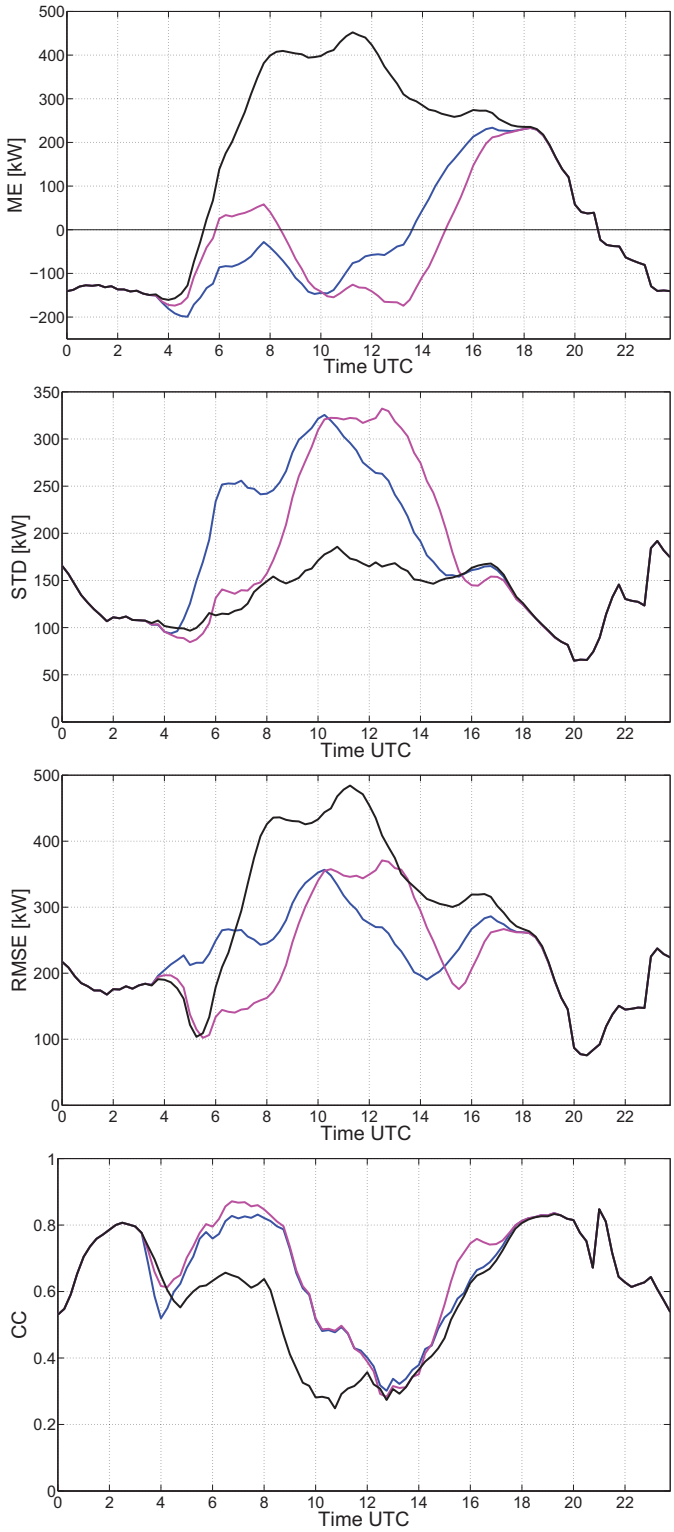


Figure 5.19: Statistical measures of the annualized averaged day at the medium voltage level of calculated load flow considering the orientation based on LiDAR data (blue solid line), assuming optimal orientation of the PV systems (red solid line) and the SLP (black solid line).

power because of the solar irradiance variation. Both $STD$ curves are shifted in time because of the different azimuth angles of the PV systems. The $STD$ curve using the LiDAR orientation values shows a diurnal variation from 5:00 UTC to 14:00 UTC while the $STD$ curve assuming an optimal orientation has a peak from 8:00 UTC to 15:00 UTC. All $STD$ curves have a common minima at around 20:00 UTC because of the similarity of the calculated and measured load profile at the evening peak during this time.

The $RMSE$ is around 180 kW at night for all calculations. Between 5:00 and 6:00 UTC there is a minimum for both SLP-only and the calculation assuming an optimal orientation because of a low $ME$ at the zero-crossing and a constant $STD$. The $RMSE$ of the calculation considering the LiDAR-based orientations does not show this minima. The reason for that is the missing zero-crossing and the steep increase of the $STD$ at this time. The $RMSE$ of this calculation increases to a maximum at 10:00 UTC. The $RMSE$ of the calculation assuming an optimal orientation shows a steep rise from 9:00 UTC to 10:00 UTC and a maximum at 13:00 UTC. The $RMSE$ of the SLP has the highest amplitude in this comparison of at least 400 kW and increases from 5:00 UTC to 8:00 UTC because of the high $ME$ as result of neglecting the PV influence. Both the $RMSE$ of the calculation considering the LiDAR-based orientations and assuming an optimal orientation have local minimas in the afternoon because of the low $ME$ during zero-crossing. All $RMSE$s decrease in the afternoon and run together at around 18:00 UTC when the influence of the PV no longer persists. All $RMSE$ curves have a common minima at around 20:00 UTC because of the second zero-crossing of the $ME$ and the low $STD$.

The $CC$s of all calculations are in a range from 0.6 to 0.8 during the nighttime. This is around twice as high as the $CC$s for the low voltage grid calculations (see Figure 5.13). The SLP is more appropriate during the night at this voltage level than for the test site and the low voltage level. The $CC$s of all calculations shows a steep decrease at around 4:00 UTC because of increasing effects of the SLP while the measurements stay at a constant level. The $CC$ of both calculations considering the PV feed-in power increases again to a $CC$ of approximately 0.8 while the SLP remains on 0.6. All $CC$ curves start to decrease at 8 UTC and run together in the afternoon at 12:00 UTC on around 0.3. This low $CC$ value is caused by the changing amplitude of the average day curves (SLP curve decreases and calculations considering the PV feed-in power increase) while the averaged measurement is almost constant (see Figure 5.18). The $CC$ increases from 14:00 UTC to 18:00 UTC because of the decreasing effects of the PV and the increasing load during the evening peak in both calculations and measurement.

### 5.3.2 Quarter-hourly data comparison at medium voltage level

The discussion of the results of the overall investigation period is supported by scatter plots. The scatter plots in Figure 5.20 show all valid data pairs of calculated and measured data. Note, the measurement does not consider the algebraic sign of the load flow and therefore only absolute values are calculated and presented. Furthermore, the plots are distinguished based on $\gamma_s$ into the whole day, daylight hours ($\gamma_s \geq 0°$ and $\gamma_s \geq 15°$) and night ($\gamma_s \leq 0°$) to analyse effects because of the diurnal cycle.

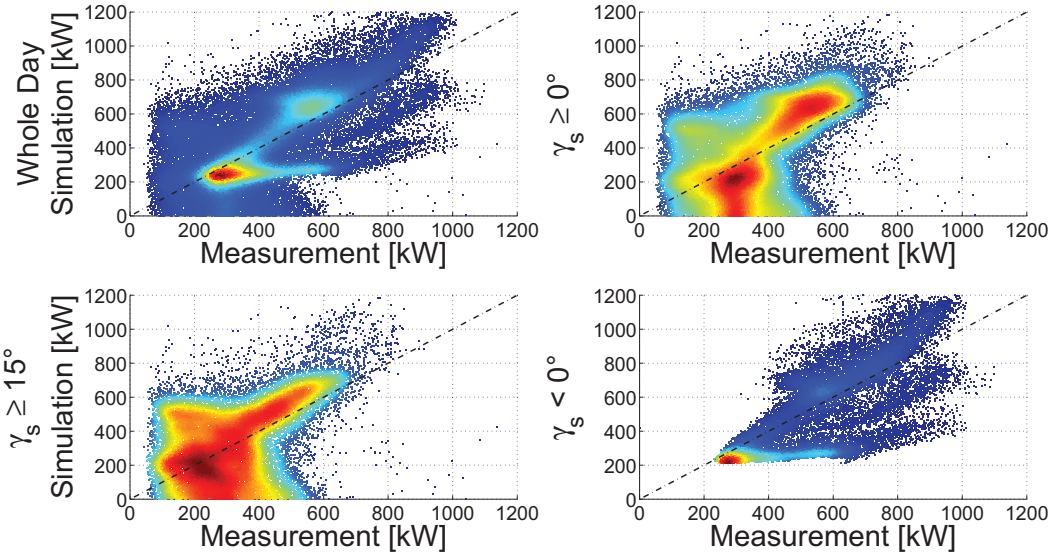


Figure 5.20: Comparison of calculated and measured absolute load flow at the medium voltage substation. The calculation is based on MACC-RAD and SLP. It is separated into different $\gamma_s$. The frequency of occurrence is colour-coded: low frequencies are blue and high frequencies are red.

The scatter plot of the whole day shows a high level of scatteredness. Two spots with a high frequency are visible. The first spot is at approximately 230 kW (calculated) and 250 kW (measured) with an almost horizontal trend to 600 kW (measured). The second spot is less frequent and located at 625 kW (calculated) and 600 kW (measured). Between both spots there is a slight trend of higher frequency of occurrence visible. Furthermore, the measurement does not reach the y-axis meaning there are no measured active power values of zero. The minimal measured value is 44.8 kW. The calculated values reach the x-axis and shows a high level of scatteredness ranging from 50 kW to 500 kW (measured). This becomes more clear in the scatter plots considering only the daylight hours.

The two spots visible in the scatter plot of the whole day are also visible in the scatter plots considering only data when $\gamma_s \geq 0°$. The trend of higher frequency

of occurrence between both spots is visible here, too. The scatter values at high amplitudes are not within this period and a positive bias occurs at higher active power values above 400 kW. Furthermore, the high scatteredness at the x-axis is also present. However, this is based on a mathematical effect when reversal load flow values with a positive bias are expressed as absolute values. The negative values with a positive bias are symmetric with respect to the zero point and are projected to absolute values with a negative bias [1]. A part of the underestimation at low active power values is in fact a reversal load flow with an overestimation. This becomes more clear when the irradiance is considered (see below and Figure 5.21).

The limitation on data values where $\gamma_s \geq 15^\circ$ reduces the level of scatteredness again. A high frequency of occurrence is given both above the main diagonal indicating an overestimation and in the range from 200 to 400 kW (measured) below the main diagonal. As mentioned before, this underestimation area is the region where the projected reversal load flow values are plotted.

The scatter plot of the nighttime is dominated by a spot of high frequency of occurrence at 70 kW (measured) and 210 kW (calculated). From this spot a horizontal trend line of higher frequency of occurrence is visible up to 600 kW (measured). This is the variation between the measurement and an almost constant load assumed by the SLP at night. Furthermore, several points are around the main diagonal up to 1,000 kW (measured) and with several points below the main diagonal reflecting an underestimation of the load. This level of scatteredness is a result of the missing variance and load dependency on the real air temperature profile.

To conduct a more detailed investigation into the results and the symmetry with respect to the zero point, the data are separated according to $kC$. The data with a $kC \leq 0.4$ representing low irradiance cases such as overcast situations and the data with a $kC \geq 0.75$ representing cases with high irradiance values such as clear-sky. These data are shown in Figure 5.21.

The results considering the data with a $kC \geq 0.75$ show a high level of scatter in the range from 50 kW to 700 kW (measured). A high density of the values is visible from 200 kW to 400 kW (measured) and 0 kW to 200 kW (calculated). The high solar irradiance leads to a high PV feed-in power and presumably reversal load flows. The data pairs of calculated and measured values for overestimated reversal load flows are projected as an underestimated positive load flow on the scatter plot.

[1] An odd function has a symmetry with respect to a point if the condition $f(-x) = -f(x)$ is met (Gellert *et al.*, 1969). The function of the calculations and measurements giving only the absolute value is defined as $|f(|x|)|$. The insert of this function into the condition is given as: $|f(|-x|)| = |f(x)| = f(x)$ and $|-f(|x|)| = |-f(x)| = f(x)$.Therefore, the condition is met and measured and calculated reversal load flows with a positive bias are symmetric with respect to the zero point and occur as absolute values with a negative bias in the scatter plot.

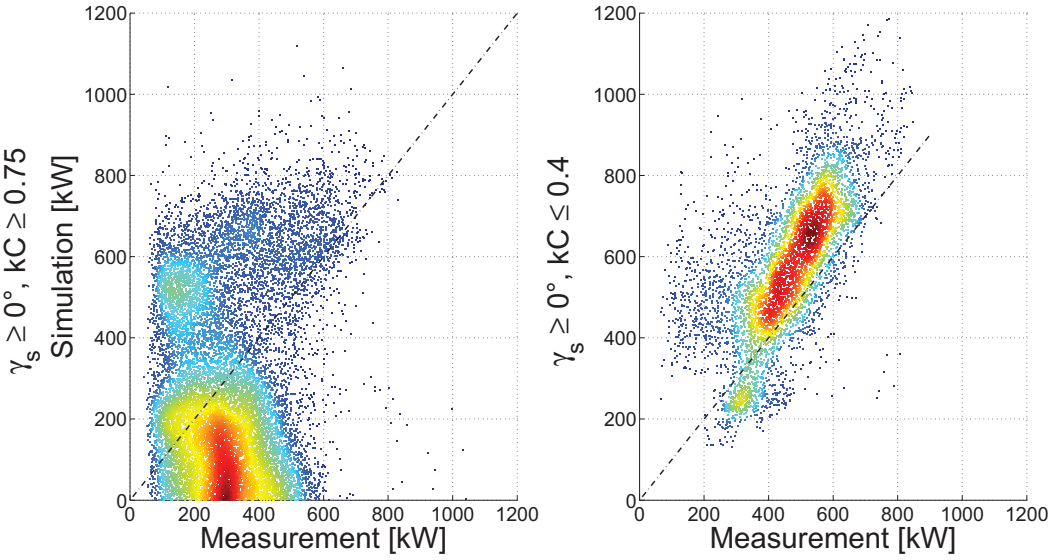


Figure 5.21: Comparison of calculated and measured absolute load flows at the medium voltage substation for $\gamma_s \geq 0°$. The left plot shows only data where $kC \geq 0.75$ and the right plot only data where $kC \leq 0.4$. The frequency of occurrence is colour-coded: low frequencies are blue and high frequencies are red.

This effect is not visible in the cases when $kC \leq 0.4$. In these situations the PV feed-in power is low and the load flow is dominated by the consumption. The scatter plots shows a similar shape as for the low voltage level (see Section 5.2.3) with an overestimation above the main diagonal and a reduced level of scatter.

# Chapter 6

# Result Discussion

This chapter focuses on the results drawn from the previous chapter. This analysis integrates and compares these results with existing results in literature.

## 6.1 Simulation of PV fleet feed-in power

The PV feed-in power of the PV fleet represents the generation side of the investigated test site. The PV feed-in power of both the PV fleet and the single PV systems can be calculated based on satellite-derived irradiance data.

### 6.1.1 Accuracy of the PV model

The PV feed-in power of single PV systems is simulated with the presented PV model (see Section 4.1.1) in 15 minute resolution for a low voltage grid area and validated against smart meter measurements (see Section 5.1.1). The normalized statistical measures *RMSE* and *ME* show that the PV feed-in power simulation errors are independent of the PV system size and comparable with results in the literature but with a higher temporal resolution (e.g. Drews *et al.*, 2007; Stein *et al.*, 2010). The values are satisfactory for grid planning issues and the positive *ME* is considered as additional margin of safety threshold in grid operation according to Meier (2014). The comparison of the results using satellite-derived irradiance data with simulations considering ground-measured irradiance data of the nearby pyranometer show a reduction of the *ME* (see Section 5.1.3). This increase in the accuracy is justified by the difference of spatial averaged irradiance information as provided by satellites and a point measurement by e.g. pyranometer (Zelenka *et al.*, 1999).

Further reasons for the overestimation of the PV feed-in power are assumptions

describing PV system losses or reductions of the effective $P_{STC}$. For example, the temperature models estimating the PV cell temperature use the 2m air temperature of meteorological stations which can differ from the air temperature on a roof (Jakubiec and Reinhart, 2013).

Furthermore, the degradation of the PV systems is not taken into account in the PV model. This leads to an overestimation of the present $P_{STC}$ which is lower than the initial $P_{STC}$, especially for thin film PV technologies (Vázquez and Rey-Stolle, 2008). It is assumed that the combination of a PV degradation model with the installation date from the system data provided by the DSO can reduce this error source. However, without detailed information about the installed PV systems and the maintenance of these data also other reasons can affect the value of $P_{STC}$. Examples of such reasons are the re-powering of a PV system due to the burglary of PV modules or due to manufacturer's warranty. Furthermore, the detailed analysis of installed PV systems based on aerial images showed some PV systems with an increased covered area and therefore an increased nominal power. This additional installed PV power was not reported to the DSO and breached various regulations and laws (e.g. EnWG, 2013; EEG, 2014; NAV, 2006; TAB, 2009). Therefore, the accuracy increases with the amount of information available from the DSO.

### 6.1.2 Impact of varying the PV model algorithms

The variation of the data sources and algorithms used confirms the mentioned results and informs them with more details (see Section 5.1.3).

The overestimation of the PV feed-in power of the PV fleet significantly correlates with the application of the MACC-RAD irradiance data while the usage of the nearby pyranometer data leads to an underestimation. However, it is expected that the results of such an analysis will confirm the dependency of the $ME$ on the satellite irradiances as shown in Table 3.1.

Furthermore, the consideration of the correct orientation of each PV system enhances the statistical measures as expected due to lower errors of the system orientation mismatch. The differences between the manual in-situ measurements and the orientation angles based on the LiDAR data are small.

An important result is that a linear model for PV modules leads to significantly higher error values. Such a model assumes a linear relation between irradiance and $P_{STC}$. The reason for the higher error is the neglect of the low light performance of the PV modules. In combination with the $GHI$ distribution this leads to a significant annual underestimation.

At the test site, the isotropic $DTI$ calculation algorithm performs best followed

by the Reindl and Perez models. The reasons for this unexpected result need further investigation and an extension of the irradiance measurements at the test site. A more significant difference between the simple isotropic model and the empiric Reindl and Perez models similar to direct irradiance comparison was expected (Gueymard, 2009).

The application of the cell temperature models according to Faiman (2008) tend to overestimate the PV feed-in power. Both others models only slightly differ.

The PV inverter models investigated and the applied Sun position algorithms minorly affects the statistical measures. However, a noteable exception is the Sun position algorithm according to DIN 5034-2 (1985) leading to higher *RMSE* as well as lower *ME* and *CC* values.

An overview of the variations of both the irradiance and orientation angles source is shown as a box plot in Figure 6.1.

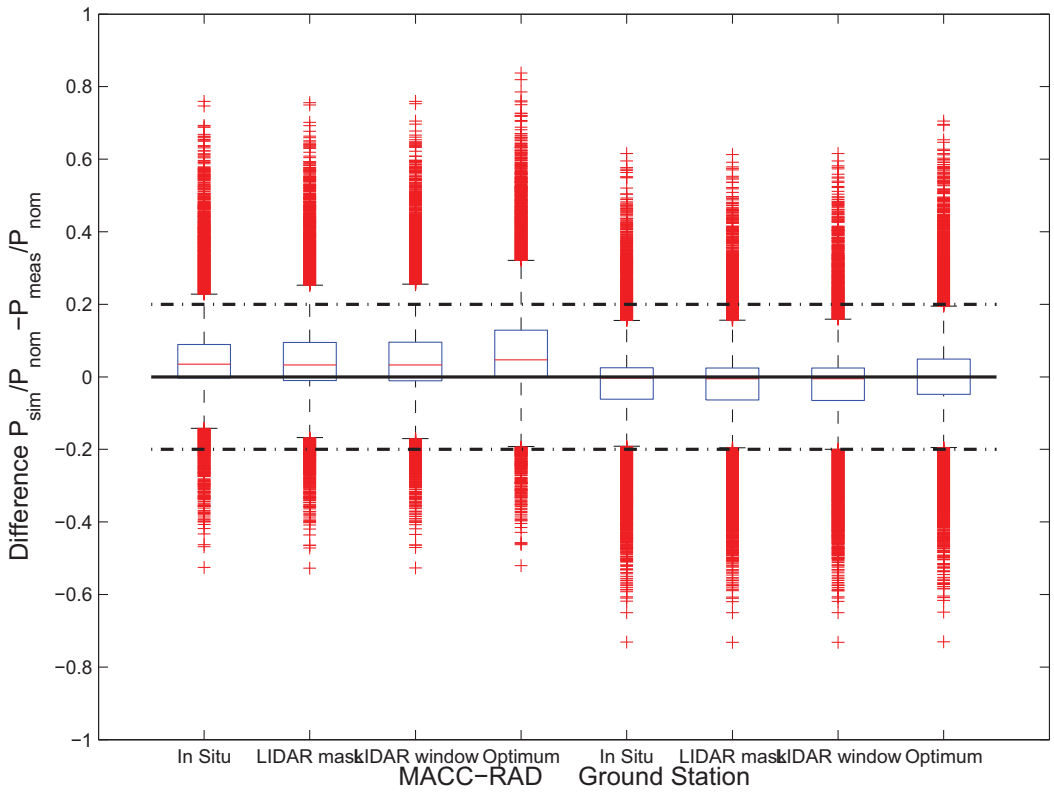


Figure 6.1: Normalized differences of the applied PV model and the measurements depending on the used irradiance data source and considered PV system orientation data. The red horizontal lines illustrate the median of the data while the blue horizontal lines represent the 25th and 75th percentiles, respectively. The whiskers extend to the most extreme data points not considering outliers, and represent 99.3 % of all data. The outliers are plotted individually as red crosses.

The four columns on the left side consider the irradiance data provided by MACC-RAD while the four columns on the right side consider the ground-based irradiance measurement. The four columns differ in the source of the PV system orientation angles (see Section 3.3.2.2).

In conclusion, the spread of the difference between calculations and measurements is mostly within a range of 20 % of the $P_{STC}$. An exception is the combination of MACC-RAD with an assumed optimal PV system orientation where the whisker and therefore the difference reaches 30 %. Outliers ranges from -70 % to 80 % depending on the data source combination. However, for the calculation considering the satellite irradiance data, 75 % of the differences are below 10 % $P_{STC}$. The 25th percentile is around zero. As mentioned, the satellite irradiance data provided by MACC-RAD overestimates the PV feed-in power. The differences are lower if ground-measured irradiance data are taken into account. Moreover, the overestimation no longer occurs and the median is approximately zero. The difference between simulation and measurement is below $\pm$ 20% for 99.3% of all data.

### 6.1.3 Detection of exceeding a PV feed-in power threshold

The detection of PV feed-in power higher than 70 % $P_{STC}$ is of interest to the DSO according to EEG (2014). Scores are used to describe the ability to detect generation in excess of the 70 % threshold based on satellite-derived irradiance data (see Section 5.1.2).

With a *PC* above 0.90 the trend of the simulated values matches well with the measurements. However, the $THS$ considers hits where simulation matches with the measured threshold exceedance and decreases with errors and misses. This score shows only average values due to the low ratio of threshold exceedance to the rest of the time. This is also expressed in the *FAR* ranging from 33 % to 77 % for the single PV systems and 83 % for the PV fleet, respectively. If a threshold exceedance is simulated the probability is significant that no exceedance occurs. The reason for this is the overestimation of the PV feed-in power which is also represented in the $CTB$. The values of $CTB > 1$ imply that a threshold exceedance is more often calculated than occurs.

In greater detail, the *POD* describes the probability of correct detection. For the single PV systems the *POD* is at least 74 %, meaning that three of four exceedance events are correctly detected. This value decreases to 66 % for the overall PV fleet. Vice versa, the $POFD$ is at most 9 % for the single PV systems and fall to 6 % for the PV fleet. This means that the probability of a calculated event when no threshold exceedance occurs is seldom.

In summary, the determination of a PV feed-in power threshold exceedance is possible and the miss of an event is rare, however, the approach suffers from a high rate of false alarms due to the irradiance overestimation. Furthermore, the threshold detection for single PV systems strongly depends on the PV system modelling and accurate data e.g. orientation angles. Therefore, the possibility of PV feed-in power threshold detection should be considered with care as a systematic overestimation has been found. Further reduction in satellite biases are necessary to increase the detection accuracy. However, this error will result in more grid reinforcement than necessary. Finally, any planning based on this scheme will not cause any critical situations for the grid safety.

## 6.2 Transformer load flow

The calculation of the load flow at a medium-to-low voltage transformer considering satellite-derived irradiance data is performed for a single test site. Therefore, the applicability in other regions can be assumed but would needs further investigation. The statistical measures show an annual cycle. The monthly *rME* overestimates during summer due to the overestimation of the PV feed-in power. In winter the *rME* is lower because of the higher load consumption and reduced irradiance values. The monthly *rRMSE* values are almost constant during the year but also show higher values in the summer months. This is caused by the higher variance of the PV feed-in during this period. Furthermore, the results significantly depend on the load profile type.

### 6.2.1 Load flow calculations in annualized diurnal cycles

The analysis of annualized average days makes deviations and errors in the diurnal cycles visible (see Section 5.2.2). The consumption during the night is underestimated in the annualized observation. It is assumed that this is a result of the neglect of the off-peak energy share in the load profiles used. The simulated and measured time series do not show the typical peak around noon as does the SLP data. This peak in consumption is covered by the local PV feed-in power. This result is similar to other locations according to the literature (Wirth, 2015; Stetz *et al.*, 2012).

The comparison of the simulated and measured data show higher errors during the morning and evening hours. The impact of the PV is small during these periods. In addition, the deviations between both SLP and NoSLP data are small. Especially in the morning and evening hours differences occur due to the limited statistical

nature of the NoSLP data (Heilscher *et al.*, 2010). Especially in the evening, the errors are high and there is a mismatch between assumed load profile and measured profile. However, the PV feed-in power is low during this period because of the low *GHI*. Therefore, it can be concluded that the load profile strongly affects the accuracy of the approach during the periods of the low sun elevation angles.

As expected, the variability correlates with the diurnal cycles because of the changing conditions in the consumption and PV feed-in power. This is also visible in the values of the *CC*. These are higher during the sunlight hours and lower during the night. The low *CC* at night is a result of the consumption underestimation and the neglected temperature dependency.

In conclusion, the load profile type used has a strong impact on the accuracy. This is especially true during the hours without a significant PV feed-in power impact. These results are comparable with the literature. Stetz *et al.* (2012) also found a strong correlation between measured load profiles and SLP in the analysis of consumption measurements of 1077 smart meters in three test regions in Southern Germany. The measured profiles showed regional effects in the morning and evening peaks and higher consumption during the night than assumed by SLP. Furthermore, their analysis shows that the PV feed-in does not reduce the daily-based peak load which is used for the planning of the electric grid. However, the daily-based off-peak load decreases with increasing PV power capacity installed. These are similar results to the comparison of SLP and NoSLP with the measured load profile in this work. Therefore, it can be assumed that the test site is representative for calculating the annual values.

### 6.2.2 Quarter-hourly load flow at low voltage level

The analysis of all 15-minute average data also clearly shows the overestimation during the daylight hours (see Section 5.2.3). The level of scatteredness is caused by the PV feed-in power as well as the consumption.

Furthermore, a high level of scatteredness is also visible at night time because of the deviation of the load profile used and the load flow measurements. The difference between the assumed night consumption and the variable real consumption is appreciable. Especially the low temperatures in February 2012 led to higher errors (see Section 5.2.1).

The level of scatteredness depends more on the load profile used than on the irradiance source. This is another piece of evidence for the strong impact of the load profile type on the calculation approach.

### 6.2.3 Investigation of the energy values

The overestimation of the PV feed-in power is also visible in the analysis of the energy values of each system (see Section 5.2.4). The energy balance gives an indication of the different shares of the overestimation, however it has to be considered with care due to the limited investigation period of two months. Furthermore, it is also limited because of the single satellite-derived irradiance source.

The most bias is caused by the irradiance provided by MACC-RAD probably because of the comparison of a spatially averaged irradiance to a single point measurement. The overestimation of MACC-RAD is also quantified in the direct comparison to the ground-measurement at the university campus (see Section 3.1). If irradiance data from the nearby pyranometer are taken into account, the overestimation is reduced.

As expected, the bias of the PV model is independent from the irradiance source used. The assumption of an optimal orientation of each PV system leads to an additional positive bias. The impact of the mismatch is not significant because of the high number of investigated PV systems with almost optimal orientation. However, this overestimation is smaller than the effect of a neglected air temperature and wind speed influence. The underestimation occurring because of the neglected PV system cooling effects compensate parts of the irradiance-caused overestimation.

The significant effect of the load profile is also evident in the energy balance. In the investigated test site, the error of the PV feed-in power calculation ranges only from 22 % to around 50 % of the *rEM* at the transformer. This variation of the share of the *rEM* depends on the irradiance source.

### 6.2.4 Detection of reversal load flows at the distribution grid transformer

The DSOs are interested in the detection of reversal load flows. The knowledge about the direction is helpful in the strategic grid planning as well as in the operation of the grid because of different thresholds for voltage drop and voltage rise (Stetz *et al.*, 2012).

The scores describing the accuracy of the reversal load flow detection depends more on the load profile used than on the source of irradiance. Furthermore, to avoid statistical averaging effect only times where $\gamma_s \geq 15°$ are summarized in this section. Both *PC* and $THS$ show good results meaning that the detection of reversal load flows is accurately possible. The *FAR* is lower than in the PV feed-in power threshold detection. Only approximately 15% of the calculated reversal load flows

do not occur. This is also expressed in the $CTB$, which also shows an overestimation. The reason for this overestimation is the overestimated PV feed-in power as well as the uncertainty of the real load situations.

Furthermore, if the VDI results are assumed as an outlier, at least 95 % of the occuring reversal load flows are detected correctly with the satellite-based irradiance data. However, if no reversal load flow occurs, the overestimation of the PV feed-in power leads to a higher rate of false detections. The $POFD$ ranges from 30 % to 50 % depending on both the load profile used and the irradiance source.

## 6.3 Medium voltage level

The upscaling of the approach for several transformers can be used for the calculation of the load flow at the substation of medium voltage feeders. However, consumers and generators e.g. larger commercial customers directly connected to the medium voltage are not considered (see Section 3.4).

### 6.3.1 Medium voltage load flow simulations in annualized diurnal cycles

The annualized day highlights the average intra-day effects of the PV feed-in power because of the diurnal cycles (see Section 5.3.1).

The consumption at night is underestimated. Probably this is a result of the neglected temperature-depending load profiles for heat pumps and off-peak storage heating as well as additional loads such as traffic lights and mobile base stations. The consideration of such profiles and loads requires a high level of information availability at the DSO. Typically, this information is only available in different data systems or in hardcopy form. It is strongly recommended that these data are made automatically accessible.

Furthermore, around noon the load flow is also underestimated. However, this is probably caused by the overestimation of the PV feed-in. In this example, the consideration of the PV system orientation or the assumption of an optimal orientation results in differences of around 100 kW.

The non-occurrence of the peak-consumption around noon is appreciable. The SLP assumes this peak consumption and it is evident that it does not occurs during clear-sky days with a high PV feed-in power. However, even in the annualized day the peak does not occur. Of course, this results in high errors expressed in the statistical measures.

As expected, the high PV feed-in power leads to a high $STD$ during the day following the diurnal cycles. The minimum of the $STD$ is given in the evening. The PV does not affect the peak consumption in the evening. This peak is visible in both simulation and measurements. There are differences in the amplitude and duration due to the assumed load profile and the measured consumption.

### 6.3.2 Analysis of the investigation period in quarter-hourly resolution

The analysis of the 15-minute average values shows the disadvantage of measured values without load flow direction information (see section 5.3.2).

The level of scatteredness is high compared to the the scatter plots of the low voltage transformer. The errors at the low voltage level are significant and it can be assumed that these errors increase with the number of transformers connected to a medium voltage feeder.

The simulation overestimates the load flow at the substation in a similar manner to a single low voltage transformer. MACC-RAD shows a positive bias for $GHI$ just as the PV model overestimates the PV feed-in power. Furthermore, an underestimation of the current consumption can occur because SLP is optimized only for accurate annual energy values and not necessarily for single dedicated values during the day. While the standard deviation of the SLP for residential households ranges from 5 to 10 % of the average profile the standard deviation of commercial and industrial SLPs can reach 20 % (Engels, 2000). The level of scatteredness is high during the night. As mentioned before it is assumed that this is a result of the neglected temperature-depending load profiles for heat pumps and off-peak storage heating.

The classification of regular load flows and reversal load flows as well as the correlation of load-driven and PV-caused utilisation is not possible with the application of absolute values. Especially if different voltage drop thresholds have to be met for peak load and peak generation, respectively, it is recommended that the direction of the load flow instead of the absolute values is known (Stetz *et al.*, 2012). This disadvantage is also visible in Figure 6.2. The simulated load flow reaches values of at least -400 kW meaning a reversal load flow. The measurements only detect the absolute values and the grid control center is not able to detect the reversal load flow based on these measurements. Without additional data or measurements the grid control center is not able to recognize that this medium voltage feeder generates more power than consumed.

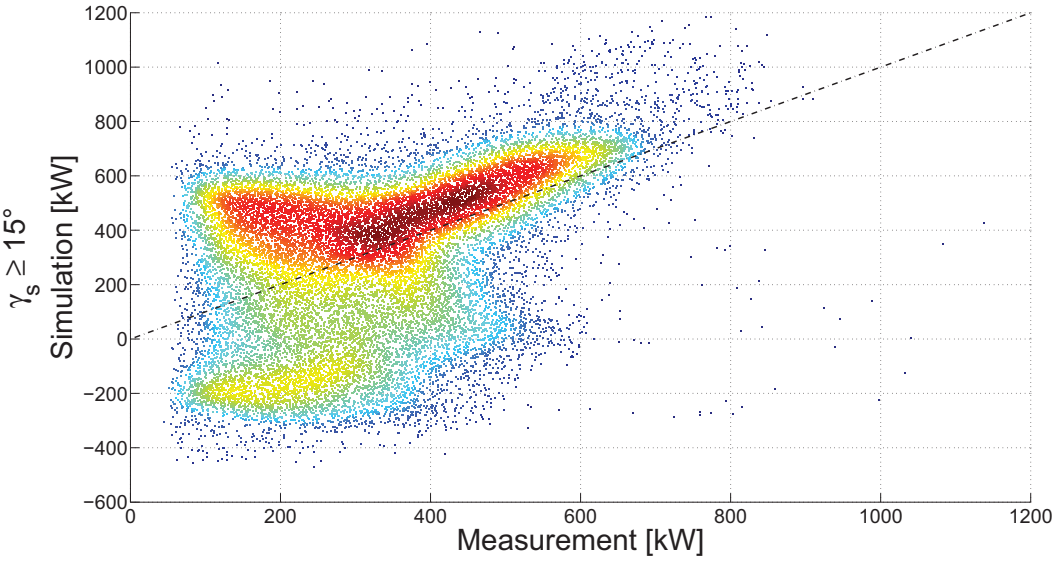


Figure 6.2: Comparison of calculated and measured load flow at medium voltage level. The calculation considers the load flow direction. The frequency of occurrence is colour-coded: low frequencies are blue and high frequencies are red.

# Chapter 7

# Conclusion

This chapter summarizes the work including the validation and outcomes as well as an overview of the model and a brief discussion of the results. Furthermore, prospective users will find recommendations here for practical application.

## 7.1 Summary

### 7.1.1 Transformer load flow computation model

A method for the load flow calculation at low voltage transformers in areas with a significant capacity of PV systems is introduced. The usage of satellite-derived irradiance data makes the method applicable at least all over Europe. Furthermore, the method is also scalable to higher voltage levels e.g. medium voltage feeders.

The principles of the method are shown in Figure 7.1. The PV feed-in power time series of each single PV system are computed using irradiance data from satellites and well-known irradiance translation and PV models. Additional meteorological data are provided by ground stations and show strong correlation over the distance to the area of interest. Important parameters for the PV system modelling such as location or rated power are provided by the DSO database (i.e. SOPTIM). Additional data such as the orientation of the PV modules provided by laser-scan data (i.e. LiDAR) improves the model accuracy.

The sum of the single PV system time series is the PV feed-in power of the PV fleet connected to the transformer and the generation part of the load flow. The consumption time series is represented with assumed synthetic load profiles scaled to the annual energy consumption. This annual energy consumption is also provided by the DSO (i.e. SAP IS-U). The synthetic load profiles are used due to the lack of time series information of the real residential customers.

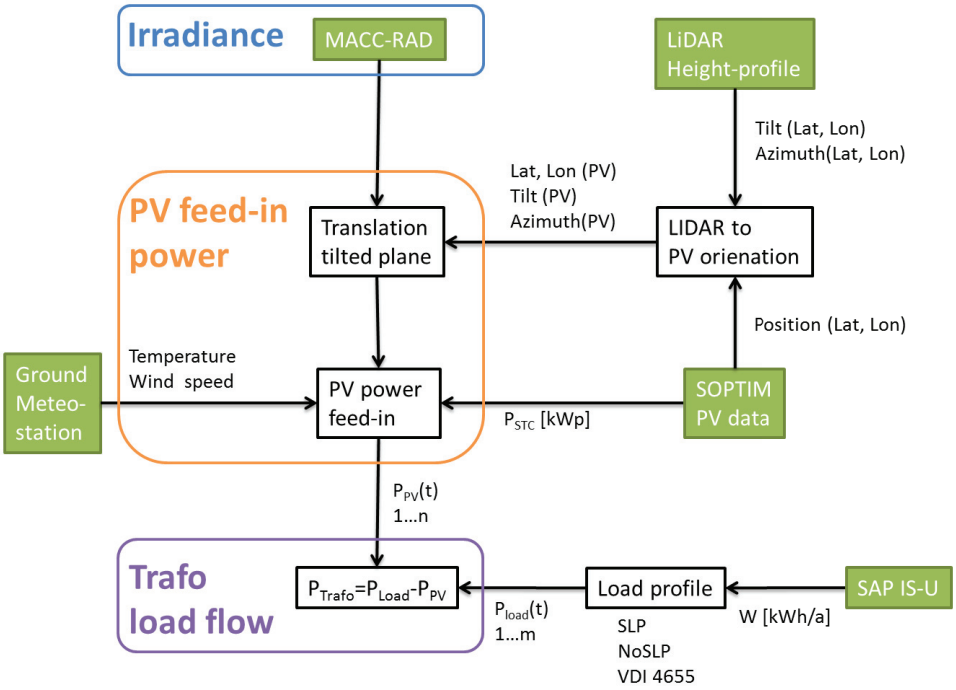


Figure 7.1: Method for the load flow calculation at low voltage transformers in areas with a significant number of PV systems based on satellite-derived irradiance data.

### 7.1.2 Validation results

All calculated time series are validated against independent measurements at each level i.e. PV feed-in power, load flow at the transformer at both low and medium voltage levels. Furthermore, different input data and assumptions are investigated to determine the impact on the calculation model. The statistical measures, which depend on simulation results, are compared. Thereby, this study disregards missing and suspect measurements.

The work demonstrates the accuracy of the PV feed-in power calculation of residential PV systems considering satellite irradiance data. The errors are independent of the rated power of the PV systems and therefore applicable for small and large residential PV systems. However, the accuracy decreases due to wrong or incomplete orientation data. The overestimation of the PV feed-in power is considered as an additional margin of safety threshold that is welcome in grid operations.

The model calculates the load flow at a low voltage grid transformer. Especially the assumed load profiles lead to a significant error because of their statistical nature. The second significant error is caused by the satellite-derived irradiance data. A third, smaller source of error is the PV model. The load flow at a medium voltage feeder is comprised of the sum of several distribution transformer load flows.

The model does not consider additional generators or consumers who are directly connected to the medium voltage feeder. Furthermore, the errors increase at this scaled-up level.

Additionally, the application of threshold detection is investigated. Scores express the accuracy of the calculation which indicates when individual systems exceed a threshold. The study analyses when the PV feed-in power of individual PV systems exceeds 70 % of the nominal power threshold. For the low voltage grid transformers the occurrence of reversal load flows is examined.

The possibility of PV feed-in power threshold detection should be considered with care because of the systematic overestimation. However, this error would result in more grid reinforcement than truly necessary. At least, any planning based on this scheme would not cause any critical situations for the grid security. A further reduction in satellite biases are necessary to increase the detection accuracy.

DSOs are interested in the occurrence of reversal load flows. Similar to the PV feed-in power threshold detection, the detection of reversal load flows depends on the accuracy of the input data. Additionally, the errors of the load profile time series have a strong impact on the detection. The PV feed-in power overestimation leads to an overestimated number of reversal load flows. Therefore, a reduction of both irradiance bias and PV model bias will increase the accuracy.

### 7.1.3 Result conclusion

The essence of the work and results is described in this section.

The differences between the investigated Heliosat methods have no significant influence on the results of the transformer load flow calculation. As expected, the usage of irradiance data of an accurate ground measurement nearby reduces the errors. However, the undisputed advantages of satellite-based irradiance data are the long-term history and the unlimited application to different locations.

The PV model affects the accuracy of the simulated PV feed-in power. However, the difference in the accuracy of the necessary algorithms only minimally affects the results of the PV fleet feed-in power calculations. The effects and errors of the irradiance, ambient data as well as the knowledge of the recent PV parameters cause higher errors. Therefore, simple but fast models can be used. Nevertheless, the PV module model should take into account the non-linear behaviour of the PV. A simple linear relation to the irradiance leads to significant errors.

The calculation of the load flow requires the sum of the feed-in power of the overall PV fleet. The assumption of an optimal orientation of all PV systems leads to an overestimation due to an invalid coincidence factor. The consideration of the

orientation angles of each PV system in a small area such as a low voltage grid increases the accuracy. The differences between the manually ascertained orientation data and LiDAR data are negligible.

The load time series based on statistical load profiles have a significant influence on the accuracy. Overall, the SLP shows the best results in this case and can be assumed at the investigated area according to Engels (2000). Especially these errors as well as the PV feed-in power overestimation affects the accuracy of the up-scaling to the medium voltage level.

## 7.2 Recommendations

This section summarizes some recommendations based on the experience gathered in the research leading to this work.

Nowadays, the effects of a significant number of PV systems on the electric grid and load flows have to be considered in grid planning and grid operations. The calculation of both PV feed-in power and load flow at the transformer based on satellite irradiance data is useful in the grid planning of low voltage grids. The available long-term history of the irradiance data allows the determination of probability of *GHI* values and the PV feed-in power. Furthermore, these long-term data can be used for reanalysis of the grid planning approaches and strategies. The results of such a reanalysis can be used for the reconsideration of the recent approaches. In combination with a roof potential analysis, the irradiance time series can be used to extrapolate data and therefore calculate the impact of a theoretically higher number of PV systems. This calculation also includes the determination of the PV hosting capacity of the grid.

The orientation angles should be taken into account for analysis and calculations at the low voltage level. The low number of PV systems and houses as well as the small spatial land area disallow the usage of spatial smoothing and lumped PV models.

Stetz *et al.* (2012) recommend the measurement of the direction of the load flow and justify this recommendation with the economic effectiveness of non-symmetric split of the voltage band at peak-load and generation. This work confirms the recommendations. The neglect of the direction can lead to misunderstandings of the load flow results. Since recognition of occurring reversal load flows is not existent in the measurements used the calculation appears to be flawed. However, this is not a true error but rather a mathematical effect which does not differentiate between the algebraic signs.

# Chapter 8

# Outlook

This work describes and analyses the calculation of transformer load flow in low voltage grids with high PV penetration ratios based on satellite-derived irradiance data. The analysed scheme assumes several parameters because of missing or unavailable data. This chapter will give a brief outlook of possible further improvements.

Currently, data on the PV systems originate from newly-developed estimation methods or even merely assumptions. An improved PV system model considering actual data will reduce the calculation errors. The PV model takes into account only one PV system orientation because of the rare occurrence of PV systems with multi-orientation. However, a rise in installations of PV systems with East-West orientation to increase the self consumption can lead to a more frequent occurrence of multi-orientations and will make the orientation modelling more complex.

Furthermore, the degradation of the PV systems is neglected. The consideration of annual degradation rates can improve the accuracy and reduce the overestimation of the PV feed-in power. The value of the annual degradation rates varies (Gutnik *et al.*, 2012; Ndiaye *et al.*, 2013) and has to be investigated in future for a representative approach. It is expected that the DSO can provide the necessary installation dates of each PV system for the determination of the system age.

Moreover, shadowing effects on the PV module generators are not taken into account yet. The determination of shadowing time-series based on backwards ray-tracing algorithms for the irradiance estimation is a topic of different studies (e.g. Larson and Shakespeare, 2003; Jakubiec and Reinhart, 2013; Fath *et al.*, 2015). It is expected that the combination of this ray-tracing algorithms with the model introduced in this work will reduce the calculation errors.

One main source for errors is the load profile. It is assumed that the consideration of the temperature-dependency as well as the energy in peak and off-peak

periods will improve the load profiles. A detailed investigation of synthetic load profiles (Dickert and Schegner, 2011; Pflugradt and Platzer, 2012) makes sense. Furthermore, the errors will be reduced if consumption time-series based on smart meter measurements are available.

The magnitude of the load flow at the transformer is the sum of the load flow of each feeder. This load flow causes voltage drops depending on the detailed grid structure and asset types. The introduced method can be combined with detailed grid models based on a grid simulation software and will provide detailed voltage drop information for certain times and locations. This is important information for the DSO in order to establish efficient grid planning data as well as for nearly real-time grid operation.

Mostly, the albedo is assumed as a constant value in this work. However, the albedo also affects the accuracy of the model and varies in time. The difference between accurate albedo measurements and constant albedo assumptions is investigated in Gueymard (2009). The influence on the irradiance increases on steep tilted planes e.g. facade-mounted PV systems. However, albedo values are also accessible by satellites e.g. for PV potential calculations in urban areas (Borfecchia *et al.*, 2014). These satellite-derived albedo values are also required for the Heliosat-4 method used in the MACC-RAD service. The albedo time series can be easily used in the PV feed-in power calculation.

The PV model uses temperature and wind data provided by ground-based meteorological stations. It is expected that this limitation to ground data can be avoided. The McClear irradiance model considers aerosol data provided by the ECMWF forecast (Lefèvre *et al.*, 2013). These forecast data include temperature and wind speed as well. Using these meteorological data probably will increase the calculation errors however are useful when ground-based measurements are unavailable.

A main advantage of the method investigated in this work is the modular scheme. The satellite-derived irradiance data can be replaced with irradiance data from other sources e.g. nowcasting methods based on satellite-derived cloud motion vectors or irradiance data from numerical weather prediction systems. This combination provides a forecast of both the PV feed-in power and the transformer load flow. It is expected that this is an important point for a proactive distribution grid operation. For example, the demand for the integration of renewable energy led to stronger combination of forecast techniques and power systems at both transmission and distribution levels (Köhler *et al.*, 2015a,b).

# Chapter 9

# Appendix A: Definition of Statistical Measures

This chapter describes the statistical values and methods used based on Beyer *et al.* (2009) and Wilks (2011). These statistical measures allow to compare the results from the different variations.

## 9.1 Definition of the statistical values

This section defines the different statistical measures used in this work to compare the results of the calculations. This is necessary because the comparison of several thousands of data points is not efficient. The measurements are considered as reference values.

The mean ($\bar{x}$) of a data series $x(i)$ containing $i$ elements is defined by

$$\bar{x} = \frac{1}{N} \sum_{i=1}^{N} x(i), \tag{9.1}$$

where $N$ is the number of data.

The values are distributed around the mean. This can be expressed with the standard deviation ($STD$) quantifying the amount of variation of a data set. The $STD$ is defined by

$$STD = \sqrt{\frac{1}{N} \sum_{i=1}^{N} (x(i) - \bar{x})^2}. \tag{9.2}$$

The mean error ($ME$), also denoted as bias, quantifies the difference of a simu-

lation or calculation to the measurement and is defined by

$$ME = \frac{1}{N}\sum_{i=1}^{N}\left(x_s(i) - x_m(i)\right) = \overline{x_s(i)} - \overline{x_m(i)}, \tag{9.3}$$

where $x_s(i)$ is the simulated data and $x_m(i)$ is the measured data at time $i$.

The *RMSE* can be calculated from the simulated and measured data sets by

$$RMSE = \sqrt{\frac{1}{N}\sum_{i=1}^{N}\left(x_s(i) - x_m(i)\right)^2}. \tag{9.4}$$

The corresponding relative measures are related to the mean of the absolute measured values and given by

$$rME = \frac{ME}{\overline{|x_m|}} \tag{9.5}$$

and

$$rRMSE = \frac{RMSE}{\overline{|x_m|}}. \tag{9.6}$$

This definition differs from the definition in Beyer *et al.* (2009) where the measures only are related to mean of the measured values. The definitions in Beyer *et al.* (2009) were made for radiation values and negative values cannot occur. This definition is also valid for the PV feed-in power neglecting self-consumption of inverters during night. However, the load flow at transformers can be bidirectional, with positive and negative values. Therefore, the definition is extended to the mean of the absolute measured values. This avoids high relative error values because of mean values close to zero while positive and negative values cancel each other out.

Especially, to compare the error values of different rated PV systems, the *ME* and *RMSE* are normalized to the PV nominal power $P_{STC}$ by

$$nME = \frac{ME}{P_{STC}} \tag{9.7}$$

and

$$nRMSE = \frac{RMSE}{P_{STC}}. \tag{9.8}$$

The correlation coefficient (*CC*) quantifies the linear correlation between two

variables $x_s$ and $x_m$ and is defined by

$$CC = \frac{\sum_{i=1}^{N} \left(x_s(i) - \overline{x_s}\right) \cdot \left(x_m(i) - \overline{x_m}\right)}{\sqrt{\sum_{i=1}^{N} \left(x_s(i) - \overline{x_s}\right)^2 \cdot \sum_{i=1}^{N} \left(x_m(i) - \overline{x_m}\right)^2}}. \tag{9.9}$$

A value of $CC = 1.0$ means a total positive correlation and $CC = -1.0$ means a total negative correlation. If the variables do not correlate, the result is $CC = 0.0$. The interpretation of the non-extreme values follows Kronthaler (2014). A strong positive correlation is given for $1.0 > CC \geq 0.6$ while a weak positive correlation is given for $0.6 > CC \geq 0.3$. A correlation cannot be assumed for $0.3 > CC > -0.3$.

The relative error of measurement ($rEM$) is defined as the difference between a measured values and a corresponding reference value, whereat the reference value can be the true value, the conventional true value or the expectation. The difference between true value and conventional true value can be neglected (DIN 55350-13, 1987). The $rEM$ is defined by

$$rEM = \left(\frac{x_m}{x_t} - 1\right) \cdot 100\%, \tag{9.10}$$

where $x_m$ is the measured value and $x_t$ is the true value, the conventional true value or expectation. In this work, the conventional true value is defined as $x_t$.

## 9.2 Definition of the scores

This section describes the definition of different scores for expressing an event detection based on a contingency table according to Wilks (2011).

A contingency table (9.1) can be set up on the basis of the analyses of the measured and calculated data in view of whether a limit is complied or not. Each event detection can be sorted in one of the four given categories. These categories are event occurred and calculated ($a$), event did not occur but was calculated ($b$), event occurred but not calculated ($c$) and event did not occur and was not calculated ($d$).

Table 9.1: Contingency table for event detection measures

| | | ***Observation*** | |
|---|---|---|---|
| | | ***Yes*** | ***No*** |
| ***Calculation*** | ***Yes*** | a | b |
| | ***No*** | c | d |

Based on the classification of the events into the four categories following scores are used to describe the accuracy of the threshold event detection. A perfect calculation means $b = c = 0$.

One accuracy measure is the proportion correct ($PC$) given by

$$PC = \frac{(a+d)}{(a+b+c+d)}. \tag{9.11}$$

The worst possible $PC$ is 0 and the best is 1. It shows the number of results with a correct simulation of events of interest.

The threat score $THS$ is given by

$$THS = \frac{a}{(a+b+c)}. \tag{9.12}$$

The $THS$ range is 0 to 1, while a value of 1 indicating a perfect simulation.

Furthermore, the false alarm rate $FAR$ describes the number of false simulation results and is defined by

$$FAR = \frac{b}{(a+b)}. \tag{9.13}$$

A perfect simulation is given for $FAR = 0$ while a complete mismatch results in $FAR = 1$.

The contingency table bias ($CTB$) is the comparison of the average calculation to the average measurement. It is defined as the ration of the number of calculated to the number of measured events by

$$CTB = \frac{(a+b)}{(a+c)}. \tag{9.14}$$

Simulations without any bias are $CTB = 1$. For $CTB < 1$ and $CTB > 1$ the events are under- and overestimated, respectively.

The probability of detection ($POD$) is defined as number of interested events which are correct simulated by

$$POD = \frac{a}{(a+c)}. \tag{9.15}$$

The range is between 0 and 1, while 1 is a perfect simulation.

The probability of false detection ($POFD$) is defined as number of interested events which are correct simulated by

$$POFD = \frac{b}{(b+d)}. \tag{9.16}$$

# Chapter 10

# Appendix B: The Heliosat-2 and Heliosat-4 method

This chapters gives a more detailed description of the Heliosat-2 and Heliosat-4 methods. Both algorithms base on satellite images and follow the basic approach according to Cano *et al.* (1986). However, Heliosat-2 and Heliosat-4 are radically different approaches for satellite-based estimation of solar irradiations at the surface. The Heliosat-2 method is a indirect and semi-empirical approach based on cloud index with an exogenous clear-sky model. In contrast, the Heliosat-4 method is a direct approach explicitly accounting for radiative transfer of the atmosphere and clouds. The empirical relation between the satellite images and the clear-sky index is not necessary anymore.

## 10.1 Heliosat-2

### 10.1.1 General approach

This section briefly describes the Heliosat-2 method. A more extended overview is given in Espinar *et al.* (2014) or in the original publications (e.g. Rigollier *et al.*, 2004). Based on the Heliosat-2 method several commercial solar databases become operational e.g. HelioClim (Blanc *et al.*, 2011).

The *GHI* at an instant time $t$ and a location $(x,y)$ is given by

$$GHI\,(t,x,y) = GHI_{cs}\,(t,x,y)\,kC\,(t,x,y)\,, \tag{10.1}$$

where $GHI_{cs}(t,x,y)$ is the irradiance under clear-sky condition at the instant time $t$ and the location $(x,y)$. The clear-sky index $kC$ is calculated by the analysis of a

time-series of Meteosat images to the current one and related to the cloud index $n$ according to the empirical relation by

$$kC = \begin{cases} 1.2, n \leq -0.2 \\ 1-n, -0.2 < n \leq 0.8 \\ 2.0667 - 3.6667n + 1.6667n^2, 0.8 < n \leq 1.1 \\ 0.05, n > 1.1 \end{cases}. \tag{10.2}$$

This relation was derived from ground measurements and Heliosat-2 data and shows satisfactory results (Hammer, 2001). According to Rigollier *et al.* (2004), the cloud index $n$ for a position $(x,y)$ and instant time $t$ is defined by

$$n(t,x,y) = \frac{\rho(t,x,y) - \rho_{ground}(t,x,y)}{\rho_{cloud}(t,x,y) - \rho_{ground}(t,x,y)}, \tag{10.3}$$

where $\rho$, $\rho_{cloud}$, $\rho_{ground}$ are the reflectances of the investigated pixel, the brightest cloud and the ground. The ground reflectance also known as ground albedo $\rho_{ground}$ is calculated by a statistical analysis of images of 30 days. This 30-days period considers the seasonal variation of the ground albedo (Hammer *et al.*, 2003). Normally, under clear-sky conditions $n$ is 0, where the observed reflectance is close to the ground reflectance. The appearance of clouds leads to an increase of $n$. It can be greater than 1 for optically very thick clouds. Values below 0 can occur under extreme clear-sky conditions e.g. unexpected absence of aerosols. The $GHI_{cs}$ is calculated by clear-sky models take into account the influence of the atmosphere (see Section 2.1.2).

The overview of the Heliosat-2 method is shown in Figure 10.1. A time series of MSG images are used to estimate the $\rho_{ground}$. The current image and the $\rho_{ground}$ map are taken into account to calculate $n$ and based on an empirical function $kC$. The irradiance at ground level is calculated combining $kC$ with the $GHI_{cs}$ provided by a clear-sky model. SOLEMI and HC3v4 differ in the clear-sky models used. SOLEMI uses the Bird clear-sky model (Bird and Hulstrom, 1981; Iqbal, 1983) while HC3v4 uses the ESRA clear-sky model (Rigollier *et al.*, 2000).

### 10.1.2 Bird clear-sky model

First, the Bird clear-sky model is shortly described. The $BNI_{cs}$ is calculated by

$$BNI_{cs} = 0.9751 \cdot BNI_{ext} \cdot \tau_r \tau_o \tau_g \tau_w \tau_a. \tag{10.4}$$

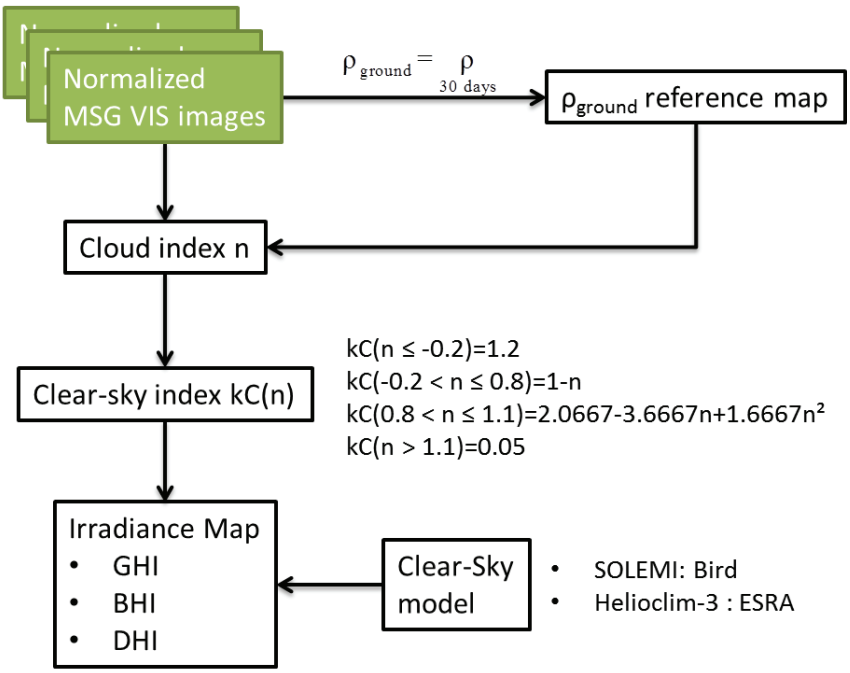


Figure 10.1: Overview about the Heliosat-2 method.

The factor 0.9751 is a spectral interval conversion factor. $BNI_{ext}$ is the irradiance for a given instant on a plane normal to the Sun's rays at the top of the atmosphere. The $\tau_r$ is the transmittance for the Rayleigh scattering. The $\tau_o$ is the transmittance related to ozone and $\tau_g$ is related to uniformly mixed gases. The $\tau_w$ describes the transmittance related to water vapour and $\tau_a$ aerosols at 550 nm. The detailed description, calculation and parameter values of the transmittances used in SOLEMI are summarized in Espinar *et al.* (2014). The diffuse part of the clear-sky irradiance $DHI_{cs}$ is summarized from three parts namely Rayleigh scattering, aerosol scattering and multiple reflections between surface and atmosphere. It is described by

$$DHI_{cs} = DHI_r + DHI_a + DHI_m, \tag{10.5}$$

where $DHI_r$ is the diffuse irradiance due to Rayleigh scattering, $DHI_a$ is the diffuse irradiance due to aerosol scattering and $DHI_m$ is the diffuse irradiance due to multiple reflections. Finally, the total clear-sky irradiance $GHI_{cs}$ is calculated by

$$GHI_{cs} = BNI_{cs}\cos(\Theta_z) + DHI_{cs}. \tag{10.6}$$

### 10.1.3 ESRA clear-sky model

In the following, the ESRA clear-sky model used in HC3v4 is briefly described. In the ESRA model the direct component $BHI_{cs}$ and diffuse component $DHI_{cs}$ is determined separately. The direct irradiance on a horizontal plane is given by

$$BHI_{cs} = GHI_{ext} \cos(\Theta_z)\, e^{(-0.8662 \cdot TL(AM2) \cdot m \cdot \delta_R(m))}, \tag{10.7}$$

where $GHI_{ext}$ is the irradiance normal to the solar beam at the top of atmosphere, $\Theta_z$ is the solar zenith angle, $TL(AM2)$ is the Linke turbidity factor for an air mass of 2, $m$ is the relative optical air mass and $\delta_R(m)$ is the integral Rayleigh optical thickness. The values of $TL(AM2)$ are based on a climatology of monthly means of $TL$ proposed by Remund *et al.* (2003). The last term describes the transmittance of the beam irradiance under clear-sky conditions (Rigollier *et al.*, 2000). The diffuse irradiance $DHI_{cs}$ is described by

$$DHI_{cs} = BNI_{ext} T_{rd}(TL(AM2))\, F_d(\Theta_z, TL(AM2)), \tag{10.8}$$

where $T_{rd}$ is the diffuse transmission function at zenith and $F_d$ is the diffuse angular function. $T_{rd}$ is calculated by

$$\begin{aligned} T_{rd}(TL(AM2)) = &-1.584310^{-2} + 3.054310^{-2} TL(AM2) \\ &+3.79710^{-4} (TL(AM2))^2. \end{aligned} \tag{10.9}$$

The diffuse angular function $F_d$ is described by a second order sine polynomial function by

$$F_d(\Theta_z, TL(AM2)) = A_0 + A_1 \cos(\Theta_z) + A_2 (\cos(\Theta_z))^2. \tag{10.10}$$

The unitless coefficients $A_0$, $A_1$ and $A_2$ depend on the Linke turbidity factor. They are given by

$$\begin{aligned} A_0 &= 2.646310^{-1} - 6.158110^{-2} TL(AM2) + 3.140810^{-3} (TL(AM2))^2 \\ A_1 &= 2.0402 + 1.894510^{-2} TL(AM2) - 1.116110^{-2} (TL(AM2))^2 \\ A_2 &= -1.3025 + 3.92310^{-2} TL(AM2) + 8.507910^{-3} (TL(AM2))^2 \end{aligned} \quad . \tag{10.11}$$

The minimum value of $A_0$ should not be below $2 \cdot 10^{-3}$, otherwise it should be set to $2 \cdot 10^{-3} / T_{rd}$. Further details can be found in Rigollier *et al.* (2000) and Geiger *et al.* (2002).

## 10.2 Heliosat-4

The Heliosat-4 method is a radiative-transfer based direct method adapted from an important approximation: the decoupling of clear-sky irradiance calculation and a modification due to cloud properties and ground albedo (Oumbe *et al.*, 2014). This approximation is applied for the solar irradiance at ground surface considering clear-sky irradiances and a modification by clouds and ground albedo. Changes in clear-atmosphere properties have negligible effect on the $kC$ so that both terms can be calculated independently. The maximum errors made in using this approximation (95th percentile) on global and direct surface irradiances are less than $15\,W/m^2$.

The clear-sky index $kC$ (defined in equation 2.9), in the field of UV and photosynthetically active radiation also known as cloud modification factor, and a clear-sky index for beam irradiance $kC_b$ is defined by

$$kC_b = \frac{BHI}{BHI_{cs}}. \tag{10.12}$$

Both $kC$ and $kC_b$ describes the cloud influence on the downwelling radiation and it is expected that both depend on changes of the clear-sky atmosphere properties $p_{cs}$. Therefore, $GHI$ and $BHI$ can be expressed by

$$\begin{aligned} GHI &= GHI_{cs}\left(\Theta_z, \rho_{ground}, p_{cs}\right) kC\left(\Theta_z, \rho_{ground}, p_{cs}, p_{cloud}\right) \\ BHI &= BHI_{cs}\left(\Theta_z, p_{cs}\right) kC_b\left(\Theta_z, p_{cs}, p_{cloud}\right), \end{aligned} \tag{10.13}$$

where $\Theta_z$ is the sun zenith angle calculated with the SG2 algorithm (Blanc and Wald, 2012), $\rho_{ground}$ is the ground albedo and $p_{cs}$ is a variable set describing the optical state of the atmosphere under clear-sky conditions. The included variables are:

1. total column contents in ozone
2. total column contents in water vapour
3. elevation of the ground above mean sea level
4. typical atmospheric profile from the six Air Force Geophysics Laboratory (AFGL) atmospheric profiles defining the vertical profile of temperature, pressure, density, and volume mixing ratio for gases as a function of altitude
5. aerosol optical depth (AOD) at 550 nm
6. Ångström coefficient
7. aerosol type from the Optical Properties of Aerosols and Clouds (OPAC) library (Hess *et al.*, 1998)

The optical state of a cloudy atmosphere is described with variables contained in the parameter set $p_{cloud}$:

1. cloud optical depth
2. cloud phase
3. cloud liquid water content
4. droplet effective radius
5. the vertical position of the cloud

Oumbe *et al.* (2014) has shown that the error made in decoupling the effects of the clear atmosphere from those due to the clouds is negligible because the error is around 2 % and therefore in the uncertainty of accurate pyranometers. Hence, Heliosat-4 uses the following approximations for calculating *GHI* and *BHI* defined by

$$\begin{aligned} GHI &\approx GHI_{cs}\left(\Theta_z, \rho_{ground}, p_{cs}\right) kC\left(\Theta_z, \rho_{ground}, p_{cs0}, p_{cloud}\right) \\ BHI &\approx BHI_{cs}\left(\Theta_z, p_{cs}\right) kC_b\left(\Theta_z, p_{cs0}, p_{cloud}\right) \end{aligned}, \tag{10.14}$$

where $p_{cs0}$ is an arbitrarily chosen but typical set $p_{cs}$. As mentioned before, this approximation leads to an error less than 2 % in the most cases and depends on $\Theta_z$, the $\rho_{ground}$ and the cloud optical depth (Oumbe *et al.*, 2014).

Heliosat-4 uses two different irradiance models to realize the decoupling approach mentioned before: McClear and McCloud. McClear is a new irradiance model calculating the downwelling solar irradiances under clear-sky conditions using physical relations pre-calculated with libRadtran and stored in look-up tables (LUT, see Section 10.2.1). This leads to calculation time savings compared to other radiative transfer models. The McCloud model calculates the clear-sky indices for global and beam irradiance under cloudy conditions taking into account cloud properties (see Section 10.2.3). These required cloud properties as well as the position of clouds are also derived from satellite data provided by the AVHRR Processing scheme Over cLouds, Land and Ocean (APOLLO Kriebel *et al.*, 2003, see Section 10.2.2).

The combination and interaction of these models as well as the input data are shown in figure 10.2. The APOLLO model calculates the cloud mask from multispectral satellite images. This cloud mask decides if McCloud is applied. If clouds are detected, McCloud calculates the *kC* values and multiply them by the clear-sky irradiance from McClear. Otherwise, only the clear-sky irradiance from McClear is used.

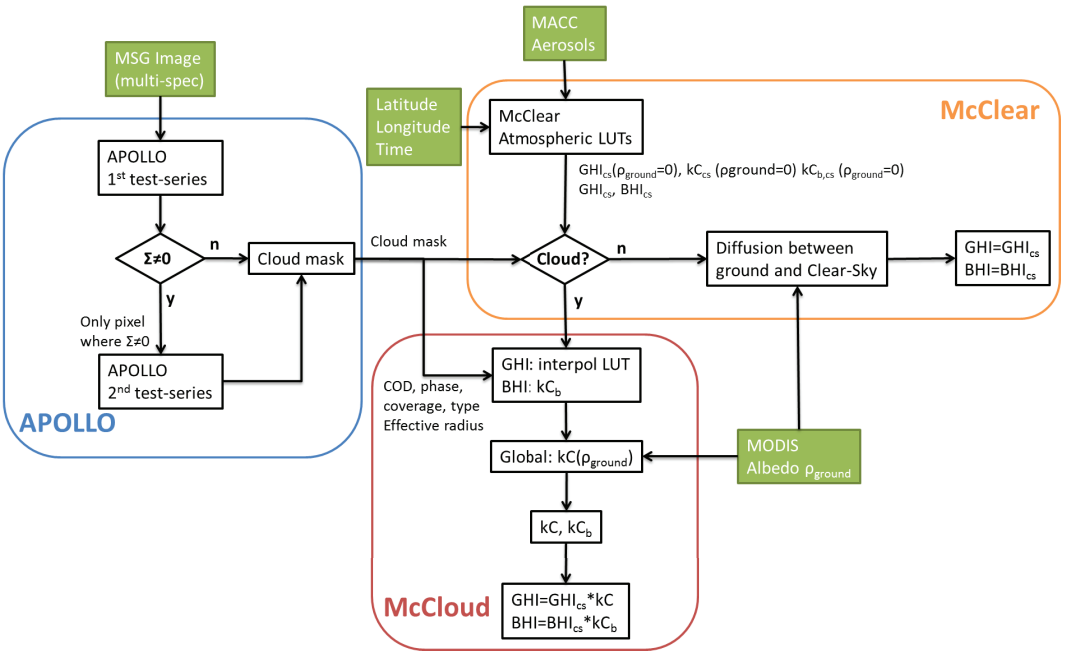


Figure 10.2: Brief overview about the Heliosat-4 method.

### 10.2.1 McClear clear-sky model

Lefèvre *et al.* (2013) developed the new fast McClear clear-sky model to estimate the downwelling shortwave direct and global irradiances received at ground level. It is based on full physical modelling instead of empirical relations or simplifications. The atmosphere description parameters e.g. aerosol properties or total column content in water vapour and ozone are delivered by the MACC projects (Espinar *et al.*, 2014). McClear estimates the irradiance at ground level with the similar accuracy as the radiative transfer model libRadtran (Mayer and Kylling, 2005) but 105 times faster due to using look-up tables and interpolation functions (Espinar *et al.*, 2014).

The LUT decrease the calculation time and contain the clearness-indices for global and direct irradiances. The beam irradiance clearness-index $kT_b$ is defined by

$$kT_b = \frac{BHI}{G_{ext}}. \tag{10.15}$$

The $kT$ LUTs were calculated for $\rho_{ground}$ 0, 0.1 and 0.9 and $kT_b$ also for $\rho_{ground}$=0 as well as several variations of the atmosphere parameter set $p_{cs}$. For values between the pre-calculated LUT-values linear interpolation and extrapolation functions are used except for $\Theta_z$. The calculation of a $kT$ for a given $\rho_{ground}$ is described by the formula of Vermote *et al.* (1997) as a function of $\rho_{ground}$ and the atmospheric

spherical albedo $\rho_{sphere}$ by

$$kT\left(\rho_{ground}\right) = \frac{kT\left(\rho_{ground}=0\right)}{1-\rho_{ground}\rho_{sphere}}. \tag{10.16}$$

The estimation of $\rho_{sphere}$ is performed by computing two given values of $\rho_{ground}$ (0.1, and 0.9) and afterwards linear interpolation or extrapolation by

$$\begin{aligned} a &= \frac{\rho_{sphere}\left(\rho_{ground}=0.9\right)-\rho_{sphere}\left(\rho_{ground}=0.1\right)}{0.8} \\ b &= \rho_{sphere}\left(\rho_{ground}=0.1\right)-0.1a \\ \rho_{sphere} &= a\rho_{ground}+b \end{aligned} \quad . \tag{10.17}$$

Contrary to Heliosat-2, in Heliosat-4 the ground albedo values are provided by MODIS satellite images (product MCD43C1) with a spatial resolution projected to a 0.05 grid in latitude/longitude and a 16 day acquisition time. These data form a monthly mean climatology (Blanc *et al.*, 2014b). The data sets contain three model parameters for the description of the bidirectional reflectance distribution function (BRDF) and are taken from the closest data grid point. The approach towards missing data in the two different MODIS data sets is described in detail in Lefèvre *et al.* (2013). Based on BRDF two further parameters are calculated, the directional hemispherical reflectance (DHR, also known as black-sky albedo) and the bihemispherical reflectance (BHR, also known as white-sky albedo) (Schaaf *et al.*, 2002). Defining $k_b\left(\rho_{ground}\right)$ by

$$k_b\left(\rho_{ground}\right) = \frac{BHI}{GHI\left(\rho_{ground}\right)}. \tag{10.18}$$

Herein, $BHI$ is independent from $\rho_{ground}$ while $\rho_{ground}$ is described by

$$\rho_{ground} = BHR + k_b\left(\rho_{ground}\right)\cdot\left(DHR-BHR\right). \tag{10.19}$$

In this formula the dependence on $\rho_{ground}$ to $k_b$, which depends itself on $\rho_{ground}$ is challenging. The combination of the equations 10.16 to 10.19 leads to a second-order equation in which $kT$ is the value of interest. It is given by

$$\begin{aligned} &a(DHR-BHR)^2kT_b^2 \\ &+kT\left[kT\left(\rho_{ground}=0\right)+\left(2aBHR+b\right)\left(DHR-BHR\right)kT_b\right] \\ &+\left(aBHR^2+bBHR-1\right)kT^2=0 \end{aligned} \quad . \tag{10.20}$$

Lefèvre *et al.* (2013) uses Monte Carlo technique to solve equation 10.20 and found

that only one solution is respects the constraint $kT > kT_b$. Therefore $kT$ is estimated by using equation 10.20 while equation 10.19 provides $\rho_{ground}$. McClear requires a vertical atmospheric profile which is taken from the implemented ones in libRadtran. There are five vertical atmospheric profile used in McClear based on the AFGL: tropics, mid-latitude summer and winter, and sub-Arctic summer and winter. The selection of the vertical atmospheric profile depending on the location based on a map derived from the one proposed by Trewartha (1954). The winter season is defined from November to April and during this season the winter profiles are chosen for mid-latitude and sub-Arctic locations. The altitude correction is performed by linear interpolation considering the elevation values provided by MACC.

The aerosol inputs for McClear are provided by European Centre for Medium-Range Weather Forecasts (ECMWF) in the framework of the FP7 and H2020 projects MACC. The model is MACC-IFS-NRT and the product description could be found online[1]. Besides the AOD at 550 nm and 1240 nm, partial optical depth at 550 nm for dust, organic particles, sea salt, sulphate and black carbon are delivered. Both AODs are used for the calculation of the Ångström coefficient. The five partial optical depths are used to determine the corresponding aerosol types within the nine typical aerosol types of the library OPAC: urban, continental clean, continental polluted, continental average, maritime clean, maritime polluted, maritime tropical, antarctic, and desert. The conversion algorithm into these more detailed ensembles is given in figure 1 of Lefèvre *et al.* (2013). McClear provides as output data the clear-sky irradiances $GHI_{cs}$ and $BHI_{cs}$ for a site considering the original $\rho_{ground}$ as well as $GHI_{cs}$ ($\rho_{ground}$=0), $GHI_{cs}$ ($\rho_{ground}$=0.1) and $GHI_{cs}$ ($\rho_{ground}$=0.9).

The validation was performed against 1-minute average clear-sky ground measurements provided from several station of the Baseline Surface Radiation Network in various climates. For *GHI* the *CC* ranges from 0.95 to 0.99, the *ME* from $-14\,\mathrm{W/m^2}$ to $25\,\mathrm{W/m^2}$ and the *RMSE* from $20\,\mathrm{W/m^2}$ (3 % of the mean observed irradiance) to $36\,\mathrm{W/m^2}$ (5 %). For *BHI* the *CC* ranges from 0.86 to 0.99, *ME* from $-49\,\mathrm{W/m^2}$ to $+33\,\mathrm{W/m^2}$ and *RMSE* from $33\,\mathrm{W/m^2}$ (5 %) to $64\,\mathrm{W/m^2}$ (10 %), (Lefèvre *et al.*, 2013). Other publications on validating McClear exist on desert regions namely Abu Dhabi (Eissa *et al.*, 2015a) and Egypt (Eissa *et al.*, 2015b).

[1] `https://www.gmes-atmosphere.eu/catalogue/#details?st=Airqualityandatmosphericcomposition&pp=Aerosol&sp=TotalAOD&pr=MACC-IFSNRTforecastofglobaltotalaerosolopticaldepthatmultiplewavelengths&op=DETAILS`

### 10.2.2 APOLLO cloud detection scheme

APOLLO stands for AVHRR Processing scheme Over cLouds, Land and Ocean and was originally developed for the AVHRR (Advanced Very High Resolution Radiometer) sensors of the polar orbiting NOAA (National Oceanic and Atmospheric Administration) satellites (Saunders and Kriebel, 1988; Kriebel *et al.*, 2003). The objective of APOLLO is the estimation of cloud properties using several spectral channels of the radiometers.

Kriebel *et al.* (2003) describes the cloud detection using a two-stage approach with various tests. The first stage separates cloud-free and cloud contaminated pixels taking into account the reflectance and infrared-derived temperature values of the image pixels. If a pixel is brighter than a reflectance threshold or colder than a temperature threshold it is marked as cloudy. The dynamic visible threshold test uses two visible spectral channels and calculates the ratio between these two channels. Normally, the ratio of a pixel showing vegetated land surface is higher than that of cloudy pixels while the ratio over ocean surface is lower. However, the ratio of non-vegetated land surface is similar to that of clouds and it is hard to distinguish between both. The infrared gross temperature test compares temperatures with a threshold. Pixels with a temperature lower than a minimum threshold are marked as cloudy. Furthermore, the temperature difference between the two infrared channels is low in cloud-free situations and over thick clouds but increases over thin clouds. The last test in this series, applied only over ocean surface, calculates the standard deviation of a 3x3 pixel window around each pixel and is denoted as spatial coherence. The threshold setting is difficult because of the high variability and is solved by dynamical thresholds based on window histograms.

The second stage is only used for pixels indicated as cloud contaminated. This stage divides the pixels into fully and partially clouded. This is performed by a second run of two above-mentioned tests with other thresholds: the spatial coherence and the dynamic ratio. Afterwards, all pixels are analysed to identify snow or ice surface pixels to avoid misleading cloud identifications. The analysis thresholds of the different tests based on self-adjusting histogram techniques reduce satellite and sensor-related problems (Kriebel *et al.*, 2003).

APOLLO was adapted by DLR to process images of the SEVIRI (Spinning Enhanced Visible and Infrared Imager) instrument aboard the series of Meteosat Second Generation (MSG) satellites. According to Schroedter Homscheidt *et al.* (2004) the adaption compromises the thresholds for most APOLLO algorithms. While the self-adjusting histogram limits based on values in neighbourhood-boxes are still valid, the explicit parameters and all default values are changed. Furthermore, the

APOLLO processing contains corrections for regional peculiarities. The peculiarities can lead to misclassification and misidentification of cloud properties. These corrections depend not only on the regions with peculiarities but also on the experience to handle it. Therefore, the correction schemes are different the regions as well as to the both sensors, AVHRR and SEVIRI. The validation of the adaption was performed by comparing typical cloud parameter values from APOLLO using AVHRR and APOLLO using SEVIRI.

Independent of the used implementation and sensor, APOLLO provides following data to each image pixel

1. a mask cloud-free/cloudy
2. cloud optical depth $\tau_c$
3. cloud type (low, medium, high, thin)
4. cloud coverage, i.e. the fraction of a pixel covered by a cloud

The calculation of the cloud coverage of partly clouded pixels takes into account the reflectance measured at $0.6\,\mu$m and $0.8\,\mu$m as well as the average reflectance of fully-clouded and cloud-free pixels. This is performed in a 59 x 59 pixel window centered on the concerned pixel. Afterwards, the effective optical depth is estimated taking the average of all $\tau_c$ of fully covered pixels of same type within the window. This average is multiplied by the cloud coverage. Furthermore, some thresholds are used for $\tau_c$. The minimum value of $\tau_c$ is 0.5 for fully clouded pixels and 0.45 for partly clouded pixels. Values below this threshold are set to this threshold. The maximum of $\tau_c$ is set at 500 (Wald, 2014).

### 10.2.3 McCloud cloudy-sky model

The objective of the McCloud model is the determination of $kC$ and $kC_b$ under cloudy conditions and modifies $GHI_{cs}$ and $BHI_{cs}$ provided by the McClear model. As inputs McCloud uses the clear-sky irradiances $GHI_{cs}$ and $BHI_{cs}$, cloud properties, namely $\tau_c$, the cloud type and the sun zenith angle $\Theta_z$ as well as ground albedo $\rho_{ground}$. Within McCloud, the clear-sky index for direct radiation $kC_b$ is estimated taking into account the cloud optical depth $\tau_c$ provided by APOLLO by

$$kC_b = e^{\left(-\frac{\tau_c}{\cos(\Theta_z)}\right)}. \tag{10.21}$$

Similarly to McClear, the $kC$ estimation is also based on look-up tables and interpolation techniques. The vertical position and the geometrical thickness of the clouds

have just a small effect on the global radiation, therefore, typical altitudes of clouds can be used instead of localized values (Espinar *et al.*, 2014). Therefore, the following cloud base height and optical thickness are chosen for the four cloud types provided by APOLLO:

- low cloud: water cloud at low altitude. The cloud base height is 1.5 km and the geometrical thickness is 1 km
- medium cloud: water cloud at medium altitude. The cloud base height is 4 km with a thickness of 2 km
- high cloud: water cloud of large vertical extent from low altitude to medium altitude. The cloud base height is 2 km and the thickness is 6 km
- thin ice cloud: ice cloud with a base height of 9 km and a geometrical thickness of 0.5 km

McCloud calculates *kC* using interpolations between nodes on the LUT for each cloud type. Each LUT contains the results from libRadtran using different values for $\Theta_z$, $\tau_c$, $\rho_{ground}$ and a typical set $p_{cs0}$. Following the decoupling approach, *kC* can be determined under cloudy conditions considering a typical set of atmospheric parameters $p_{cs0}$ (Oumbe *et al.*, 2014). The difference in *kC* using different $p_{cs0}$ is negligible according to Wald (2014). The LUTs are linearly interpolated taking into account $\Theta_z$ and $\tau_c$ while the interpolation of $\rho_{ground}$ is more complex, similar to McClear, and results in three values of *kC*, one for each $\rho_{ground} = 0$, 0.1, and 0.9. *GHI* is computed for each of the three $\rho_{ground}$ taking into account the corresponding $GHI_{cs}$ provided by McClear by

$$GHI\left(\Theta_z, \rho_{ground}, p_{cs0}, p_{cloud}\right) = GHI_{cs}\left(\Theta_z, \rho_{ground}, p_{cs0}\right) kC\left(\Theta_z, \rho_{ground}, p_{cs0}, p_{cloud}\right). \tag{10.22}$$

The computation of $\rho_{ground}$ follows the same approach as in McClear, as described before. The clearness index, defined in equation 2.8, is also calculated by the formula of Vermote *et al.* (1997) by

$$kT\left(\rho_{ground}\right) = \frac{kT\left(\rho_{ground} = 0\right)}{1 - \rho_{ground}\rho_{sphere,cloud}}. \tag{10.23}$$

Similarly to McClear, the spherical albedo of the cloudy atmosphere $\rho_{sphere,cloud}$ is determined considering $\rho_{ground}$. The ground albedo $\rho_{ground}$ is computed in the same way as in Lefèvre *et al.* (2013). Equation 10.24 is used calculating $\rho_{sphere,cloud}$ for two $\rho_{ground}$ (0.1 and 0.9) and then linearly interpolated or extrapolated for the actual

$\rho_{ground}$ by

$$\begin{aligned}
\rho_{sphere,cloud}\left(\rho_{ground}=0.1\right) &= \frac{1-\frac{GHI\left(\rho_{ground}=0\right)}{GHI\left(\rho_{ground}=0.1\right)}}{0.1} \\
\rho_{sphere,cloud}\left(\rho_{ground}=0.9\right) &= \frac{1-\frac{GHI\left(\rho_{ground}=0\right)}{GHI\left(\rho_{ground}=0.9\right)}}{0.9} \\
a &= \frac{\rho_{sphere,cloud}\left(\rho_{ground}=0.9\right)-\rho_{sphere,cloud}\left(\rho_{ground}=0.1\right)}{0.8} \\
b &= \rho_{sphere,cloud}\left(\rho_{ground}=0.1\right)-0.1a \\
\rho_{sphere,cloud} &= a\rho_{ground}+b
\end{aligned} \quad . \tag{10.24}$$

Finally, according to Wald (2014), *GHI* is calculated with *GHI* ($\rho_{ground}$=0) by

$$\begin{aligned}
GHI\left(\Theta_z,\rho_{ground},p_{cs},p_{cloud}\right) &= \frac{GHI\left(\rho_{ground}=0\right)}{1-\rho_{ground}\rho_{sphere,cloud}} \\
&= \frac{GHI_{cs}\left(\Theta_z,\rho_{ground}=0,p_{cs}\right)kC\left(\Theta_z,\rho_{ground}=0,p_{cs0},p_{cloud}\right)}{1-\rho_{ground}\rho_{sphere,cloud}}
\end{aligned} \quad . \tag{10.25}$$

A detailed overview of Heliosat-4 is shown in Figure 10.3. It illustrates the different input values and sources (green boxes) and the various test series within APOLLO leading to the decision on whether a pixel is cloud free or cloudy (Kriebel *et al.*, 2003). The outcome from the cloud product is used as trigger for using McCloud as well as input for McCloud. The calculation steps of both McClear and McCloud are included according to Qu (2013).

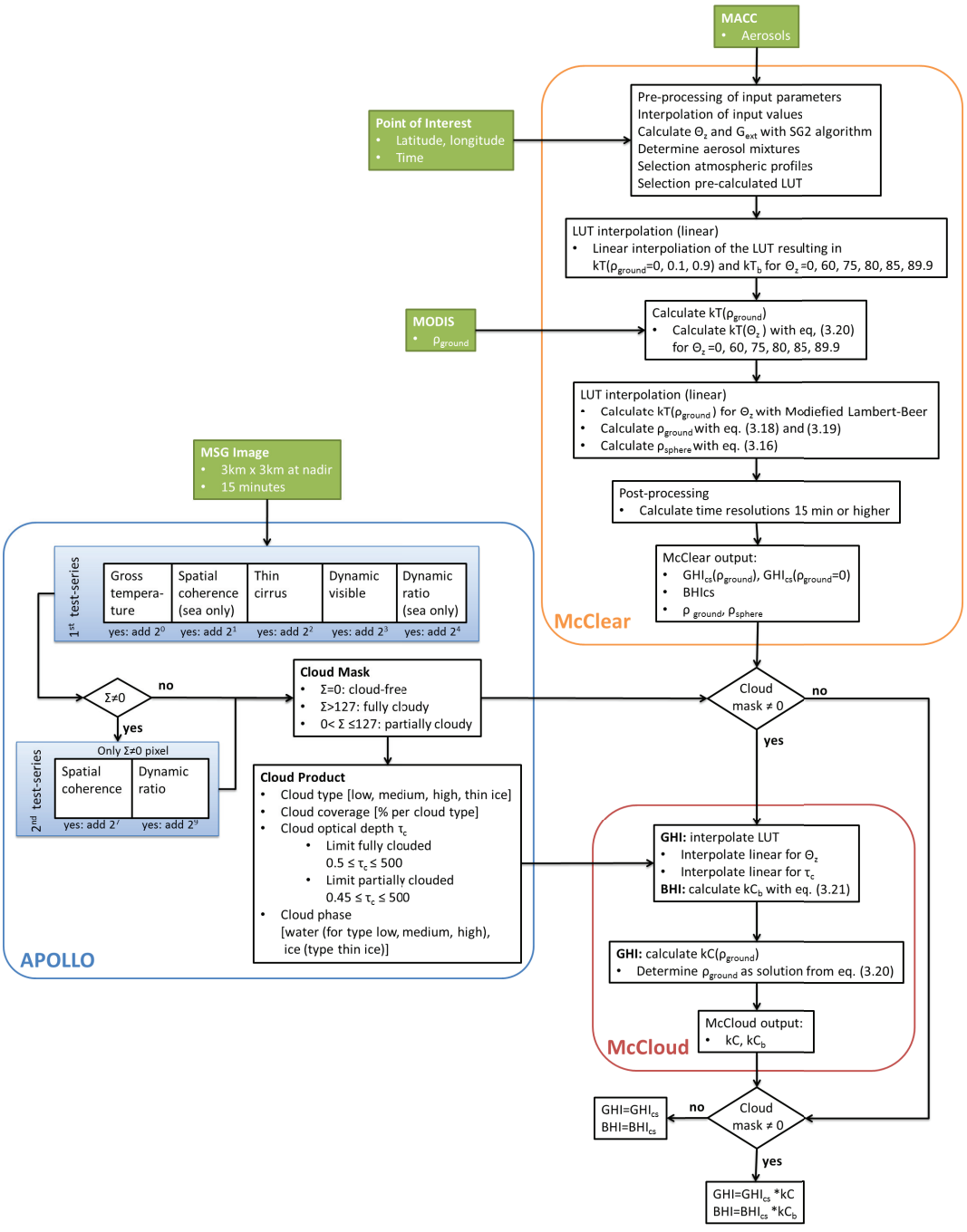


Figure 10.3: The overall scheme of Heliosat-4 is based on the different models McClear, APOLLO and McCloud. The detailed algorithms of McClear and McCloud are visualized according to Qu (2013) and APOLLO according to Kriebel *et al.* (2003), respectively.

# Chapter 11

# Appendix C: List of papers, posters and oral presentations

- Ruf, H., Schroedter-Homscheidt, M., Heilscher, G. and Beyer, H. G. (2016), 'Quantifying residential PV feed-in power in low voltage grids based on satellite-derived irradiance data with application to power flow calculations', in *Solar Energy*, vol. 135, pp. 692-702, 2016

- Ditz, K., Ruf, H., Funk, D., Schroedter-Homscheidt, M., Köhler, C. and Heilscher, G. (2016), 'Validierung satellitenbasierter solarer Einstrahlung nach dem Heliosat-4-Verfahren in Deutschland, in *Proceedings of the 31. Symposium Photovoltaische Solarenergie*, Bad Staffelstein, Germany

- Ruf, H., Kober, P., Meier, F., Irlbeck, M. and Heilscher, G. (2016), 'Vergleich des synthetischen Referenzlastprofils nach VDI 4655 mit hochaufgelsten Messdaten eines modernen Hauses in Ulm, in *Proceedings of the 31. Symposium Photovoltaische Solarenergie*, Bad Staffelstein, Germany

- Ruf, H., Schroedter-Homscheidt, M., Meier, F., Heilscher, G. and Beyer, H. G. (2016), 'Bestimmung der Wirkleistung an einem Transformator in einem Niederspannungsnetz mit hohem Anteil an Photovoltaik-Anlagen mit Hilfe von Satelliten-Einstrahlungsdaten, in *Proceedings of the 31. Symposium Photovoltaische Solarenergie*, Bad Staffelstein, Germany

- Irlbeck, M., Ruf, H. and Köhler, C. (2016), 'Die Digitalisierung des Stromsystems durch Vorhersagesysteme: Eine gesamtsystemische Betrachtung mittels Referenzarchitekturen, in *Proceedings of the 31. Symposium Photovoltaische Solarenergie*, Bad Staffelstein, Germany

- Ruf, H., Kober, P., Meier, F., Irlbeck, M. and Heilscher, G. (2016), 'Reprsentativitt des Projekthauses Ulm: Vergleich der Messdaten mit der VDI 4655, in *Proceedings of the 3rd Conference Zuknftige Stromnetze fr Erneuerbare Energien*, Berlin, Germany

- Ruf, H., Schroedter-Homscheidt, M., Meier, F., Heilscher, G. and Beyer, H. G. (2016), 'Nutzung von satellitenbasierten Einstrahlungsdaten zur Lastflussberechnung in Niederspannungsnetzen mit hohem Anteil an Photovoltaik-Anlagen, in *Proceedings of the 3rd Conference Zuknftige Stromnetze fr Erneuerbare Energien*, Berlin, Germany

- Ruf, H., Schroedter-Homscheidt, M., Beyer, H. G. and Heilscher, G. (2015), 'Load Flow Calculation of a Low Voltage Transformer using Satellite-based Irradiance Data, in *Proceedings of the International ETG Congress 2015: Die Energiewende*, Bonn, Germany

- Stakic, D., Ebe, F., Ruf, H., Meier, F. and Heilscher, G. (2015), 'Simulation of the life-time consumption from oil-immersed transformers with consideration of the further development of decentralized PV feed-in', in *Proceedings of the International ETG Congress 2015: Die Energiewende*, Bonn, Germany

- Ruf, H., Stakic, D., Funk, D., Ditz, K., Heilscher, G., Meier, F. and Schroedter-Homscheidt, M., (2015), 'ICT control strategies for high PV penetration at the demo site in Ulm', presentation at *Sustainable Places 2015*, Savona, Italy

- Ruf, H., Heilscher, G., Meier, F. and Schroedter-Homscheidt, M., (2015), 'Using satellite data for power flow estimation of an electrical low voltage grid with a high amount of photovoltaic systems', presentation at *3rd International Conference Energy & Meteorology (ICEM)*, Boulder, Colorado, USA

- Ditz, K., Ruf, H., Funk, D., Schroedter-Homscheidt, M., Meier, F., Krishnaraju, S. and Heilscher, G. (2015), 'Ergebnisvergleich von PV- und Netz-Simulationen für die Bestimmung der Einspeiseleistung', in *Proceedings of the 30. Symposium Photovoltaische Solarenergie*, Bad Staffelstein, Germany

- Funk, D., Ruf, H., Meier, F., Ebe, F. and Heilscher, G. (2015), 'Belastung durch dezentrale Photovoltaikanlagen in Niederspannungsnetzen', in *Proceedings of the 30. Symposium Photovoltaische Solarenergie*, Bad Staffelstein, Germany

- Köhler, C., Ruf, H., Steiner, A., Lee, D., Thieler, J., Casel, M., Funk, D., Ditz, K., Stakic, D., Ebe, F., Meier, F., Wosnitza, M., Ritter, B. and Heilscher, G. (2015), 'Nutzung Numerischer Wettervorhersagen in der Simulation von Verteilnetzen: Die Effekte einer Sonnenfinsternis auf netzgekoppelte PV-Anlagen und Netztransformatoren', in *Proceedings of the 30. Symposium Photovoltaische Solarenergie*, Bad Staffelstein, Germany

- Ruf, H., Funk, D., Meier, F. and Heilscher, G. (2015), 'Bestimmung von Ausrichtungs- und Neigungswinkeln von Bestandsanlagen mittels LIDAR Daten', in *Proceedings of the 30. Symposium Photovoltaische Solarenergie*, Bad Staffelstein, Germany

- Stakic, D., Ebe, F., Ruf, H., Meier, F. and Heilscher, G. (2015), 'Simulation des Lebensdauerverbrauchs von ölbefüllten Verteilnetztransformatoren unter Berücksichtigung des weiteren Ausbaus dezentraler Photovoltaikeinspeisung', in *Proceedings of the 30. Symposium Photovoltaische Solarenergie*, Bad Staffelstein, Germany

- Ditz, K., Ruf, H., Funk, D., Schroedter-Homscheidt, M., Meier, F., Krishnaraju, S. and Heilscher, G. (2015), 'Vergleich von PV- und Netzsimulationswerkzeugen zur Unterstützung der Netzbetriebsführung im Verteilnetz', in *Proceedings of the 2nd Conference Zukünftige Stromnetze für Erneuerbare Energien*, Berlin, Germany

- Ruf, H., Funk, D., Ditz, K., Stakic, D., Kaufmann, T., Heilscher, G., Schroedter-Homscheidt, M., Meier, F. and Ebe, F. (2014), 'Transformer load flow calculation using satellite derived irradiance', poster at *COST WIRE Final Workshop*, Paris, France

- Ruf, H., Schroedter Homscheidt, M., Meier, F. and Heilscher, G. (2014), 'Application of meteorological data for state estimation of an electrical low voltage grid with a high amount of photovoltaic systems', presentation at *14th EMS Annual Meeting & 10th European Conference on Applied Climatology (ECAC)*, Prague, Czech

- Huld, T., Ruf, H. and Heilscher, G. (2014), 'Self-Consumption of Electricity by Households, Effects of PV System Size and Battery Storage', in *Proceedings of the 29th European PV Solar Energy Conference and Exhibition*, Amsterdam, The Netherlands

- Weiss, I., Caneva, S., Arancon, S., Heilscher, G., Ruf, H., Stakic, D., Ditz, K., Funke, D., Neuchel, E., Meier, F., Schwabeneder, D., Brunner, H., Sawsan, H., Basciotti, D., Schmidt, R., Schroedter-Homscheidt, M., Killius, N., Borg, E., Schülke, A., Schwarz, M., Venturi, A., Papageorgiou, A., Pettersson, J., Ahlund, C., Saguna, S., Idowu, S., Nyberg, S. and Sjoo, J. (2014), 'How to Optimise the Over Production of PV Electricity into the Grid with the Implementation of ICT Devices The OrPHEuS Project', in *Proceedings of the 29th European PV Solar Energy Conference and Exhibition*, Amsterdam, The Netherlands

- Ruf, H., Kaufmann, T., Ditz, K., Funk, D., Stakic, D., Heilscher, G., Meier, F. and Ebe, F. (2014), 'Smart Grid Ulm: Netzanalyse - Netzplanung - Netzbetrieb', poster at *Smart Grids Week 2014* Graz, Austria

- Ruf, H., Schroedter-Homscheidt, M., Meier, F. and Heilscher, G. (2014), 'Calculate electrical values of distribution grid with high PV shares using satellite and GIS data', presentation at *COST WIRE and CITIES Workshop: Weather Intelligence for Renewable Urban Areas*, Roskilde, Denmark

- Ruf, H., Schroedter-Homscheidt, M., Meier, F. and Heilscher, G. (2014), 'Satellite-based Nowcasting for Distribution Grids', presentation at the *Geospatial World Forum 2014*, Geneva, Switzerland

- Ditz, K., Ruf, H., Heilscher, G., Ebe, F., Meier, F., Danzer, M. A., Felder, M., Sehnke, F., Schott, B. and Binder, J. (2014), 'Alternative zum Netzausbau durch vorausschauende Netzplanung und -Optimierung, Entwicklungen im Smart Grid', in *Proceedings of the 29. Symposium Photovoltaische Solarenergie*, Bad Staffelstein, Germany

- Funk, D., Ruf, H., Meier, F. and Heilscher, G. (2014), 'Einfluss verschiedener Modultechnologien auf ein Niederspannungsnetz', in *Proceedings of the 29. Symposium Photovoltaische Solarenergie*, Bad Staffelstein, Germany

- Heilscher, G., Correa, H. A. A., Ebe, F., Kaufmann, T., Ruf, H., Müller, R. and Meier, F. (2014), 'Qualifizierung der Netzspannungsinformation von Wechselrichtern für die Beurteilung des Netzzustands von Niederspannungsnetzen', in *Proceedings of the 29. Symposium Photovoltaische Solarenergie*, Bad Staffelstein, Germany

- Ruf, H., Schroedter-Homscheidt, M., Beyer, H. G., Meier, F. and Heilscher, G. (2014), 'Wolkenindikatoren für die Sammelschienenspannung von Nieder-

spannungsverteilnetztransformatoren', in *Proceedings of the 29. Symposium Photovoltaische Solarenergie*, Bad Staffelstein, Germany

- Stakic, D., Ebe, F., Ruf, H., Meier, F., Müller, M. and Heilscher, G. (2014), 'Implementierung photovoltaischer Systeme in elektrische Netze von Industriegebieten', in *Proceedings of the 29. Symposium Photovoltaische Solarenergie*, Bad Staffelstein, Germany

- Ditz, K., Ruf, H., Heilscher, G., Ebe, F., Meier, F., Danzer, M., Felder, M., Sehnke, F., Schott, B. and Binder, J. (2014), 'Varianten des Netzausbaus durch vorausschauende Netzplanung und optimierung Entwicklungen im Smart Grid Testgebiet Hittistetten', in *Proceedings of the Conference Zukünftige Stromnetze für Erneuerbare Energien*, Berlin, Germany

- Ruf, H., Schroedter-Homscheidt, M., Beyer, H. G., Meier, F. and Heilscher, G. (2013), 'Investigation of cloud indicators for low voltage distribution grid transformers', presentation at *IEA-PVPS Task 14 & IEA-SHC Task 46 Workshop: Solar Ressource and Forecast Data for High PV Penetration*, Paris, France

- Ruf, H., Schroedter-Homscheidt, M., Beyer, H. G., Meier, F. and Heilscher, G. (2013), 'Analysis of Cloud Indicators to Derive the Bus Bar Voltage at a Local Low Voltage Distribution Grid Transformer', in *Proceedings of the 28th European Photovoltaic Solar Energy Conference and Exhibition*, Paris, France

- Meier, F., Ruf, H. and Heilscher, G. (2013), 'Smart Grid Forschung am realen Verteilnetz', presentation at *7. Eurosolar-Konferenz: Stadtwerke mit Erneuerbaren Energien*, Ulm, Germany

- Ruf, H., Schroedter-Homscheidt, M., Beyer, H. G., Meier, F. and Heilscher, G. (2013), 'Wolkenindikatoren für den Photovoltaik-Einfluss auf die Spannung eines Ortsnetstransformators', presentation at *3. Fachtagung Energiemeteorologie*, Grainau, Germany

- Ruf, H., Meier, F. and Heilscher, G. (2013), 'Ausblick auf 100% Strom aus Photovoltaik in Ulm', presentation at *Smart Grids Week 2013*, Salzburg, Austria

- Ebe, F., Fucker, M., Ruf, H., Meier, F. and Heilscher, G. (2013), 'Regelbare Ortsnetztransformatoren (RONT)', in *Proceedings of the 28. Symposium Photovoltaische Solarenergie*, Bad Staffelstein, Germany

- Ruf, H., Heilscher, G., Schroedter-Homscheidt, M., Beyer, H. G. and Meier, F. (2013), 'Erstellung einer Wolkenstatistik für lokale Verteilnetze: Lassen sich einfache Indikatoren für den Einfluss des Wolkenzugs ableiten?', in *Proceedings of the 28. Symposium Photovoltaische Solarenergie*, Bad Staffelstein, Germany

- Schäfer, S., Heilscher, G., Ruf, H. and Meier, F. (2013), 'Auswertungen von Wirkleistungssprüngen an einem Niederspannungstransformator mit PV-Einspeisung', in *Proceedings of the 28. Symposium Photovoltaische Solarenergie*, Bad Staffelstein, Germany

- Ruf, H., Heilscher, G. and Meier, F. (2012), 'Smart Solar Grid - Integration hoher Anteile von Photovoltaik in kommunalen Niederspannungsverteilnetzen', in *Proceedings of the VDE ETG Kongress 2012 - Smart Grid: Intelligente Energieversorgung der Zukunft*, Stuttgart, Germany

- Ruf, H., Heilscher, G., Meier, F., Mayer, O. and Grottke, M. (2012), 'Impact of Increasing Photovoltaic Energy Penetration on the Distribution Grid', in *Proceedings of the 27th European Photovoltaic Solar Energy Conference*, Frankfurt a. M, Germany

- Ruf, H., Stetter, D., Lanig, S., Hoyer-Klick, C., Meier, F. and Heilscher, G. (2012), 'Active Grid Planning Based on Solar Power Roof Potential Analysis', in *Proceedings of the 27th European Photovoltaic Solar Energy Conference*, Frankfurt a. M, Germany

- Ruf, H. (2012), 'Netzintegration von PV: ENDORSE - Entwicklung einer Solarleistungsvorhersage auf Satellitenbasis für die Netzbetreiber', presentation at *Smart Grids Week 2012*, Bregenz, Austria

- Ruf, H. (2012), 'Solardachkataster Ulm', presentation at *Ideenwerkstatt zur regionalen Energiewende*, Ulm, Germany

- Gutnik, J., Heilscher, G. and Ruf, H. (2012), 'Langzeitdegradation kristalliner und amorpher Si-Module und Vergleich mit neueren Modulen', in *Proceedings of the 27. Symposium Photovoltaische Solarenergie*, Bad Staffelstein, Germany

- Ruf, H., Heilscher, G. and Meier, F. (2012), 'Smart Solar Grid: Ergebnisse der Analyse und des Solardachpotentials des ersten Testgebiets der Stadtwerke Ulm', in *Proceedings of the 27. Symposium Photovoltaische Solarenergie*, Bad Staffelstein, Germany

- Ruf, H. (2012), 'Measured effects of a high PV penetration to a communal low voltage grid of Ulm', presentation at *2nd Inverter and PV System Technology Forum 2012*, Berlin, Germany

- Heilscher, G., Ruf, H., Mayer, O., Grottke, M. and Rabe, W. (2011), 'Protection of the System Management at High Penetration of Photovoltaic Energy in the Low Voltage Grid', in *Proceedings of the 26th European Photovoltaic Solar Energy Conference*, Hamburg, Germany

- Ruf, H. (2011), '50% Solarstrom von den Dächern der Stadt Ulm', presentation at *9. Österreichische Photovoltaik Tagung*, Wien, Austria

- Ruf, H. (2011), 'Einbindung von Photovoltaik in das Niederspannungsnetz aus Sicht eines Stadtwerks', presentation at *2. Fachtagung Energiemeteorologie*, Bremerhaven, Germany

- Heilscher, G., Ehleuter, F. and Ruf, H. (2011), 'Technische und wirtschaftliche Bewertung einer Solarmodul-Waschanalage', in *Proceedings of the 26. Symposium Photovoltaische Solarenergie*, Bad Staffelstein, Germany

# REFERENCES


Albrecht, W. and Schröder, W. (2013). *Ausführungshandbuch für Photovoltaik-Anlagen: Normengerechte Planung, Montage, Installation, Inbetriebnahme und Wartung*. Forum Verlag, Merching, March 2013 edition.

ARegV (2007). Verordnung über die Anreizregulierung der Energieversorgungsnetze: ARegV.

ASTM (2012). Tables for Reference Solar Spectral Irradiances: Direct Normal and Hemispherical on 37 Tilted Surface. `http://www.astm.org/Standards/G173.htm`. Viewed 5 April 2015.

Bärwaldt, G. and Kurrat, M. (2008). Auswirkungen von dynamischen Haushaltsstromtarifen auf der Basis stochastischer Haushaltslastprofile. In *Proceedings of the 10. Symposium Energieinnovation*, Graz.

BDEW (2014). Stromnetz in Deutschland. `https://www.bdew.de/internet.nsf/id/DE_Energiedaten`. Viewed 24 April 2015.

Bendib, B., Belmili, H., and Krim, F. (2015). A survey of the most used mppt methods: Conventional and advanced algorithms applied for photovoltaic systems. *Renewable and Sustainable Energy Reviews*, **45**, 637–648.

Beyer, H. G., Costanzo, C., and Heinemann, D. (1996). Modifications of the Heliosat procedure for irradiance estimates from satellite images. *Solar Energy*, **56**(3), 207–212.

Beyer, H. G., Betcke, J., Drews, A., Heinemann, D., Lorenz, E., Heilscher, G., and Bofinger, S. (2004). Identification of a general model for the MPP performance of PV-modules for the application in a procedure for the performance check of grid connected systems. In *Proceedings of the Nineteenth European Photovoltaic Solar Energy Conference*, pages 3073–3076, Paris, France.

Beyer, H. G., Martinez, J. P., Suri, M., Torres, J. L., Lorenz, E., Müller, S., Hoyer-Klick, C., and Ineichen, P. (2009). Report on Benchmarking of Radiation Products: Deliverable 1.1.3. `http://www.mesor.org/docs/MESoR_Benchmarking_of_radiation_products.pdf`. Viewed 23 August 2014.

Bird, R. E. and Hulstrom, R. L. (1981). A Simplified Clear Sky Model for Direct and Diffuse Insolation on Horizontal Surfaces. Golden, Colorado, USA.

Blanc, P. and Wald, L. (2012). The SG2 algorithm for a fast and accurate computation of the position of the Sun for multi-decadal time period. *Solar Energy*, **86**(10), 3072–3083.

Blanc, P., Gschwind, B., Lefèvre, M., and Wald, L. (2011). The HelioClim Project: Surface Solar Irradiance Data for Climate Applications. *Remote Sensing*, **3**(12), 343–361.

Blanc, P., Espinar, B., Geuder, N., Gueymard, C. A., Meyer, R., Pitz-Paal, R., Reinhardt, B., Renné, D., Sengupta, M., Wald, L., and Wilbert, S. (2014a). Direct normal irradiance related definitions and applications: The circumsolar issue. *Solar Energy*, **110**(0), 561–577.

Blanc, P., Gschwind, B., Lefevre, M., and Wald, L. (2014b). Twelve monthly maps of ground albedo parameters derived from MODIS data sets. In *Proceedings of the IGARSS 2014*, pages 3270–3272, Quebec, Canada.

Borfecchia, F., Caiaffa, E., Pollino, M., Cecco, L. d., Martini, S., La Porta, L., and Marucci, A. (2014). Remote Sensing and GIS in planning photovoltaic potential of urban areas. *European Journal of Remote Sensing*, pages 195–216.

Bucher, C., Betcke, J., Andersson, G., Bletterie, B., and Küng, L. (2012). Simulation of Distribution Grids with Photovoltaics by Means of Stochastic Load Profiles and Irradiance Data. In *Proceedings of the 27th European Photovoltaic Solar Energy Conference*, pages 3795–3800. München, Germany.

Bucher, C., Betcke, J., and Andersson, G. (2013a). Effects of variation of temporal resolution on domestic power and solar irradiance measurements. In *Proceedings of the IEEE PowerTech 2013*, Grenoble.

Bucher, C., Andersson, G., and Küng, L. (2013b). Increasing the PV Hosting Capacity of Distribution Power Grids: A Comparison of Seven Methods. In *Proceedings of the 28th European Photovoltaic Solar Energy Conference*, pages 4231–4235, Paris, France.

Buechner, J., Katzfey, J., Floercken, O., Moser, A., Schuster, H., Dierkes, S., van Leeuwen, T., van Verheggen, L., Uslar, M., and van Amelsvoort, M. (2014). Moderne Verteilernetze für Deutschland (Verteilernetzstudie). `http://www.bmwi.de/DE/Mediathek/publikationen,did=654018.html`. Viewed 5 December 2015.

Cano, D., Monget, J., Albuisson, M., Guillard, H., Regas, N., and Wald, L. (1986). A method for the determination of the global solar radiation from meteorological satellite data. *Solar Energy*, **37**(1), 31–39.

Cohen, M. A. and Callaway, D. S. (2016). Effects of distributed pv generation on california's distribution system, part 1: Engineering simulations. *Solar Energy*.

Deneke, H. M. and Roebeling, R. A. (2010). Downscaling of METEOSAT SEVIRI 0.6 and 0.8 $\mu$m channel radiances utilizing the high-resolution visible channel. *Atmospheric Chemistry and Physics*, **10**(20), 9761–9772.

DGS (2012). *Photovoltaische Anlagen: Leitfaden für das Elektro- und Dachdeckerhandwerk, Fachplaner, Architekten, Ingenieure, Bauherren und Weiterbildungsinstitutionen*. DGS, Landesverb. Berlin-Brandenburg, Berlin, 5 edition.

DGS (2015). EEG plant register: data from 03/2015. `http://www.energymap.info/download.html`. Viewed 24 April 2015.

Diabaté, L., Moussu, G., and Wald, L. (1989). Description of an operational tool for determining global solar radiation at ground using geostationary satellite images. *Solar Energy*, **42**(3), 201–207.

Dickert, J. and Schegner, P. (2011). Neue Ansätze der Modellierung synthetischer Lastgänge für Planung und Betrieb von Smart Grids. In *Proceedings of the International ETG-Congress 2011*, volume 1, Offenbach. VDE-Verlag.

DIgSILENT (2014). PV System: DIgSILENT PowerFactory Technical Reference Documentation: Version 15.2.

DIN 5034-2 (1985). Tageslicht in Innenräumen; Grundlagen.

DIN 55350-13 (1987). Begriffe der Qualitätssicherung und Statistik; Begriffe zur Genauigkeit von Ermittlungsverfahren und Ermittlungsergebnissen.

DIN EN 50160 (2011). Merkmale der Spannung in öffentlichen Elektrizitätsversorgungsnetzen: Merkmale der Spannung in öffentlichen Elektrizitätsversorgungsnetzen; Deutsche Fassung EN 50160:2010 + Cor. :2010.

DIN EN 50461 (2007). Solarzellen - Datenblattangaben und Angaben zum Produkt für kristalline Silizium-Solarzellen.

DIN EN 50470-3 (2007). Wechselstrom-Elektrizitätszähler - Teil 3: Besondere Anforderungen - Elektronische Wirkverbrauchszähler der Genauigkeitsklassen A, B und C.

DIN IEC 60076-7 (2008). Leistungstransformatoren - Teil 7: Leitfaden für die Belastung von ölgefüllten Leistungstransformatoren (IEC 60076-7:2005).

DLR (1999). Hourly global and direct normal irradiance for Europe, Africa and Asia. `https://wdc.dlr.de/data_products/SERVICES/SOLARENERGY/description.php`. Viewed 25 April 2015.

Drews, A., Keizer, A. C. d., Beyer, H. G., Lorenz, E., Betcke, J., van Sark, W. G. J. H. M., Heydenreich, W., Wiemken, E., Stettler, S., Toggweiler, P., Bofinger, S., Schneider, M., Heilscher, G., and Heinemann, D. (2007). Monitoring and remote failure detection of grid-connected PV systems based on satellite observations. *Solar Energy*, **81**(4), 548–564.

Dubielzig, G. (2007). *Referenzlastprofile von Ein- und Mehrfamilienhäusern für den Einsatz von KWK-Anlagen*, volume Nr. 560 of *Fortschrittsberichte VDI : Reihe 6, Energietechnik*. VDI-Verlag, Düsseldorf.

Düwall, P. (1985). *Ermittlung der Lastganglinien bei der Benutzung elektrischer Energie durch die bundesdeutschen Haushalte während eines Jahres: [Kurzfassung]*. Verlags- und Wirtschaftsges. d. Elektrizitätswerke, Frankfurt/Main.

DWD (2015). Climate Data Center (CDC): Monthly air temperature. `ftp://ftp-cdc.dwd.de/pub/CDC/`. Viewed 30 June 2015.

EEG (2014). Erneuerbare-Energien-Gesetz vom 21. Juli 2014 (BGBl. I S. 1066), das durch Artikel 4 des Gesetzes vom 22. Juli 2014 (BGBl. I S. 1218) geändert worden ist.

Eilenberger, S. and Braun, M. (2012). Herausforderungen und Lösungen für das Verteilnetz von morgen. In S. Tenbohlen and A. Gugel, editors, *Proceedings of the Stuttgarter Hochspannungssymposium 2012*, Stuttgart, Germany. Inst. für Energieübertragung und Hochspannungstechnik.

Einstein, A. (1905). Über einen die Erzeugung und Verwandlung des Lichtes betreffenden heuristischen Gesichtspunkt. *Annalen der Physik*, **322**(6), 132–148.

Eissa, Y., Munawwar, S., Oumbe, A., Blanc, P., Ghedira, H., Wald, L., Bru, H., and Goffe, D. (2015a). Validating surface downwelling solar irradiances estimated by the McClear model under cloud-free skies in the United Arab Emirates. *Solar Energy*, **114**, 17–31.

Eissa, Y., Korany, M., Aoun, Y., Boraiy, M., Abdel Wahab, M., Alfaro, S., Blanc, P., El-Metwally, M., Ghedira, H., Hungershoefer, K., and Wald, L. (2015b). Validation of the Surface Downwelling Solar Irradiance Estimates of the HelioClim-3 Database in Egypt. *Remote Sensing*, **7**(7), 9269–9291.

Engels, K. (2000). *Probabilistische Bewertung der Spannungsqualitat in Verteilungsnetzen*, volume 72 of *Aachener Beitrage zur Energieversorgung*. Klinkenberg Verlag, Aachen, 1 edition.

EnWG (2013). Energiewirtschaftsgesetz vom 7. Juli 2005 (BGBl. I S. 1970, 3621), das zuletzt durch Artikel 1 des Gesetzes vom 21. Februar 2013 (BGBl. I S. 346) geändert worden ist.

Ernest and Young GmbH (2013). Ergebnisse der Kosten-Nutzen-Analyse für einen flächendeckenden Einsatz intelligenter Zähler. `https://www.bmwi.de/BMWi/Redaktion/PDF/Publikationen/Studien/kosten-nutzen-analyse-fuer-flaechendeckenden-einsatz-intelligenterzaehler,property=pdf,bereich=bmwi2012,sprache=de,rwb=true.pdf`. Viewed 4 November 2015.

Espinar, B., Hoyer-Klick, C., Lefevre, M., Schroedter-Homscheidt, M., and Wald, L. (2014). USER'S GUIDE to the MACC-RAD Services on solar energy radiation resources: v3 - July 2014 - MACC-II Deliverable 122.6: Project MACC-II. `https://www.gmes-atmosphere.eu/documents/maccii/deliverables/rad/MACCII_RAD_DEL_D_122.6_final.pdf`. Viewed 24 December 2014.

Esri (2015). ESRI ArcGIS homepage. `http://www.esri.com/software/arcgis`. Viewed 22 August 2015.

Faiman, D. (2008). Assessing the outdoor operating temperature of photovoltaic modules. *Progress in Photovoltaics: Research and Applications*, **16**(4), 307–315.

Fath, K., Stengel, J., Sprenger, W., Wilson, H. R., Schultmann, F., and Kuhn, T. E. (2015). A method for predicting the economic potential of (building-integrated)

photovoltaics in urban areas based on hourly Radiance simulations. *Solar Energy*, **116**, 357–370.

Freymiller, S. (2015). personal communication to grid losses with Stefan Freymiller, network sales and distribution at Stadtwerke Ulm/Neu-Ulm Netze GmbH, 13.7.2015.

Fünfgeld, C. and Tiedemann, R. (2000). Anwendung der Repräsentativen VDEW-Lastprofile: step-by-step. `http://www.allgaeunetz.com/download/vdewm232000umsetzungderanalytischenlastprofilv.pdf`, Frankfurt a.M. Viewed 13 November 2015.

Ge, Y., Dai, J., Qian, K., Hepburn, D., and Zhou, C. (2015). Simulation of domestic electricity load profile by multiple gaussian distribution. In International Conference and Exhibition on Electricity Distribution, editor, *CIRED 2015 - 23rd International Conference and Exhibition on Electricity Distribution (CIRED)*, CIRED.

Geiger, M., Diabaté, L., Ménard, L., and Wald, L. (2002). A web service for controlling the quality of measurements of global solar irradiation. *Solar Energy*, **73**(6), 475–480.

Gellert, W., Küstner, H., Hellwich, M., and Kästner, H., editors (1969). *Großes Handbuch der Mathematik*. Buch und Zeit Verlagsgesellschaft m.b.H., Köln.

Glunz, S. W., Preu, R., and Biro, D. (2012). Crystalline Silicon Solar Cells. In A Sayigh, editor, *Comprehensive Renewable Energy*, pages 353–387. Elsevier.

Green, M. A., Emery, K., Hishikawa, Y., Warta, W., and Dunlop, E. D. (2015). Solar cell efficiency tables (Version 45). *Progress in Photovoltaics: Research and Applications*, **23**(1), 1–9.

Grenier, J. C., De La Casinire, A., and Cabot, T. (1994). A spectral model of Linke's turbidity factor and its experimental implications. *Solar Energy*, **52**(4), 303–313.

Grossi, L., Wirth, G., Lorenz, E., Spring, A., and Becker, G. (2014). Simulation of the Feed-in Power of Distributed PV Systems. In *Proceedings of the 29th European PV Solar Energy Conference and Exhibition*, pages 2916–2920, München, Germany. WIP.

Gueymard, C. A. (2009). Direct and indirect uncertainties in the prediction of tilted irradiance for solar engineering applications. *Solar Energy*, **83**(3), 432–444.

Gutnik, J., Heilscher, G., and Ruf, H. (2012). Langzeitdegradation kristalliner und amorpher Si-Module und Vergleich mit neueren Modulen. In *Proceedings of the 27. Symposium Photovoltaische Solarenergie*, Bad Staffelstein, Germany.

Hammer, A. (2001). Anwendungsspezifische Solarstrahlungsinformationen aus Meteosat-Daten. `http://oops.uni-oldenburg.de/317/`, Oldenburg. Viewed 5 December 2015.

Hammer, A., Heinemann, D., Hoyer, C., Kuhlemann, R., Lorenz, E., Müller, R., and Beyer, H. G. (2003). Solar energy assessment using remote sensing technologies. *Remote Sensing of Environment*, **86**(3), 423–432.

Heilscher, G., Gmehlin, M., Conrad, J., and Ehm, A. (2010). Concept for Large-Scale-Deployment of Grid Connected PV in the Private Sector at the Edge of Grid Parity. In *Proceedings of the 25th World Conference on Photovoltaic Energy Conversion*, pages 5305–5308, München, Germany.

Hess, M., Koepke, P., and Schult, I. (1998). Optical Properties of Aerosols and Clouds: The Software Package OPAC. *Bulletin of the American Meteorological Society*, **79**(5), 831–844.

Hoff, T. E. and Perez, R. (2010). Quantifying PV power Output Variability. *Solar Energy*, **84**(10), 1782–1793.

Hoff, T. E. and Perez, R. (2012). Modeling PV fleet output variability. *Solar Energy*, **86**(8), 2177–2189.

Hottel, H. C. and Woertz, B. B. (1942). Evaluation of flat-plate solar heat collector. *Transactions of ASME, Journal of Heat Transfer*, **64**(2), 91–104.

IEA (2014). High Penetration of PV in Local Distribution Grids: Subtask 2: Case-Study Collection. `http://www.iea-pvps.org/index.php?id=295`. Viewed 18 November 2015.

IEA (2015). Energy and Climate Change: World Energy Outlook Special Report. Paris.

Ineichen, P. (2013). Long term satellite hourly, daily and monthly global, beam and diffuse irradiance validation. Interannual variability analysis. `http://archive-ouverte.unige.ch/unige:29606`, Geneva. Viewed 5 December 2015.

Ineichen, P. and Perez, R. (2002). A new airmass independent formulation for the Linke turbidity coefficient. *Solar Energy*, **73**(3), 151–157.

Iqbal, M. (1983). *An introduction to solar radiation*. Academic Press, Toronto and New York.

IRENA (2015). *Renewable Power Generation Costs in 2014*. International Renewable Energy Agency. Viewed 25 September 2015.

ISO 9060 (1990). Solar energy – Specification and classification of instruments for measuring hemispherical solar and direct solar radiation.

Jakubiec, J. A. and Reinhart, C. F. (2013). A method for predicting city-wide electricity gains from photovoltaic panels based on LiDAR and GIS data combined with hourly Daysim simulations. *Solar Energy*, **93**, 127–143.

KACO (2010). Data sheet: KACO new energy blueplanet 00xi series: 6400xi. `http://www.aimscorp.net/documents/KBP6400XI_spec.pdf`. Viewed 9 November 2015.

Kasten, F. (1988). Elimination of the virtual diurnal variation of the Linke turbidity factor. *Meteorologische Rundschau*, **40**(3), 93–94.

Katzmaier, M. (2015). personal communication with Martin Katzmaier, team leader measurement electric power at Stadtwerke Ulm/Neu-Ulm Netze GmbH, 7.4.2015.

Kaufmann, T., Heilscher, G., Hess, S., Müller, R., Gerdes, M., Meier, F., and Gmehlin, M. (2014). Einspeisemanagement mit dem Smart Meter Gateway. In *Proceedings of the 29. Symposium Photovoltaische Solarenergie*, Bad Staffelstein, Germany.

Kerber, G. (2011). *Aufnahmefähigkeit von Niederspannungsverteilnetzen für die Einspeisung aus Photovoltaikkleinanlagen*. Der Andere Verl, Uelvesbüll.

King, D. L., Kratochvil, J. A., and Boyson, W. E. (1997a). Measuring solar spectral and angle-of-incidence effects on photovoltaic modules and solar irradiance sensors. In *Conference Record of the Twenty Sixth IEEE Photovoltaic Specialists Conference - 1997*, pages 1113–1116.

King, D. L., Kratochvil, J. A., and Boyson, W. E. (1997b). Temperature coefficients for PV modules and arrays: measurement methods, difficulties, and results. In

*Conference Record of the Twenty Sixth IEEE Photovoltaic Specialists Conference - 1997*, pages 1183–1186.

King, D. L., Boyson, W. E., and Kratochvill, J. A. (2004). Photovoltaic Array Performance Model. `http://prod.sandia.gov/techlib/access-control.cgi/2004/043535.pdf`, Albuquerque, USA. Viewed 1 March 2015.

King, D. L., Gonzalez, S., Galbraith, G. M., and Boyson, W. E. (2007). Performance Model for Grid-Connected Photovoltaic Inverters. `http://prod.sandia.gov/techlib/access-control.cgi/2007/075036.pdf`, Albuquerque, USA. Viewed 1 March 2015.

Köhler, C., Steiner, A., Lee, D., Thieler, J., Saint-Drenan, Y.-M., Ernst, D., Becker, C., Zirkelbach, M., and Ritter, B. (2015a). Assessing the impact of a solar eclipse on weather and photovoltaic production. *Meteorologische Zeitschrift*.

Köhler, C., Ruf, H., Steiner, A., Lee, D., Thieler, J., Casel, M., Funk, D., Ditz, K., Stakic, D., Ebe, F., Meier, F., Wosnitza, M., Ritter, B., and Heilscher, G. (2015b). Nutzung Numerischer Wettervorhersagen in der Simulation von Verteilnetzen: Die Effekte einer Sonnenfinsternis auf netzgekoppelte PV-Anlagen und Netztransformatoren. In *Proceedings of the 30. Symposium Photovoltaische Solarenergie*, Bad Staffelstein, Germany.

Köpke, P., editor (2012). *Satellitenmeteorologie ; 59 Tabellen*, volume 3525 of *UTB*. Ulmer, Stuttgart.

Kopp, G. and Lean, J. L. (2011). A new, lower value of total solar irradiance: Evidence and climate significance. *Geophysical Research Letters*, **38**(1), n/a.

Krauter, S., Grunow, P., Preiss, A., Rindert, S., and Ferretti, N. (2008). Inaccuracies of input data relevant for PV yield prediction. In *Proceedings of the 33rd IEEE Photovolatic Specialists Conference (PVSC)*.

Kriebel, K. T., Gesell, G., Kästner, M., and Mannstein, H. (2003). The cloud analysis tool APOLLO: Improvements and validations. *International Journal of Remote Sensing*, **24**(12), 2389–2408.

Kronthaler, F. (2014). *Statistik angewandt: Datenanalyse ist (k)eine Kunst*. Springer-Lehrbuch. Springer Spektrum, Berlin.

Kroposki, B., Marion, W., King, D. L., Boyson, W. E., and Kratochvil, J. A. (2000). Comparison of module performance characterization methods. In *Proceedings of the 28th IEEE Photovoltaic Specialists Conference*, pages 1407–1411.

Kühnert, J., Lorenz, E., Betcke, J., Hammer, A., and Heinemann, D. (2014). Regionale PV-Leistungsvorhersagen für den Kurzzeit-Bereich auf Basis von Satellitendaten, numerischen Wetterprognosen und PV-Leistungsmessungen. In OTTI, editor, *Proceedings of the 29. Symposium Photovoltaische Solarenergie*.

Larson, G. W. and Shakespeare, R. (2003). *Rendering with Radiance: The art and science of lighting visualization*. Space & Light, Davis, Calif., rev. ed edition.

Lave, M., Reno, M. J., and Broderick, R. J. (2015). Characterizing local high-frequency solar variability and its impact to distribution studies. *Solar Energy*, **118**, 327–337.

Lefèvre, M., Oumbe, A., Blanc, P., Espinar, B., Gschwind, B., Qu, Z., Wald, L., Schroedter-Homscheidt, M., Hoyer-Klick, C., Arola, A., Benedetti, A., Kaiser, J. W., and Morcrette, J.-J. (2013). McClear: a new model estimating downwelling solar radiation at ground level in clear-sky conditions. *Atmospheric Measurement Techniques*, **6**(9), 2403–2418.

Lefevre, M., Blanc, P., Espinar, B., Gschwind, B., Menard, L., Ranchin, T., Wald, L., Saboret, L., Thomas, C., and Wey, E. (2014). The HelioClim-1 Database of Daily Solar Radiation at Earth Surface: An Example of the Benefits of GEOSS Data-CORE. *Selected Topics in Applied Earth Observations and Remote Sensing, IEEE Journal of*, **7**(5), 1745–1753.

Linke, F. (1922). Transmissions-Koeffizient und Trübungsfaktor. In *Beiträge zur Physik der Atmosphäre 10*, volume 10, pages 91–103. Karl J. Trübner, Straßburg.

Liou, K.-N. (1992). *Radiation and cloud processes in the atmosphere: Theory, observation, and modeling*, volume no. 20 of *Oxford monographs on geology and geophysics*. Oxford University Press, New York.

Liu, H., Pinker, R. T., and Holben, B. N. (2005). A global view of aerosols from merged transport models, satellite, and ground observations. *Journal of Geophysical Research: Atmospheres*, **110**(D10).

Loutzenhiser, P., Manz, H., Felsmann, C., Strachan, P., Frank, T., and Maxwell, G. (2007). Empirical validation of models to compute solar irradiance on inclined surfaces for building energy simulation. *Solar Energy*, **81**(2), 254–267.

Luoma, J., Kleissl, J., and Murray, K. (2012). Optimal inverter sizing considering cloud enhancement. *Solar Energy*, **86**(1), 421–429.

Mayer, B. and Kylling, A. (2005). Technical note: The libRadtran software package for radiative transfer calculations - description and examples of use. *Atmospheric Chemistry and Physics*, **5**(7), 1855–1877.

Meier, F. (2014). personal communication with Florian Meier, head of grid planning, Stadtwerke Ulm/Neu-Ulm Netze GmbH, 21.10.2014.

Mertens, K. (2013). *Photovoltaik: Lehrbuch zu Grundlagen, Technologien und Praxis*. Hanser, München, 2 edition.

Meteotest (2015). Homepage Meteonorm. `http://meteonorm.com/`. Viewed 9 October 2015.

Mohrmann, M., Reese, C., Hofmann, L., and Schmiesing, J. (2012). Untersuchung von Niederspannungsverteilnetzen anhand von synthetischen Netzstrukturen. In *Proceedings of the VDE Kongress 2012 Smart Grid: Intelligente Energieversorgung der Zukunft*. Stuttgart, Germany.

Mueller, R., Dagestad, K., Ineichen, P., Schroedter-Homscheidt, M., Cros, S., Dumortier, D., Olseth, J., Piernavieja, G., Reise, C., Wald, L., and Heinemann, D. (2004). Rethinking satellite-based solar irradiance modelling: The SOLIS clear-sky module. *Remote Sensing of Environment*, **91**(2), 160–174.

Mürdel, S. (2015). personal communication to switching operations at medium voltage level with Stefan Mürdel at Stadtwerke Ulm/Neu-Ulm Netze GmbH, 14.7.2015.

NAV (2006). Niederspannungsanschlussverordnung: NAV.

Ndiaye, A., Charki, A., Kobi, A., Kébé, C. M., Ndiaye, P. A., and Sambou, V. (2013). Degradations of silicon photovoltaic modules: A literature review. *Solar Energy*, **96**, 140–151.

Oumbe, A., Qu, Z., Blanc, P., Lefèvre, M., Wald, L., and Cros, S. (2014). Decoupling the effects of clear atmosphere and clouds to simplify calculations of the broadband solar irradiance at ground level. *Geoscientific Model Development*, **7**(4), 1661–1669.

Pardatscher, R., Witzmann, R., Wirth, G., Becker, G., Garhamer, M., and Brantl, J. (2011). Untersuchung zu den Auswirkungen von Photovoltaikeinspeisung auf das Nieder- und Mittelspannungsnetz. In *Proceedings of the International ETG-Congress 2011*, Würzburg, Germany. VDE-Verlag.

Paulescu, M., Paulescu, E., Gravila, P., and Badescu, V. (2012). *Weather Modeling and Forecasting of PV Systems Operation*. Green Energy and Technology. Springer, Dordrecht.

Perez, R., Ineichen, P., Seals, R., Michalsky, J., and Stewart, R. (1990). Modeling daylight availability and irradiance components from direct and global irradiance. *Solar Energy*, **44**(5), 271–289.

Pflugradt, N. and Platzer, B. (2012). Verhaltensbasierter Lastprofilgenerator für Strom- und Warmwasser-Profile. In *22. Symposium Thermische Solarenergie*. OTTI, Regensburg.

Qu, Z. (2013). *The new method Heliosat-4 for the assessment of surface solar radiation*. Ph.D. thesis, Ecole Nationale Supérieure des Mines de Paris.

Qu, Z., Oumbe, A., Blanc, P., Lefevre, M., Wald, L., Schroedter-Homscheidt, M., Gesell, G., and Klueser, L. (2012). Assessment of Heliosat-4 surface solar irradiance derived on the basis of SEVIRI-APOLLO cloud products. In *Proceedings of the 2012 EUMETSAT Meteorological Satellite Conference*, Sopot, Poland.

Reda, I. and Andreas, A. (2004). Solar position algorithm for solar radiation applications. *Solar Energy*, **76**(5), 577–589.

Reda, I. and Andreas, A. (2007). Corrigendum to "Solar position algorithm for solar radiation applications" [Solar Energy 76 (2004) 577–589]. *Solar Energy*, **81**(6), 838.

Reindl, D., Beckman, W., and Duffie, J. (1990a). Diffuse fraction correlations. *Solar Energy*, **45**(1), 1–7.

Reindl, D., Beckman, W., and Duffie, J. (1990b). Evaluation of hourly tilted surface radiation models. *Solar Energy*, **45**(1), 9–17.

Remund, J., Wald, L., Lefevre, M., Ranchin, T., and Page, John, H. (2003). Worldwide Linke turbidity information. In *Proceedings of the ISES Solar World Congress 2003*, Goteborg, Sweden. International Solar Energy Society (ISES).

Renné, D. (2014). Emerging Meteorological Requirements to Support High Penetrations of Variable Renewable Energy Sources: Solar Energy. In A. Troccoli, L. Dubus, and S. E. Haupt, editors, *Weather matters for energy*, pages 257–273. Springer, New York.

Rigollier, C., Bauer, O., and Wald, L. (2000). On the clear sky model of the ESRA — European Solar Radiation Atlas — with respect to the heliosat method. *Solar Energy*, **68**(1), 33–48.

Rigollier, C., Lefèvre, M., and Wald, L. (2004). The method Heliosat-2 for deriving shortwave solar radiation from satellite images. *Solar Energy*, **77**(2), 159–169.

Rikos, E., Tselepis, S., Hoyer-Klick, C., and Schroedter-Homscheidt, M. (2008). Stability and Power Quality Issues in Microgrids Under Weather Disturbances. *Selected Topics in Applied Earth Observations and Remote Sensing, IEEE Journal of*, **1**(3), 170–179.

Ruf, H. (2012). Netzintegration von PV: ENDORSE - Entwicklung einer Solarleistungsvorhersage auf Satellitenbasis für die Netzbetreiber. In *Oral presentation at the Smart Grids Week 2012*, Bregenz, Austria.

Ruf, H., Stetter, D., Lanig, S., Hoyer-Klick, C., Meier, F., and Heilscher, G. (2012a). Active Grid Planning Based on Solar Power Roof Potential Analysis. In *Proceedings of the 27th European Photovoltaic Solar Energy Conference*, pages 3782–3787. Hamburg, Germany.

Ruf, H., Heilscher, G., Meier, F., Mayer, O., and Grottke, M. (2012b). Impact of Increasing Photovoltaic Energy Penetration on the Distribution Grid. In *Proceedings of the 27th European Photovoltaic Solar Energy Conference*, pages 4534–4538. Hamburg, Germany.

Ruf, H., Schroedter-Homscheidt, M., Beyer, H. G., Meier, F., and Heilscher, G. (2013). Analysis of Cloud Indicators to Derive the Bus Bar Voltage at a Local Low Voltage Distribution Grid Transformer. In *Proceedings of the 28th European Photovoltaic Solar Energy Conference*, page 3944, Paris, France.

Ruf, H., Funk, D., Meier, F., and Heilscher, G. (2015). Bestimmung von Ausrichtungs- und Neigungswinkeln von Bestandsanlagen mittels LIDAR Daten. In *Proceedings of the 30. Symposium Photovoltaische Solarenergie*, Bad Staffelstein, Germany.

Saunders, R. W. and Kriebel, K. T. (1988). An improved method for detecting clear sky and cloudy radiances from AVHRR data. *International Journal of Remote Sensing*, **9**(1), 123–150.

Schaaf, C. B., Gao, F., Strahler, A. H., Lucht, W., Li, X., Tsang, T., Strugnell, N. C., Zhang, X., Jin, Y., Muller, J.-P., Lewis, P., Barnsley, M., Hobson, P., Disney,

M., Roberts, G., Dunderdale, M., Doll, C., d'Entremont, R. P., Hu, B., Liang, S., Privette, J. L., and Roy, D. (2002). First operational BRDF, albedo nadir reflectance products from MODIS. *Remote Sensing of Environment*, **83**(1-2), 135–148.

Schäfer, S., Heilscher, G., Ruf, H., and Meier, F. (2013). Auswertungen von Wirkleistungssprüngen an einem Niederspannungstransformator mit PV-Einspeisung. In *Proceedings of the 28. Symposium Photovoltaische Solarenergie*, volume 1.

Schillings, C., Mannstein, H., and Meyer, R. (2004). Operational method for deriving high resolution direct normal irradiance from satellite data. *Solar Energy*, **76**(4), 475–484.

Schmetz, J., Pili, P., Tjemkes, S., Just, D., Kerkmann, J., Rota, S., and Ratier, A. (2002). An Introduction to Meteosat Second Generation (MSG). *Bulletin of the American Meteorological Society*, **83**(7), 977–992.

Schroedter Homscheidt, M., Betcke, J., Gesell, G., Heinemann, D., and Holzer-Popp, T. (2004). Energy-specific Solar Radiation data from MSG: Current Status of the Heliosat-3 project. In H. Lacoste, editor, *Proceedings of the second MSG RAO workshop*, volume 582 of *SP*, pages 131–136. ESA Publications Division.

Schwarz, M. and Kollmann, A. (2014). Wirtschaftliche Betrachtung von Netzausbau und Smart Grid-Lösungen in der Niederspannungsebene. *e & i Elektrotechnik und Informationstechnik*, **131**(3), 99–104.

Skoplaki, E. and Palyvos, J. A. (2009). On the temperature dependence of photovoltaic module electrical performance: A review of efficiency/power correlations. *Solar Energy*, **83**(5), 614–624.

Stakic, D. E., Ebe, F., Ruf, H., Meier, F., and Heilscher, G. (2015). Simulation des Lebensdauerverbrauchs von ölbefüllten Verteilnetztransformatoren unter Berücksichtigung des weiteren Ausbaus dezentraler Photovoltaikeinspeisung. In *Proceedings of the 30. Symposium Photovoltaische Solarenergie*, Bad Staffelstein, Germany.

Stein, J., Perez, R., and Parkins, A. (2010). Validation of pv performance models using satellite-based irradiance measurements: A case study. In R. Campbell-Howe, editor, *Proceedings of the 39th ASES National Solar Conference*. American Solar Energy Society.

Stein, J. S. (2012). The photovoltaic Performance Modeling Collaborative (PVPMC). In *Proceedings of the 38th IEEE Photovoltaic Specialists Conference (PVSC)*, pages 003048–003052. IEEE.

Stetz, T., Wolf, H., Saint Drenan, Y.-M., Kämpf, E., Probst, A., Eilenberger, S., Braun, M., Schöllhorn, D., and Schmidt, S. (2012). Stochastische Analyse von Smart-Meter Messdaten. In *Proceedings of the VDE Kongress 2012 Smart Grid: Intelligente Energieversorgung der Zukunft*. Stuttgart, Germany.

StromNZV (2014). Verordnung über den Zugang zu Elektrizitätsversorgungsnetzen: StromNZV.

TAB (2008). Technische Anschlussbedingungen für den Anschluss an das Mittelspannungsnetz: TAB Mittelspannung 2008. Berlin.

TAB (2009). Technische Anschlussbedingungen für den Anschluss an das Niederspannungsnetz: TAB 2007: mit BDEW-Ergänzungen. Berlin.

Tjaden, T., Weniger, J., Bergner, J., Schnorr, F., and Quaschning, V. (2014). Einfluss des Standorts und des Nutzerverhaltens auf die energetische Bewertung von PV-Speichersystemen. In *Proceedings of the 29. Symposium Photovoltaische Solarenergie*, Bad Staffelstein, Germany.

Trewartha, G. T. (1954). *An Introduction to Climate*. McGraw-Hill, New York, 3 edition.

Ueda, Y., Kurokawa, K., Kitamura, K., Yokota, M., Akanuma, K., and Sugihara, H. (2009). Performance analysis of various system configurations on grid-connected residential PV systems. *Solar Energy Materials and Solar Cells*, **93**(6–7), 945–949.

Vázquez, M. and Rey-Stolle, I. (2008). Photovoltaic module reliability model based on field degradation studies. *Progress in Photovoltaics: Research and Applications*, **16**(5), 419–433.

VDE-AR-N 4105 (2011). Erzeugungsanlagen am Niederspannungsnetz.

VDI 4655 (2008). Referenzlastprofile von Ein- und Mehrfamilien-häusern für den Einsatz von KWK-Anlagen.

Vermote, E. F., Tanre, D., Deuze, J. L., Herman, M., and Morcette, J.-J. (1997). Second Simulation of the Satellite Signal in the Solar Spectrum, 6S: an overview. *Geoscience and Remote Sensing, IEEE Transactions on*, **35**(3), 675–686.

Verso, A., Martin, A., Amador, J., and Dominguez, J. (2015). GIS-based method to evaluate the photovoltaic potential in the urban environments: The particular case of Miraflores de la Sierra. *Solar Energy*, **117**, 236–245.

Wald, L. (2014). Heliosat-4 use of ground albedo and MSG parameters: Feburary 2014 - MACC-II Deliverable 123.6: Project MACC-II. `https://www.gmes-atmosphere.eu/documents/maccii/deliverables/rad/MACCII_RAD_DEL_D123.3_20140207_wald.pdf`. Viewed 5 December 2015.

Wieland, T., Schmautzer, E., Fickert, L., and Eberhart, S. (2015). Probabilistic approach for the determination of connection power using smart meter data for urban households with decentralized generation and storage units. In Verband der Elektrotechnik Elektronik Informationstechnik e. V., editor, *International ETG Congress 2015*, pages 422–427. VDE VERLAG.

Wilks, D. S., editor (2011). *International Geophysics : Statistical Methods in the Atmospheric Sciences*. Academic Press.

Wirth, G. (2015). Modellierung der Netzeinfluesse von Photovoltaikanlagen unter Verwendung meteorologischer Parameter. `http://oops.uni-oldenburg.de/2186/`, Oldenburg. Viewed 11 April 2015.

Wirth, G., A. Spring, Becker, G., R. Pardatscher, M. Ldl, Witzmann, R., J. Brantl, M. Garhamer, and H. Wagenhuser (2011). Felduntersuchung der Netzauslastung und Spannungsanhebung durch PV-Anlagen. In *Proceedings of 26. Symposium Photovoltaische Solarenergie*, Bad Staffelstein, Germany.

WMO (2008). Guide to meteorological instruments and methods of observation. `https://www.wmo.int/pages/prog/www/IMOP/CIMO-Guide.html`, Geneva, Switzerland. Viewed 13 July 2015.

Yingli (2012). Data sheet: Yingli Green Energy Holding Co. Ltd. YGE 60 Cell 40mm SERIES: YL230P-29b. `http://www.yinglisolar.com/assets/uploads/products/downloads/YGE_60_Cell_Series_EN.pdf`. Viewed 9 November 2015.

Zarzalejo, L. F., Polo, J., Martín, L., Ramírez, L., and Espinar, B. (2009). A new statistical approach for deriving global solar radiation from satellite images. *Solar Energy*, **83**(4), 480–484.

Zehner, M., Hartmann, M., Weizenbeck, J., Gratzl, T., Weigl, T., Mayer, B., Wirth, G., Krawczynski, M., Betts, T., Gottschalg, R., Hammer, A., Giesler, B., and Mayer, O. (2010). Systematic analysis of meteorological irradiation effects. In *Proceedings of the 25th World Conference on Photovoltaic Energy Conversion*, pages 4545–4548. WIP-Renewable Energies.

Zelenka, A., Perez, R., Seals, R., and Renné, D. (1999). Effective Accuracy of Satellite-Derived Hourly Irradiances. *Theoretical and Applied Climatology*, **62**(3-4), 199–207.